

---

# **A setup for imprinting artificial magnetic fields on ultracold atoms**

**Josselin Bernardoff**

---



**Lehrstuhl von Prof. Dr. Immanuel BLOCH**



---

# **A setup for imprinting artificial magnetic fields on ultracold atoms**

---

**Josselin Bernardoff**

---

Masterarbeit  
an der Fakultät für Physik  
der Ludwig-Maximilians-Universität  
München

vorgelegt von  
Josselin BERNARDOFF

München, den 5. August 2013



# Contents

<b>Abstract</b>	<b>ix</b>
<b>1 Introduction</b>	<b>1</b>
1.1 Quantum mechanics, quantum computing, quantum simulation . . . . .	1
1.2 General motivation for artificial gauge fields . . . . .	2
<b>2 Artificial gauge fields</b>	<b>5</b>
2.1 Previous simulation methods – the relevance of a wavefunction’s phase . . . . .	5
2.1.1 Review of past methods for realizing artificial gauge fields . . . . .	5
2.1.2 Explaining with equations . . . . .	7
2.2 The Berry’s phase . . . . .	9
2.3 Optical flux lattices . . . . .	10
2.4 Adapting the scheme to potassium . . . . .	17
2.4.1 Accommodating the above ideas to a real multi-level atom . . . . .	17
2.4.2 Summary of the experimental requirement . . . . .	18
<b>3 Experimental setup</b>	<b>21</b>
3.1 The Raman setup . . . . .	21
3.2 The semiconductor tapered amplifier . . . . .	22
3.3 Attenuation of resonant light in a vapor cell . . . . .	24
3.3.1 Estimating the needed attenuation . . . . .	25
3.3.2 Results using a spectral intensity . . . . .	26
3.3.3 Theoretical description of light absorption in the atomic vapour . .	28
3.3.4 Measurement of the absorption . . . . .	32
3.3.5 Analysis of the data . . . . .	37
3.3.6 Conclusion & issues concerning each method . . . . .	40
3.4 Other options for filtering out the resonant light . . . . .	40
<b>4 Phase noise and Phase-Locked Loop (PLL)</b>	<b>43</b>
4.1 Why do we need a phase-locked loop ? . . . . .	43
4.2 How does our PLL work ? . . . . .	44
4.2.1 Main lines of the loop . . . . .	44
4.2.2 Inherent limitations . . . . .	46

4.2.3	The lock-box – Use of a double integrator . . . . .	47
4.3	Performance, frequency response . . . . .	49
4.3.1	Measurements with a spectrum analyzer . . . . .	50
4.3.2	Frequency response . . . . .	54
4.3.3	Transient response and steady-state error . . . . .	59
4.3.4	Performance of the lock as a function of the light intensity . . . . .	62
<b>5</b>	<b>Conclusion &amp; outlook</b>	<b>65</b>
<b>A</b>	<b>More details on the electronics</b>	<b>67</b>
<b>B</b>	<b>Effective Schrödinger equation for an adiabatic evolution</b>	<b>75</b>
<b>C</b>	<b>Picture of the cell and oven for filtering resonant light</b>	<b>77</b>
<b>D</b>	<b>The acousto-optical effect, a coherent interaction</b>	<b>79</b>
<b>E</b>	<b>Basic control theory and PLLs more specifically</b>	<b>82</b>
E.1	The general feedback loop . . . . .	82
E.2	General consideration about PLLs . . . . .	83
E.3	The PLL in the Fourier domain . . . . .	85
E.4	Analysis of the simplest controllers . . . . .	86
<b>F</b>	<b>Looking at the setup in more detail</b>	<b>90</b>
F.1	The whole loop step by step . . . . .	90
F.2	Schematic of the whole loop . . . . .	92

# List of Figures

2.1	Drawing of a rotating BEC with vortices . . . . .	6
2.2	Levels, couplings and laser beams' position for the optical flux lattice . . . . .	11
2.3	Optical scalar potential generated by the three in-plane beams . . . . .	13
2.4	Coupling and potential in one unit cell . . . . .	15
2.5	Schematic of the beam size compared to the atoms . . . . .	19
3.1	Whole optical setup . . . . .	23
3.2	Optical spectra of the diode and the TA . . . . .	25
3.3	Saturation parameter density $\tilde{s}(\delta, I; \lambda)$ vs. wavelength . . . . .	27
3.4	Integrated saturation parameter for D1 and D2 potassium lines . . . . .	28
3.5	Comparison of the Voigt, Gauss and Lorentz profiles . . . . .	30
3.6	$p_{\text{sat}}$ as a function of T for potassium . . . . .	31
3.7	Photodiode signal of absorption . . . . .	33
3.8	Attenuation as a function of temperature . . . . .	34
3.9	Shape of the signal from the SIRAH EagleEye with absorption . . . . .	35
3.10	Optical spectrum with and without absorption by the vapor cell . . . . .	36
3.11	Attenuation factor in linear and log scale . . . . .	37
3.12	Attenuation factor as a function of intensity . . . . .	38
3.13	Fit for absorption vs. intensity . . . . .	39
4.1	Comparison of the spectra of the VCO noise and the fiber noise . . . . .	45
4.2	Schematic of the whole PLL showing all the essential parts . . . . .	46
4.3	Circuit of a PI controller . . . . .	48
4.4	Transfer function of a PI controller . . . . .	49
4.5	Spectrum of the locked and unlocked signal over 30kHz . . . . .	51
4.6	Spectrum of the locked and unlocked signal over 300kHz . . . . .	52
4.7	Spectrum of the beat note of two locked beam after the fiber . . . . .	53
4.8	Spectrum showing the laser mode shape over 50MHz . . . . .	54
4.9	Connections to measure the transfer function of the lock-box only . . . . .	55
4.10	Transfer function of the lockbox with P gain . . . . .	56
4.11	Connections to measure the transfer function of the whole loop . . . . .	57
4.12	Transfer function of the whole loop with different gains . . . . .	58
4.13	Phase vs. frequency for three different dead times . . . . .	59

4.14	Transient response of the PLL for a pulse, with proportional gain . . . . .	60
4.15	Error signal in the unlocked state . . . . .	61
4.16	Comparison of error signal for two time scales . . . . .	62
4.17	Spectra of the lock at low intensity . . . . .	63
A.1	Circuit of the lock-box . . . . .	69
A.2	Circuit of the lock-box with function of each part . . . . .	70
A.3	DC part of the lock-box circuit . . . . .	71
A.4	AC→DC circuit . . . . .	72
A.5	Connections on the lock-box PCB . . . . .	73
A.6	Names of components on the lock-box PCB . . . . .	74
C.1	Picture of the long potassium cell . . . . .	77
C.2	Picture of the input face of the oven . . . . .	77
C.3	Picture of the oven used to heat up the cell . . . . .	78
D.1	Model for the acousto-optical effect . . . . .	79
D.2	Phase shift in an AOM . . . . .	80
E.1	General representation of a feedback loop . . . . .	82
E.2	General block diagram of a phase-locked loop . . . . .	84
E.3	Amplitude gain of the three basic filters . . . . .	87
F.1	The whole path of the PLL . . . . .	92

# Abstract

In this thesis, we report about the development of an optical setup together with control electronics. The goal of that setup is to implement a way to make neutral fermionic atoms simulate the behaviour of charged particles in a strong magnetic field. This kind of experiment has been so far specific to the domain of solid state physics with bidimensional semiconducting heterostructures, where very peculiar electronic phenomena occur, such as the quantum Hall effect. Simulating a magnetic field has already been the subject of much research in the field of ultracold atoms but a new experimental scheme called an *optical flux lattice* could for the first time simulate a sufficiently strong and uniform magnetic flux to access the quantum Hall regime.

After introducing the concept of “analog quantum simulation”, we describe the underlying theory of the optical flux lattice as well as the previous schemes used for the simulation of magnetic fields. Such an optical flux lattice – more involved than usual scalar optical lattice schemes – makes us see how the engineering of a Hamiltonian thanks to spatially dependent Raman couplings can produce a so-called Berry’s phase which allows us to mimic the vector potential and the Lorentz force felt by electrons in a strong magnetic field. Then we show what the setup is composed of. The semiconductor tapered amplifier is the light source used; it has the drawback of possessing a strong *amplified spontaneous emission* background, which contains resonant light for potassium at the wavelength we want to operate it. We showed how we can use a vapor cell in order to filter out the resonant light. Even if more investigation could give us better information about the actual attenuation factor, we obtained a good enough filter. The last chapter is devoted to the design of a phase-locked loop, which stabilizes the phase of laser light transmitted through an optical fiber by feedback to an acousto-optic modulator constituting a bridge between electronics and laser light; we show that the phase-locked loop fulfills the requirements it has been built to meet and then characterize it more thoroughly. Suppressing that noise ensures that the optical lattice does not heat up the atom and keeps the coherence of the Raman couplings necessary for the artificial gauge field.



# Chapter 1

## Introduction

### 1.1 Quantum mechanics, quantum computing, quantum simulation

Now that magnetic and optical methods of cooling and trapping are well-known, well-documented and very efficient, physicists want to take advantage of the particularities of ultracold systems and expand that field, link it to some other areas of research in physics. In spite of the interest of research in fundamental science, driven by the curiosity of a scientists' community around the world, there is a will to try and apply all the theoretical and empirical knowledge to subjects that a broader part of the society can grasp. The recent amazing success of electronics has shown how our perception of everyday life can be changed – for better and for worse – by technology. Ultracold atoms could provide crucial information about very intricate problems of electronics.

We can notice that computers were made possible by many discoveries in electrical engineering, which was – for a large part, but not only – the successful application of the theory of quantum mechanics. Surprisingly enough, and quite ironically one could argue, computer science applied to physics has found in the very same quantum theory its own limitation. Indeed, we know that simulation a classical system of  $N$  spins requires  $2N$  variables to be fully described, whereas the quantum version requires a Hilbert space state with dimension  $2^N$ , which is intractable for any supercomputer of a realistic size for  $N$  over, say, 50. In the virtuous circle of modern science, where new discoveries enable the research to go deeper and thus pave the way for more new discoveries, science has tripped itself with the invention of quantum mechanics but this source of challenging problems have also been the motivation for exciting research for more than eighty years now.

One of the main goal of present research in physics is to try and master quantum computation. That idea emerged more than thirty years ago[1]; nevertheless the goal seems far from being reached. The way to building a real quantum computer that could surpass a classical digital computer is still fraught with technical difficulties even if it is known in principle. Decoherence, for instance, is a main challenge in quantum computation.

The term “quantum computer” usually denotes *digital quantum computation*, which

consists in replacing each bit of a classical computer by a quantum bit (qubit). The idea is to use the fact that the state space of a quantum system grows exponentially with its size for the purpose of computational power. This digital quantum computation aims at building a computer that uses quantum algorithm which solve a problem much faster and could potentially apply to any problem of quantum mechanics.

Nevertheless there exist another facet of quantum computing, called quantum simulation or “analog quantum simulation” [2]. Quantum simulation is a recent domain and a nice way to expand the physics of ultracold systems. The idea of simulation is to engineer a real system that obeys the same equations as another system. If the *simulating system* is more controllable in its parameter than the *simulated system*, one can hope to probe, understand and predict the simulated system by testing how the simulating system behaves when the parameters are modified. Several centuries ago, scientists were already devising very sophisticated clocks like the Strasbourg’s clock which can simulate the movement of celestial bodies. The simulation is not limited to ultracold atoms and several fields like trapped ions [3] or photonic systems [4] deal with quantum simulation. This thesis deals with a part of the technical implementation of a simulation scheme that aims at creating an *artificial gauge field*.

The first chapter explains the main ideas of a scheme which should simulate the behaviour of electrons in a strong magnetic field. The crucial concepts are reviewed and then we show how we link these concepts to our system of ultracold atoms.

Then the content of the optical setup is explained. In particular, we focus on the process of filtering unwanted light which would considerably hurt the experiment due to heating.

The last chapter talks about the development of a phase-locked loop; the goal of such a setup for us is to have a good reproducibility of the experiment and also limit heating. The theory of PLL needed to understand the setup of this thesis has been added in Appendix E.

Finally we conclude about the results and give some outlook.

## 1.2 General motivation for artificial gauge fields

The ultracold atoms research community is achieving quickly much progress in quantum simulation. The latter consists, as already said, in imitating the equation of motion of a system and that means, in the frame of quantum mechanics, that we have to engineer Hamiltonians. We chose a model for test that corresponds to a certain Hamiltonian and then try and find a controllable and observable system which has the same Hamiltonian. Research teams around the world are devising step by step new simulation techniques for solid state physics, which is dealing a lot with the description of how electrons behave in a material. Optical lattices is the trick by which the crystal structure is simulated.

The reasons why ultracold gases are so promising is the very high degree of control over parameters such as interaction strength, purity of the lattice, *etc.* that one can reach;

nevertheless, there are major drawbacks in using atoms on a lattice: first, they are much heavier than electrons and the length scale occurring in “natural” electronic systems – the Bohr radius – is much smaller. For that reason, even with sub-nK temperatures, the ratio of the thermal energy unit  $kT$  to Fermi energy  $E_F$ , with a scaling  $E_F \propto n^{2/3}/m$  where  $n$  is the density of fermions with mass  $m$ , is much higher than what is achievable with electrons in a solid state crystal. As a result, as far as fermionic collective phenomena are concerned, cold atoms are “not that cold”. Moreover – and that is the drawback we will be addressing in this chapter – atoms do not have a charge. If one uses charged ions instead of atoms, the strength of the Coulomb repulsion completely overwhelms the optical lattice potential and ions arrange in a Coulomb crystal.

Fortunately, physicists come up often enough with smart tricks that allow to circumvent such issues. We will deal here with a way of using the internal structure of atoms with many energy levels – which electrons do not possess – in order to have them act as if they were charged particles subjected to a magnetic field. The fact that electrons have a charge also lead to the repulsive Coulomb force but, in this thesis, we are only interested in mimicing the interaction of a charge with a  $\vec{B}$  field *i.e* the Lorentz force.

Very exciting physics can be observed when a solid is subjected to a magnetic field. If the  $\vec{B}$  field is rather weak, it gives rise in actual electronic systems to phenomena that have been extensively used for learning more about the properties of the material such as the de Haas-van Alphen effect, very much used to map the Fermi surface of metals (see for instance Ref.[5]). When the  $\vec{B}$  field is high enough, the physics of quantum Hall effect emerge. In that latter state, the metal displays very peculiar and interesting properties, the main one being the quantization of Hall resistance as a function of the magnetic field’s magnitude, regardless of the geometry of the sample or of some material properties such as impurities or electron densities. The Hall resistance is the resistance transversal to the electric field that appears in an eletronic system subjected to a magnetic field and comes from the deflection of a charge by the Lorentz force. That effect has been used to perform extremely high precision measurements of the fine structure constant and also to define the definition of the Ohm unit and calibration of resistors. The physics of the quantum Hall effect is a very rich source of intriguing phenomena. Indeed, the results that were first observed [6] can be accounted for by the so-called integer quantum Hall effect. This effect can emerge in the model that do not take any interaction into account. However, another regime were interaction is crucial has been observed: the so-called fractional quantum Hall effect in which electrons “reorganize” via their interactions into a system where the charge carriers appear to have a fractional charge. This is not yet fully understood and is still the object of much research.

This thesis is not about explaining how the quantum Hall effect works and the reader can look up Ref.[7] for an explanation; we focus hereafter only on a scheme whose goal is to try and simulate the extremely rich behaviour of electrons in a magnetic field by means of an optical lattice, which might in turn be an important step toward simulating the quantum Hall effect.



# Chapter 2

## Artificial gauge fields

We introduced the notion of quantum simulation in the introduction. In this chapter, we will apply that idea to gauge fields and more specifically to artificial magnetic fields. We would like to implement a scheme that simulates a strong magnetic field on a **two-dimensional cloud of fermionic potassium 40 atoms**. This way, it is possible to obtain fermions in a regime close to that of the quantum Hall effect.

We first shortly explain how other teams of ultracold science have already tried to simulate magnetic fields. Then, the concept of Berry's phase, very important in the field of artificial magnetic fields, is introduced. Finally, we present the scheme that we would like to implement on our experiment.

### 2.1 Previous simulation methods – the relevance of a wavefunction's phase

#### 2.1.1 Review of past methods for realizing artificial gauge fields

In this section, we start by giving a small overview of the past attempts at simulating magnetic fields with ultracold atoms and in particular explain the important case of stirred Bose-Einstein Condensates (BEC). Thanks to this, we would like the reader to get a sense of what are the important physical features occurring when a Lorentz force is governing the physics of a system, how the different implementation were improved step by step and ended up on the concept of optical flux lattice.

The first approach of the simulation of the effects of a magnetic field on neutral atoms was to rotate a cloud of ultracold atoms. The simple idea that lies behind this method is to see that the Lorentz force  $\vec{v} \times e\vec{B}$  and the Coriolis force  $\vec{v} \times \vec{\Omega}$  felt by an atom in a frame rotating at the angular speed  $\vec{\Omega}$  are formally the same: the higher the angular velocity, the higher the simulated magnetic field. Many groups have achieved that kind of simulation more than 10 years ago [8], [9] by rotating a BEC.

One of the most important results of such experiments was to show evidence for the

formation of vortices in the BEC (see Fig. 2.1). A rotating BEC exhibits the peculiar behaviour of actually responding to rotation only above a certain threshold. When the rotation is too slow, the BEC is not experiencing any change because it cannot turn as a whole due to its superfluid properties and it is not energetically favorable to form vortices. Vortices are positions in space where a vector is gradually rotated by a (non-zero) multiple of  $2\pi$  as one travels in a circle around that position. It can be, for instance, the direction of a flow's velocity. It forces the amplitude of the vector to vanish at the center of the vortex, where the direction of that vector cannot be defined. In the context of a rotating BEC, the macroscopic wavefunction's amplitude is the quantity that vanishes. That explains the “holes” one can observe on Fig. 2.1.

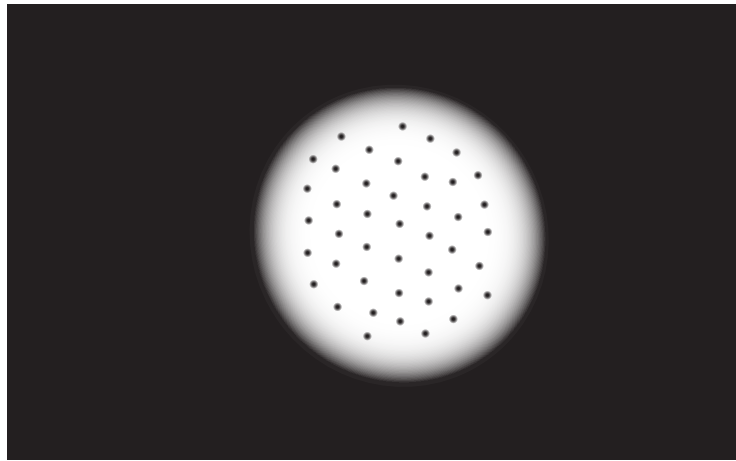


Figure 2.1: Schematic of how a BEC looks when it is stirred by lasers as in Ref.[9]. White indicates a non-vanishing density. The vortices (black dots) appear above a certain threshold of the rotating frequency and organize themselves automatically in a lattice.

The apparition of vortices was previously known in the context of superfluid helium but also in the theory of superconductors (so-called Type II superconductors), where a lattice of vortices also appears when a magnetic field is applied and is higher than a certain threshold. It meant already that, with stirred BECs, ultracold system where very useful to simulate systems that were seen as being specific to electronic solid state systems. Unfortunately, reaching very high rotation velocities is fraught with technical difficulties and that is why this technique is limited.

Ref.[10] shows how it is possible to create a vortex by adiabatically changing the direction of a magnetic field.

In the more recent attempt of Ref.[11], it has been shown that the magnetic field could be simulated by engineering a coupling of atomic internal states resulting from a position-dependent light-atom interaction. The results have been obtained by means of a Raman coupling between Zeeman substates of rubidium, which is in principle the same idea as the one we will develop in Sec. 2.3. In Ref.[11], the observation of the system yielded results that were very similar to what had been done with stirred BECs: several vortices,

where the atomic density is vanishing, have been directly detected. The relevant notion of Ref.[11] is the so-called *Berry’s phase*. Next section is devoted to an explanation of what a Berry’s phase is and we prove in next subsection that there is a direct link between the flux of a magnetic field coming from a vector potential  $\vec{A}(\vec{r})$  and the value of the phase of a quantum wavefunction, which determines where vortices are and how many are created. It follows from that link that vortices are the *flux carrier* in the system and that a high flux density corresponds to a high artificial magnetic field. The weakness of the scheme implemented in Ref.[11] is that the vortices are created on the scale of the whole ultracold cloud and the flux achieved that way is too low to get to more interesting regimes than what was demonstrated with stirred BECs. A natural idea is to have vortices appear on a smaller scale. An optical lattice looks here like a solution since it allows to have some quantities vary on a small length scale compared to the ultracold cloud’s size.

In one of the most recent publication about artificial gauge fields [12], an artificial magnetic field has been imitated by engineering a lattice where the hopping coefficient between lattice sites (in a Bose-Hubbard model) are complex. Atoms are loaded on plaquettes of four sites (forming a square); as they hop between adjacent sites, they can pick up a phase which is equivalent to a magnetic flux. This scheme occurs in a regime where atoms are strongly bound to the sites on the plaquette. In the optical flux lattice, we would like to have the advantage of the small scale of the lattice unit cell while departing from this regime of particle hopping and get closer to the free particle regime of an actual electron gas in two dimensions as achieved by solid state systems.

### 2.1.2 Explaining with equations

Here we would like to point out more explicitly the link between the phase of a quantum-mechanical system, the existence of vortices and the existence of a vector potential. This link explains the vortices in a stirred BEC.

The canonical momentum of a system with mass  $m$  and charge  $q$  submitted to a vector potential  $\vec{A}$  (such that the magnetic field is  $\vec{B} = \vec{\nabla} \times \vec{A}$ ) is  $\vec{p} = m\vec{v} + q\vec{A}$ . The De Broglie hypothesis states that it is possible to associate a wavevector  $\vec{k}$  defined by  $\hbar\vec{k} = \vec{p}$  to any quantum system. A wave can always be described as a superposition of plane waves  $(\vec{r}, t) \mapsto A_0 \exp(i\vec{k} \cdot \vec{r} - \omega t)$  with different amplitudes  $A_0$  and wavevector  $\vec{k}$ . For that reason, we focus on the phase  $\Phi = \omega t - \vec{k} \cdot \vec{r}$  of such a plane wave. The wavevector is given by  $\vec{k} = -\vec{\nabla}\Phi = \frac{m}{\hbar}\vec{v} + \frac{q}{\hbar}\vec{A}$ . The phase difference between two points in space  $\alpha$  and  $\beta$  is

$$\Phi_\beta - \Phi_\alpha = \int_\alpha^\beta \vec{\nabla}\Phi \cdot d\vec{r} = -\frac{m}{\hbar} \int_\alpha^\beta \vec{v}(\vec{r}) \cdot d\vec{r} - \frac{q}{\hbar} \int_\alpha^\beta \vec{A}(\vec{r}) \cdot d\vec{r}. \quad (2.1)$$

We see two components in the phase: one is imprinted by a velocity field and the other one is the *Aharonov-Bohm* phase which depends on the vector potential. That second component is famous for having been the tool used to prove the physicality of electromagnetic potential after the seminal work of Aharonov & Bohm in 1959 [13] has inspired experimentalists. This Aharonov-Bohm phase and the phase coming from the

velocity field are geometrical and not dynamical phase: it means that the phase picked up by a system along a path does not depend in any way on how the system moves along the path but only on where the path is in space. If the path is a closed loop we can write thanks to the Stokes' theorem:

$$\frac{q}{h} \oint_{\text{closed loop}} \vec{A} \cdot d\vec{r} = \frac{q}{h} \iint_S \vec{B} \cdot d\vec{S}. \quad (2.2)$$

This equality links the magnetic flux and the phase.

Let us get back to the important case of previous of the previous subsection. Stirring a condensate creates a position-dependent velocity field: the integral of  $\vec{\nabla}\Phi$  around a loop must be a multiple of  $2\pi$  for the wavefunction with phase  $\Phi$  to be single-valued and that leads to the quantization of circulation in the rotating BEC, where vortices carry the circulation quanta. We can see thanks to eq. (2.2) that quantification of circulation of  $\vec{A}$  and flux of  $\vec{B}$  are the same. Although the equivalence of the physical consequences of the Lorentz force and the Coriolis force is already obvious by writing the formulas defining these two forces, we can see that equivalence also by looking at the influence of the phase of a  $\vec{v}$  field and an  $\vec{A}$  field. More generally, any “trick” that creates a geometrical phase (the Aharonov-Bohm phase is only one example of that) can imitate the effect of a vector potential  $\vec{A}$ . Next section develops on how a geometrical phase can emerge for a quantum system with zero charge  $q$  without creating a velocity field  $\vec{v}(\vec{r})$ .

Let us quickly turn to another aspect of magnetic fields. It is essential to note that *a magnetic field breaks time-reversal symmetry* to the extent that the change  $t \rightarrow -t$  transforms  $\vec{B}$  into  $-\vec{B}$  as shown by the Maxwell-Ampère equation (see for instance in Ref.[14])

$$\vec{\nabla} \times \vec{B} = \mu_0 \vec{J} + \frac{1}{c^2} \frac{\partial \vec{E}}{\partial t}. \quad (2.3)$$

The current  $\vec{J} = \rho \vec{v}_{\text{charge}}$  comes from the velocity  $\vec{v}_{\text{charge}} = \frac{d\vec{r}_{\text{charge}}}{dt}$  of the spatial charge distribution  $\rho$ . Clearly, the solution of eq. (2.3) under  $t \rightarrow -t$  is  $-\vec{B}$ .

In Ref.[12], the phase picked up by an atom by travelling along a square plaquette (by hopings) is either  $-\phi$  or  $+\phi$ .  $\phi$  can be made arbitrary by tuning the frequency of some laser and this implies that  $+\phi$  and  $-\phi$  have different effects, which means that the Hamiltonian does change under time-reversal. This experiment was able to observe the fact that the Hamiltonian has a broken time-reversal symmetry. The asymmetry under time-reversal comes from the fact that the experiment have a running wave propagating with time, whereas usual scalar optical lattices are formed by a standing wave.

## 2.2 The Berry's phase

The central notion that we will use to explain how to implement an artificial gauge field on a lattice is the notion of *geometrical phase*, also called *Berry's phase* introduced in Ref.[15]. Let us develop on that concept.

We assume here Hilbert spaces with a finite basis. The adiabatic theorem states in mathematical terms that when one considers a system with a time-dependent Hamiltonian  $\hat{\mathcal{H}}(t)$  which has been prepared in an eigenstate corresponding to the eigenvalue  $\lambda_{\text{initial}} = \lambda(0)$ , that system will end up in the eigenstate corresponding to the final value  $\lambda_{\text{final}} = \lambda(t_f)$  of the time evolution of  $\lambda(t)$  (assuming  $\lambda$  is smoothly changing and isolated from other eigenvalues at all time) if the evolution between  $t = 0$  and  $t = t_f$  is slow enough. The faster it evolves, the more likely it is to end up in a superposition of eigenstates. In particular, if the Hamiltonian depends on some parameter  $G$  and  $G$  is changed adiabatically along a loop back to itself from  $t = 0$  to  $t = t_f$ , the state of the system (prepared in an eigenstate) comes back to the same eigenstate. As it holds for any  $t_f$ , we can assume *the state stays in an eigenstate during the whole travel*.

The most straightforward parameter one can think of is simply the position  $\vec{R}$  and a loop only means  $\vec{R}(0) = \vec{R}(t_f)$ . We can then write that the Hamiltonian  $\hat{H}(\vec{R})$  for every  $\vec{R}$  has an eigenbasis  $|n(\vec{R})\rangle$

$$\hat{H}(\vec{R})|n(\vec{R})\rangle = E_n(\vec{R})|n(\vec{R})\rangle$$

Here we suppose the system is travelling along a loop between time  $t = 0$  and  $t = t_f$ : originally in the state  $|n(\vec{R}(0))\rangle$ , the system goes back to  $|n(\vec{R}(t_f))\rangle = |n(\vec{R}(0))\rangle$  *up to a phase factor*. So we can arbitrarily write:

$$|\psi(t)\rangle = \exp\left(-\frac{i}{\hbar} \int_0^t E_n(t') dt'\right) \exp(i\gamma_n(t)) |n(\vec{R}(0))\rangle.$$

The phase  $\frac{1}{\hbar} \int_0^t E_n(t') dt'$  is the *dynamical phase* that the atom acquires from its time evolution. By plugging that in the time-dependent Schrödinger equation, one obtains:

$$\frac{d\gamma_n(t)}{dt} = i \dot{\vec{R}}(t) \cdot \langle n(\vec{R}(t)) | \vec{\nabla} n(\vec{R}(t)) \rangle.$$

So, around the closed loop  $\mathcal{C}$  in space we have :

$$\gamma_n(\mathcal{C}) = i \oint_{\mathcal{C}} \langle n(\vec{R}) | \vec{\nabla} n(\vec{R}) \rangle \cdot d\vec{R} \quad (2.4)$$

The quantity  $\langle n(\vec{R}) | \vec{\nabla} n(\vec{R}) \rangle$  is called the Berry connection and we can define the Berry flux as  $h\gamma_n(\mathcal{C})$  thanks to eqs. (2.1) & (2.2) with an arbitrary charge  $q = 1$ .  $\gamma_n(\mathcal{C})$  is just the circulation of the vector  $\langle n(\vec{R}) | \vec{\nabla} n(\vec{R}) \rangle$ . **The latter vector can be interpreted as a vector potential  $\vec{A}$  since its circulation induces a phase shift.**

The phase  $\gamma_n(\mathcal{C})$  is a geometrical phase called the Berry's phase and it depends only on the geometrical shape of the loop, regardless of how the system travels around it. One can now list the “ingredients” needed for a Berry's phase to appear: it comes up in the case of an adiabatic evolution of the position (or some other parameter) with a position-dependent Hamiltonian having position-dependent eigenstates. This is the general principle which has been implemented in Ref. [11].

We would like to make use of that principle in our experiment with a lattice-like scheme, which allows to generate higher artificial magnetic fields and gives the opportunity to study topological properties of the system. Since the magnetic flux through a surface  $S$  is, by definition, the integral of  $d\Phi = \vec{B} \cdot d\vec{S}$ , the flux density  $\frac{d\Phi}{dS}$  is the magnetic field. The vortices being in some way the “flux carrier”, achieving a high density of vortices is equivalent to achieving a high  $\|\vec{B}\|$ .

The Berry's phase is not only an attribute of quantum mechanics. It can be encountered in the context of the rotation of the oscillation of a Foucault pendulum or the rotation of the polarization of the light going through a (polarization maintaining) optical fiber. When one moves a vector on the surface of a sphere while maintaining its orientation *as defined locally along the curvature of the sphere* and not according to the usual orientation of the (Euclidean) flat space the sphere is embedded in, the vector is rotated when travelling around a loop. This is a matter of differential geometry in curved space.

## 2.3 Optical flux lattices

The goal of this section is to show that we can manage to create a position-dependent light field that would gather the necessary condition for a Berry's phase to appear and simulate the effect of a vector potential. This scheme would be applied to a *two-dimensional cloud of ultracold fermions* in order to be as close as possible to an electronic sample where quantum Hall effect emerges (*e.g* in Ref.[6]), hoping for such an effect to eventually show in a system of neutral ultracold atoms. Being close to the condition of quantum Hall physics in solid state means having a high enough flux density and nearly free particles.

We give here an overview of the principle presented in Refs [16] and [17].

The “simple” configuration, presented in Fig. 2.2 assumes that we have an atom possessing a ground state with angular momentum quantum number  $J = 1/2$  and an optical transition to an excited state with the same  $J$ . The angular momentum subspace of the ground state contains two states  $|g_+\rangle$  and  $|g_-\rangle$ , which are  $|J = \frac{1}{2}; m_J = \pm \frac{1}{2}\rangle$ ; for the excited state, there is also  $|e_+\rangle$  and  $|e_-\rangle$ .  $|g_+\rangle$  and  $|g_-\rangle$  (respectively,  $|e_+\rangle$  and  $|e_-\rangle$ ) are degenerate in the absence of a magnetic field but thanks to the Zeeman effect, it is possible to lift the degeneracy and split them with an energy difference  $\delta_0 = E_{g+} - E_{g-}$ . When the system {light+atom} is considered,  $|g_\pm\rangle$  are not the eigenstates anymore and from the existence of the position-dependent light-atom coupling follows the existence of the position-dependent  $|n(\vec{R})\rangle$  of last section. Such position-dependent couplings *i.e* non-vanishing off-diagonal

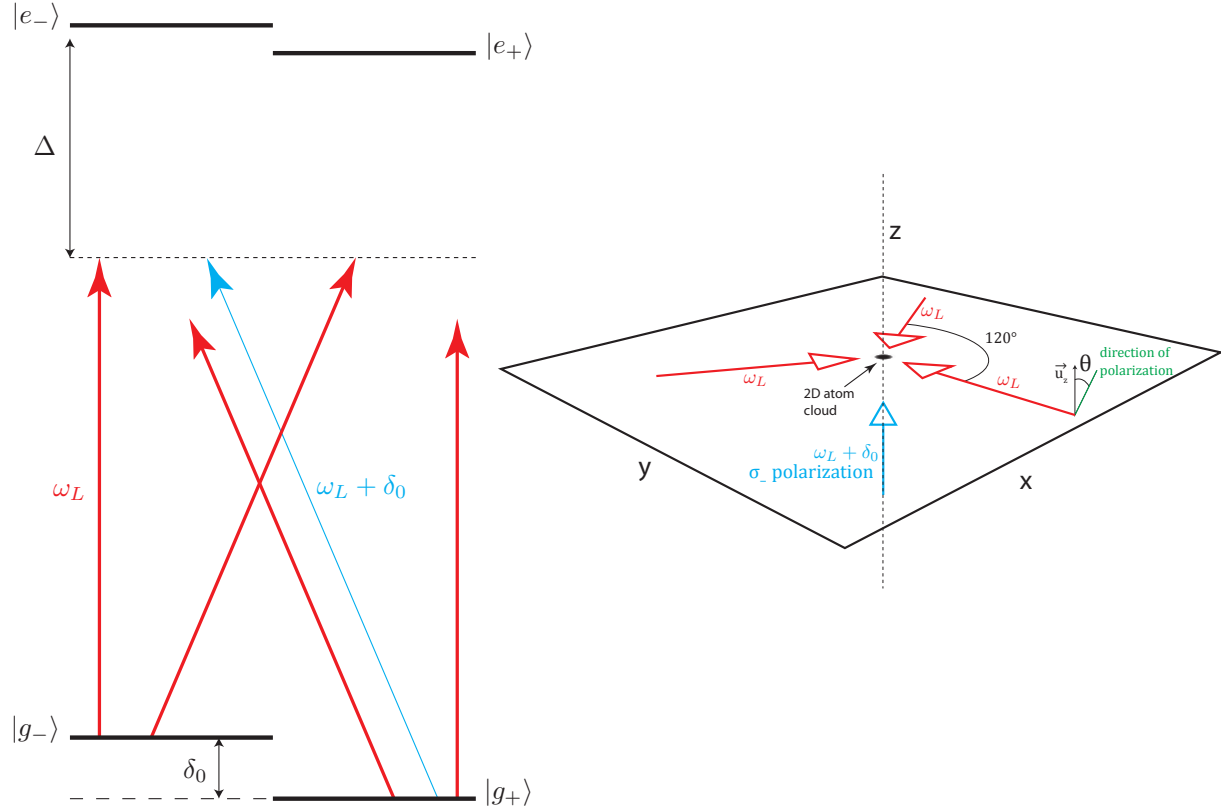


Figure 2.2: Left side: red and blue arrows show the different couplings induced by laser beams between the states in an energy diagram. We recall graphically how  $\Delta$  and  $\delta_0$  are defined. This figure is not to scale: in reality  $\Delta \gg \delta_0$ .

Right side: we draw how the four beams used for the scheme have to be placed in space and how their polarization has to be set.

matrix elements of the Hamiltonian in the basis  $\{|g_+\rangle, |g_-\rangle\}$  are produced by means of Raman transitions between  $|g_+\rangle$  and  $|g_-\rangle$ . The Hamiltonian having such coupling is very different from the scalar Hamiltonian

$$V(\vec{r}) \begin{bmatrix} 1 & 0 \\ 0 & 1 \end{bmatrix} = V(\vec{r}) \hat{\mathbb{1}}, V(\vec{r}) \in \mathbb{R}$$

used in usual optical lattice experiment (such as in Ref.[18]).

The system is characterized by three one-photon Rabi frequencies  $\kappa_m$  which couple  $|g_\pm\rangle$  and  $|e_\pm\rangle$ . The  $\kappa_m$ 's are related to the dipole operator  $\hat{d} = -e\hat{r}$ .

$$\hbar\kappa_+ = \langle g_- | \vec{E}_{\text{total}}(\vec{r}) \cdot \hat{\vec{d}} | e_+ \rangle. \quad (2.5)$$

$\vec{E}_{\text{total}}$  is along the polarization unit vector  $\vec{\epsilon}$ .  $\hat{\vec{r}}$  is the quantum-mechanical position operator.

Inverting + and – in  $\kappa_+$  gives  $\kappa_-$ .  $\hbar\kappa_0$  is the matrix element between  $|g_+\rangle$  and  $|e_+\rangle$  or between  $|g_-\rangle$  and  $|e_-\rangle$ .

We consider three beams at frequency  $\omega_L$  propagating in the same  $xy$ -plane at an angle of  $2\pi/3$  rad with respect to each other.  $z$  is the direction normal to the  $xy$  plane. Each of the three beams is linearly ( $\pi$ ) polarized at an angle  $\theta$  to the unit vector  $\vec{u}_z$  of the  $z$  axis (see Fig. 2.2). We model these beams by simple plane waves with amplitude  $E_0$ . So the electric field we have in that case is the sum  $E_{\text{total}}(\vec{r})e^{-i\omega_L t}$  with:

$$\vec{E}_{\text{total}}(\vec{r}) = E_0 \left( \sum_{l=1}^3 e^{i\vec{k}_l \cdot \vec{r}} \left[ \cos(\theta) \vec{u}_z + \sin(\theta) \left( \vec{u}_z \times \frac{\vec{k}_l}{||\vec{k}_l||} \right) \right] \right) \quad (2.6)$$

The quantity in bracket is just the unit polarization vector of each beam.

Using the definition of eq. (2.5) and eq. (2.6), the resulting Rabi frequency is

$$\kappa_+ = \underbrace{\frac{-eE_0}{\hbar} \langle g_- | \hat{r} | e_+ \rangle}_{\text{"vector frequency" } \vec{\kappa}} \cdot \sum_{l=1}^3 e^{i\vec{k}_l \cdot \vec{r}} \left[ \cos(\theta) \vec{u}_z + \sin(\theta) \left( \vec{u}_z \times \frac{\vec{k}_l}{||\vec{k}_l||} \right) \right] \quad (2.7)$$

We suppose also that one beam with frequency  $\omega_L + \delta_0$  is propagating in the direction perpendicular to the three other beams, has a Rabi frequency  $\Omega_\sigma$  and is circularly ( $\sigma_-$ ) polarized. Due to the selection rules, that beam only couples  $|g_+\rangle$  to  $|e_-\rangle$ . We assume  $\delta_0 \gg \kappa_\pm, \kappa_0$  and  $\Delta \gg \delta_0$ .

In the case  $\Omega_\sigma = 0$ , the three in-plane beams alone form either a hexagonal lattice or a triangular one depending on the sign of  $\Delta$  and the value of  $\theta$ . This is illustrated in Fig. 2.3. Such a scalar optical potential can be used to simulate graphene physics (see Ref.[19] for more).

We recall here the idea of Raman transitions: the one-photon coupling at  $\omega_L$  is very far detuned by  $\Delta = (\omega_{e \rightarrow g}) - \omega_L$  from the  $|g\rangle \rightarrow |e\rangle$  transition and so there is negligible coupling between ground and excited states as well as negligible occupancy of excited states; on the other hand, the two-photon coupling is in or near resonance with the  $|g_+\rangle \rightarrow |g_-\rangle$  transition via the virtual state  $|e_-\rangle$  which creates a coupling between  $|g_+\rangle$  and  $|g_-\rangle$ . Nevertheless the one-photon couplings do generate a light shift which scales like  $\frac{|\kappa_m|^2}{\Delta}$  with a proportionality constant  $C$  and it pushes down  $|g_+\rangle$  and  $|g_-\rangle$  by respectively  $C|\kappa_+|^2/\Delta$  and  $C|\kappa_-|^2/\Delta$ , resulting in pushing apart (algebraically, which means they can be pushed closer to each other) the eigenvalues of the two levels and creating a detuning

$$D \propto \frac{1}{\Delta} (|\kappa_+|^2 - |\kappa_-|^2).$$

The Raman coupling is coming from the  $\Lambda$  system formed by  $|g_+\rangle$ ,  $|e_-\rangle$  and  $|g_-\rangle$ . As a result, the “Raman Rabi frequency”, also called *two-photon Rabi frequency* is

$$K_{\text{Raman}} \propto \Omega_\sigma \kappa_0 / \Delta.$$

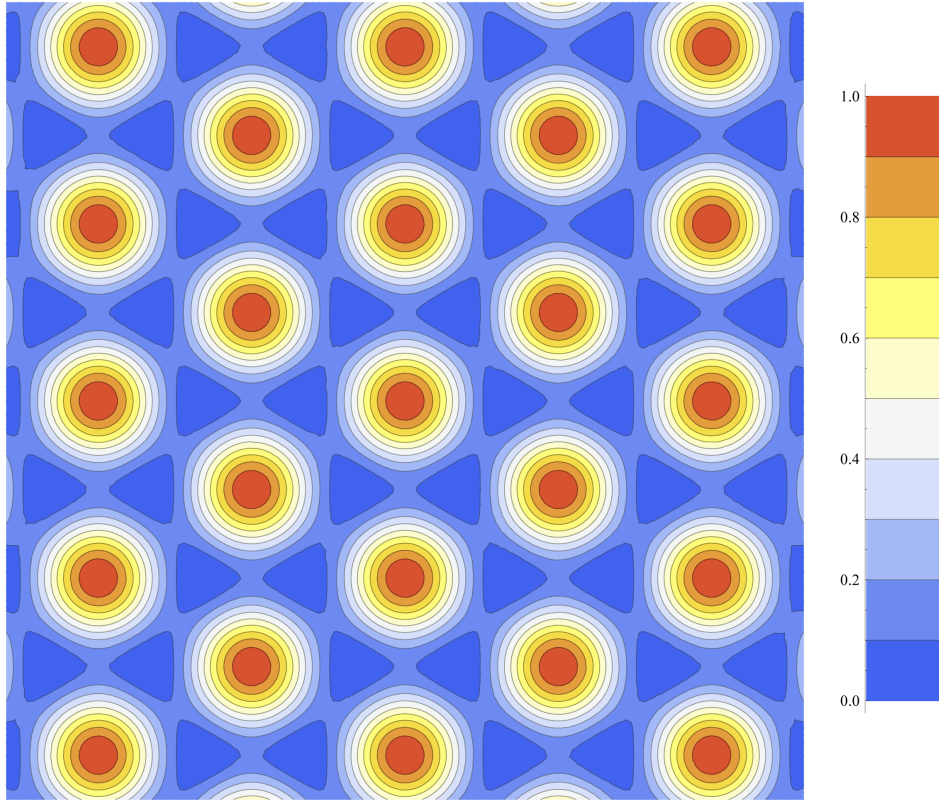


Figure 2.3: This contour plot shows the normalized scalar potential obtained with three beams in the same plane with an angle of  $120^\circ$  to each other *i.e*  $\|\vec{E}_{\text{total}}(\vec{r})\|^2$ . It generates a triangular lattice (maxima, in red on this figure) or an hexagonal lattice (minima, in blue on this figure) depending on the sign of the detuning.

It is important to see that the tilt  $\theta$  of the polarization plane of the beams at  $\omega_L$  implies that their polarization has a non-zero component of  $\sigma_+$  and  $\sigma_-$  light in the  $xy$  plane where the three beams at  $\omega_L$  propagate: from that follows that there is a coupling  $|g_-\rangle \leftrightarrow |e_+\rangle$  and  $|g_+\rangle \leftrightarrow |e_-\rangle$  (red slanting arrows in Fig. 2.2). This could lead to a two photon-coupling with two photons from the in-plane beams at  $\omega_L$ . We want the two photon coupling to come dominantly from the transition with one photon of the vertical beam at  $\omega_L + \delta_0$  and one-photon from the beams at  $\omega_L$ . The transition with two photons at  $\omega_L$  is indeed negligible because it is off resonance by  $\delta_0 \gg \kappa_{\pm}, \kappa_0$ .

So, as stated in Ref.[17], the resulting effective Hamiltonian  $\hat{H}_{\text{Raman}}$  for the ground state manifold  $\{|g_+\rangle, |g_-\rangle\}$  is

$$\hat{H}_{\text{Raman}} = \begin{bmatrix} D & K_{\text{Raman}} \\ K_{\text{Raman}}^* & -D \end{bmatrix} \propto \frac{1}{\Delta} \begin{bmatrix} |\kappa_+|^2 - |\kappa_-|^2 & \Omega_\sigma \kappa_0 \\ \Omega_\sigma \kappa_0^* & |\kappa_-|^2 - |\kappa_+|^2 \end{bmatrix}.$$

Since  $\kappa_0$  is obviously position-dependent, we have a position-dependent coupling be-

tween  $|g_+\rangle$  and  $|g_-\rangle$ . The two eigenstates  $|\rho_{\pm}(\vec{r})\rangle$  of that Hamiltonian are the so-called *dressed states*: they are the eigenstates of the system formed by assembling the light field and the internal levels into one system.  $\kappa_{\pm}$  are also obviously position-dependent and that creates a spin-dependent potential

$$U(\vec{r}) \begin{bmatrix} 1 & 0 \\ 0 & -1 \end{bmatrix}$$

as opposed to the spin-independent scalar potential  $V(\vec{r})\hat{1}$  of the scalar optical lattices.

A Rabi frequency is a complex quantity associated with Rabi oscillations of a Bloch vector (supposed to have been prepared in one eigenstate): the magnitude of that Rabi frequency is just the angular frequency at which the vector rotates, its complex phase represents the azimuthal angle of the axis of the rotation. In addition, the detuning defines the polar angle of the axis of rotation *i.e* how close it gets from the other eigenstate during the Rabi oscillation. Here we can associate a Rabi oscillation to the two-photon Rabi frequency  $K_{\text{Raman}}$  and the detuning  $D$ . Where  $\kappa_0$  vanishes, the coupling vanishes and it corresponds to a situation where the Bloch vector would just stay fixed. Such locations of zero coupling are singularities of the coupling, where the magnitude of the rotation is well-defined and equal to zero but not the phase, which can be fixed at any arbitrary value. Around these singularities, the phase of the coupling happens to wind as shown in Fig. 2.4. Such location in the lattice thus correspond to vortices of the complex phase of  $K_{\text{Raman}}$ . The arrows of Fig. 2.4 show the magnitude and phase of the coupling between  $|g_+\rangle$  and  $|g_-\rangle$  across an hexagonal plaquette and how they form a lattice of vortices. Unlike the case of a BEC in the rotating frame as shown in Fig. 2.1, the vortex do not lead to a “hole” in the cloud with an atoms’ density equal to zero because there is two species differing by their internal state in the cloud.

The flux lattice has two very important properties:

- it has a *net flux per unit cell* carried by the two vortices contained in each unit cell (a vortex and an antivortex) and so an average net flux density  $n_{\phi}$  just like a system with a real magnetic field. Indeed, the vortices and antivortices do not cancel out because the sign of  $|\kappa_+|^2 - |\kappa_-|^2$ , which is the hemisphere in which the Bloch vector points alternate between vortices and antivortices. This is not trivial and is not the case in the proposal of the same type explained in Ref[20].
- $n_{\phi}$  is high in the following sense: a unit flux quantum is contained in an area of the order of  $\lambda_L^2$  in the scheme we are explaining here. In the past ten years, following the seminal work of Ref.[18], many-body systems of ultracold atom with a density in the order of one atom per lattice site on the  $\lambda_L^2$  has routinely been achieved. Consequently, it is a very realistic goal to reach the regime where  $n_{\phi}$  is on the same order of magnitude than the particle density. That regime, added to strong interaction between charged particles corresponds to a strongly correlated system where the quantum Hall physics come into play [21]. The strength of the artificial magnetic field reached by would be orders of magnitude higher

than for other previous methods (Ref.[11] for example).

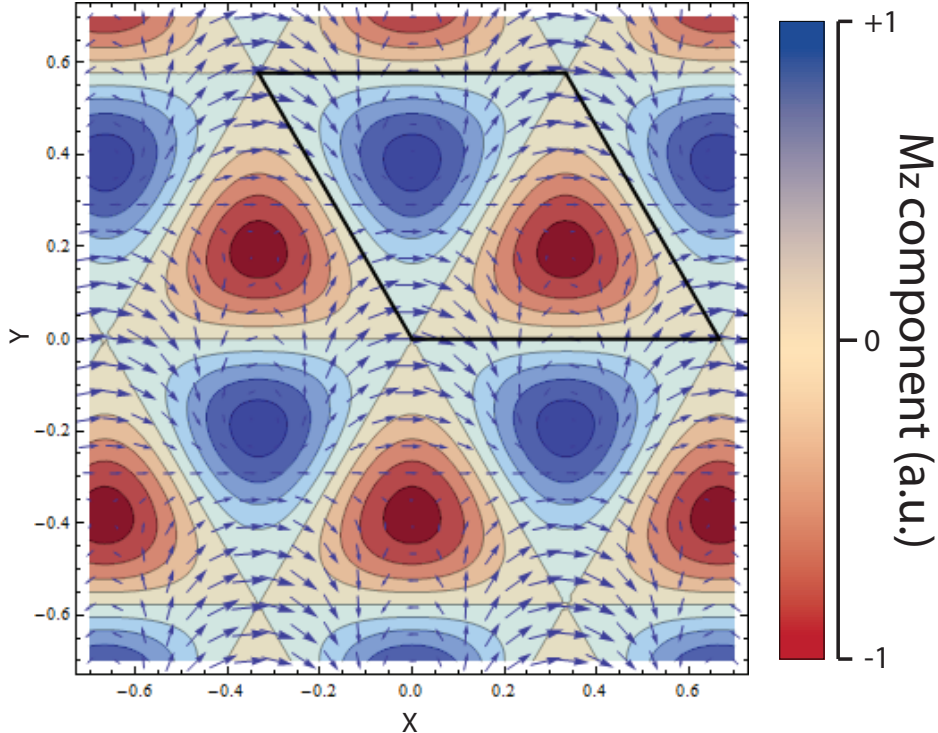


Figure 2.4: In the above picture, the color shows the level lines of the the real diagonal terms of the Hamiltonian  $\hat{H}_{\text{Raman}}$ : they form an internal state-dependent potential. Where a  $|g_-\rangle$  is maximally trapped,  $|g_+\rangle$  is minimally and *vice versa*. The arrows shows the magnitude (size of the arrow) and complex phase (direction of the arrow) of the coupling (off-diagonal term) of  $K_{\text{Raman}}$  of  $\hat{H}_{\text{Raman}}$ . One can see that vortices are in opposite directions around a maximum (red) and a minimum (blue). The thicker black line denotes the unit cell.

Now if we suppose the kinetic energy small enough, the atom move adiabatically. Thus they experience the Berry phase given by the integral  $i\langle\rho(\vec{r})|\vec{\nabla}\rho(\vec{r})\rangle$  (according to eq. (2.4)) as they move around the lattice.

We mentioned at the beginning of this chapter that quantum simulation was about engineering Hamiltonian. Therefore the ultimate proof that a system simulates another in theory is to show the emergence of the same Hamiltonian. That was an obvious step in the case mentioned in Sec. 2.1 of the simulation by studying the BEC in a rotating frame. As suggested in Ref.[22] and derived in Appendix B, one can show that the adiabatic elimination of one of the two state leads to a term in the form

$$\frac{(\hat{\vec{p}} - \hat{\vec{A}})^2}{2m}$$

in the Schrödinger equation describing a particle having position-dependent eigenstates. This is exactly the Hamiltonian of a particle with charge 1 in a magnetic field.

The strength of the lattice is characterized by  $\mathcal{V} = \frac{\hbar^2 ||\vec{\kappa}||^2}{\Delta}$  and we know that  $||\vec{\kappa}||^2$  is proportional to the intensity of one beam since that intensity is  $I = \frac{c}{2} n \epsilon_0 E_0^2$  for a plane wave with an electric field amplitude  $E_0$  in an optical index  $n$ ; the kinetic energy scale of the lattice is the recoil energy  $E_R = \frac{(\hbar k_L)^2}{2m_K}$  of one K atom for a photon of wavevector  $k_L$ . The condition of low kinetic energy can be expressed as  $\mathcal{V} \gg E_R$ . In that case of high potential, atoms are tight in the minima of the lattice (like in Ref.[12]) – the so-called *tight-binding limit* – and can only move by hopping from one lattice site to a neighbouring one. Whether it be in the case of the hexagonal or triangular lattice geometry, the only possible way to travel along a closed loop is to enclose an integer number of plaquettes. Each plaquette carries an integer number of flux number. Thus the phase

$$\phi = \frac{q}{h} \oint_{\text{closed loop}} \vec{A} \cdot d\vec{r}$$

which we can write using Stokes' theorem

$$\phi = \frac{q}{h} \iint_S \vec{B} \cdot d\vec{S}$$

is a multiple of  $2\pi$ : travelling along the loop in one direction – *i.e* multiplying by the phase factor  $e^{i\phi}$  – or the other – *i.e* multiplying by  $e^{-i\phi}$  – does not make any difference. In that case, although there is a Berry's phase associated with the lattice, the atoms are constrained in such a way that physical features uniquely associated with the presence of a magnetic field cannot be detected.

We want to avoid this case of little interest and need to obtain a system where *time-reversal symmetry is broken*: for that purpose, it is possible to work in the regime  $\mathcal{V} \sim E_R$ . In that case, where second-neighbour hopping is enabled and atoms are not too much pinned to the minima of the lattice, they travel more freely around loops enclosing a wider range of phases which allow time-reversal symmetry to be broken. In this scheme, the part of the setup that allows time-reversal symmetry to be broken is the circularly polarized light.

In order to show that the system does mimic a system of electrons in a magnetic field to some extent despite the absence of the important condition of adiabaticity, band structure calculations have been performed by exact diagonalization of the Hamiltonian. That procedure tells that the system still has a very interesting behaviour: the first band can become very flat with a correct set of parameter  $\theta, \vec{\kappa}, \omega_L, \Delta$  and  $\delta_0$ . This resembles very much the band structures of electrons in a two-dimensional system submitted to a strong magnetic field, which all occupy the lowest Landau level forming a flat band. More importantly the band structure has topological properties coming from the net flux per unit cell. This latter property is very robust again change of some parameters, just as the value of the quantized resistance of electronic system in the quantum Hall effect is very robust against the geometry or the purity of the sample [23].

## 2.4 Adapting the scheme to potassium

### 2.4.1 Accommodating the above ideas to a real multi-level atom

The transition of the fermionic species potassium 40 we would like to work with is not as simple as the one used in the model described in last section. It requires to be adapted. The ground and excited states have many  $m_F$  levels contrary to the case considered in previous section with two levels in each. The ground state is  $4^2S_{1/2}$  in spectroscopic notation with  $F = 9/2$  and  $F = 7/2$ . The fine structure Hamiltonian splits the dipole transition  $4S \rightarrow 4P$  into two transitions (the D1 line  $4S \rightarrow 4P_{1/2}$  at  $\lambda_{D1} = 770,1\text{nm}$  and D2 line  $4S \rightarrow 4P_{3/2}$  at  $\lambda_{D2} = 766,7\text{nm}$ ).

Even if we have many  $m_F$  states, we would like to have the system behave as much as possible like a “two  $|g\rangle$ , two  $|e\rangle$ ” atom. In order to achieve this, one uses the *quadratic Zeeman shift*, which shifts the energy of an atom in a uniform magnetic field  $\vec{B}_0$  by an amount proportional to  $\vec{B}_0^2$ . It allows us to make sure that, with a fixed two-photon coupling, the  $m_F$  states outside a set of two ground  $m_F$  states (say,  $|g; m_F = M - 1/2\rangle$  and  $|g; m_F = M + 1/2\rangle$ ) and two excited  $m_F$  (also  $|e; M - 1/2\rangle$  and  $|e; M + 1/2\rangle$ ) states are off resonant and that we will never induce a transition outside  $M - 1/2$  and  $M + 1/2$ . This gives the magnetic field we want to work at and also the Zeeman shift  $\delta_0$ .

We recall the fact that there are three components  $\sigma_{\pm}, \sigma_0$  of the light at  $\omega_L$  due to the tilt  $\theta$  of the  $\pi$  polarized light and that they all produce a light shift. These three light shifts give rise to three potentials that superimpose on each other. For each component, there is a light shift from the D1 transition and another from the D2 transition and the light shift scales like  $|\kappa_m|^2/\Delta$ . In the case of an optical lattice, it is the *amplitude of the lattice potential* that scales like  $|\kappa_m|^2/\Delta$ : the closer to resonance with one line, the deeper the lattice relative to this line. Between the D1 and D2 lines, there is a balance point, having opposite sign of detuning  $\Delta$  and same lattice amplitude. This balance point is not  $(\omega_{D1} + \omega_{D2})/2$  because the transition strengths – matrix elements of the dipole operator between  $4S$  and  $4P_{3/2}$  or  $4P_{1/2}$  – are not equal for both lines. The D2 line is quite accurately twice as strong as the D1 line [24]. We can conclude that the balanced point is roughly a distance of  $2/3(\nu_{D2} - \nu_{D1})$  in detuning from the D2 line; numerically, that means that we want to be around 769nm. It is not possible to reach the balanced point of potentials for each components at the same time but if one is set to 0, the other two are still very shallow.

More precisely, the light shift we want to get rid of in order to be as close as possible to a “two  $|g\rangle$ , two  $|e\rangle$ ” atom come from the coupling between  $|g; M + 1/2\rangle$  and  $|e; M + 3/2\rangle$  or between  $|g; M - 1/2\rangle$  and  $|e; M - 3/2\rangle$ . The cancellation of this light shifts sets a finer tuning of the wavelength.

Unfortunately, things are not quite so “simple” because we are considering an atom subjected at a rather high magnetic field  $\sim 300\text{G}$  that prevents us from using  $m_F$  as a good quantum number to describe the atomic eigenstates but the idea of cancelling light shifts to keep the potential shallow still holds.

### 2.4.2 Summary of the experimental requirement

For the actual implementation of the optical flux lattice scheme explained here, we need four lasers. According to full calculations done by M. Schleier-Smith, the intensity needed would be  $I_0 \approx 3 \cdot 10^4 I_{\text{sat}}$  per in-plane beams and about  $1,4 \cdot 10^3 I_{\text{sat}}$  in the vertical beam, where  $I_{\text{sat}} \approx 1,75 \text{mW/cm}^2$ . We would like to have a homogeneous light because it would generate a homogeneous lattice depth. The output of fibers – used to carry light from the optical table where light is prepared to the table where the experiment where atoms are cooled down – are very close to a Gaussian beam profile. We can have an idea of the needed power with that approximation. Fig. 2.5 shows (not to scale) the situation corresponding to the following calculations.

At the waist (location of minimum extension), such a beam is constant and equal to its center intensity within 2% in a disk with a radius of 10% of the waist  $w_0$ . A realistic size for the atom cloud is around  $50\mu\text{m}$  of radius [25]. That corresponds to  $w_0 = 50\mu\text{m}/10\% = 5 \cdot 10^{-2}\text{cm}$ . The total power of Gaussian beam with a center intensity of  $I_0$  at the waist is  $\frac{\pi}{2} I_0 w_0^2$  (for instance Ref.[26]): it yields about  $200\text{mW}$  per in-plane beam. This power is not the right amount because the system is a two-dimensional and so very thin in the plane of the three beams at  $\omega_L$ ; it means that the beam can be much shorter vertically than horizontally and that, instead of being round, it will be elliptical and very elongated. This last fact allows to reduce the power we need by a factor 10.  $20\text{mW}$  is the right amount of power and we would like to reach at least  $100\text{mW}$  to be on the safe side and be also able to test physics with deeper lattices than what is required in the implementation of the optical flux lattice. We can conclude that, with  $100\text{mW}$  maximum power per in-plane beam, we can have enough intensity for an optical flux lattice with little anisotropy of the potential as well as an alignment process which would not be too hard. The circularly polarized beam needs around 20 times less intensity; however, it cannot be thin in one direction and must for that reason have around  $10\text{mW}$ .

The frequency difference  $\delta_0$  for the laser beams can be obtained via **Acousto-Optical Modulators** (AOM) and will be around  $130\text{MHz}$ . For that frequency, we can use the difference between a  $80\text{MHz}$  AOM and a  $200\text{MHz}$  AOM slightly detuned from their center frequency. For the energy levels of the atom, splitting the Zeeman sub-levels by  $\delta_0$  at  $300\text{G}$  entails the use of a highly stable magnetic field: that is the object of the master thesis of H. Lüschen in the same laboratory.

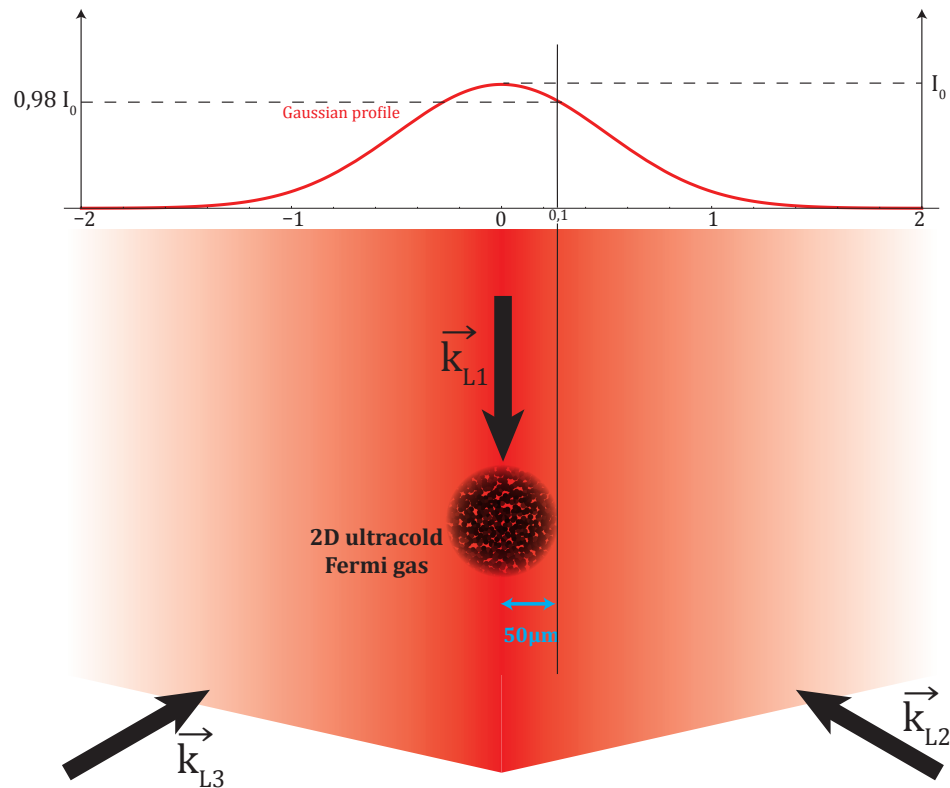


Figure 2.5: Visual explanation of the position of the 2D ultracold cloud at the intersection of the three in-plane beams with a frequency  $\omega_L$  and wavevector  $\vec{k}_{L1}, \vec{k}_{L2}, \vec{k}_{L3}$ . This figure is obviously not to scale. The quantities displayed here are an approximation of what could be the final parameters of the beam and the cloud. The curve is the intensity of one beam *vs.* distance in unit of the waist  $w_0$ . The gradient of red color represents laser light for one beam with wavevector  $\vec{k}_{L1}$  out of three beams in total.



# Chapter 3

## Experimental setup

In last chapter, we determined right from the start in the explanation of the experimental implementation of the optical flux lattice that we needed four beams as shown in Fig. 2.2. We concluded by mentioning the important parameters  $\lambda_L$ ,  $\delta_0$  as well as the power we must have in each beam. A convenient way to reach the desired power, which is mostly contained in the three in-plane beams is to use semiconductor lasers. For that power range, a simple laser diode is not enough since it cannot output more than 70mW in most cases and we would like to obtain all beams by separating one single beam: it is better in terms of noise and it potentially spares space on the optical table. The option chosen is to use a semiconductor **Tapered Amplifier** (TA) which can output around 1W.

The first problem that we encountered is that the spectrum of the TA contains a weak but broad background extending beyond the wavelengths of the D1 and D2 line and consequently contains resonant light, which is likely to heat up the atoms. This chapter, after having shown an overview with all the components of the setup, will explain more specifically how we tackled that issue. The second main problem we had was to avoid phase noise between each beam which is dealt with in next chapter.

### 3.1 The Raman setup

Let us now describe the whole of the setup, shown in Fig. 3.1 before we get to the problem posed by the use of a TA at  $\lambda_L = 769,1\text{nm}$ .

The light is generated by the TA and then sent in a quartz, 30cm long vapor cell containing natural – hence non-enriched – potassium. That cell is heated up with a heating tape (HILLESHEIM HST-020) to maximum 120°C which corresponds to a voltage of 35-40V. The tape is not wound directly around the cell but on an aluminium oven that contains it and allows to easily integrate the cell in the setup on the bread board. Some pictures of the oven and the cell are shown in Appendix C. The wound up oven is then wrapped in aluminium foil for insulation in order to prevent the heating to induce too much loss in air and grounded to avoid electrical shock in case something goes wrong with the heating tape and the aluminium becomes connected to the 40V.

After that the beam is separated three times in a row into four beams using a  $\lambda/2$ -plate followed by a polarizing cube splitter.

For each of the four beams, the following happens:

- about 8% of it is picked off by a glass plate and is shone on a HAMAMATSU G4176 fast photodetector (after a back-reflection off a mirror). The remaining 92% percent is focused into an AOM where the frequency is shifted. Then, another lens is used to adapt the beam size and that beam with a modified size is coupled to a fiber.

- The far end of the fiber is cut perpendicular to its propagation axis and reflects back a few percent of the light while the rest is focused on the atom cloud. That light propagating backwards goes again through the fiber, the AOM, 8% is picked off again in a compact interferometer and shone onto the fast photodetector, creating a beat note that we use for the phase lock (see next chapter).

## 3.2 The semiconductor tapered amplifier

The so-called TA laser contains first a diode laser with a grating-based external cavity then an optical isolator – also called optical diode – followed by the amplifier. The diode laser's light needs to be coupled into the amplifier, which is done here via a collimating lens. To achieve this, one uses the strong spontaneous emission visible when the TA is injected with a current (in excess of 1A) without an input beam. The first step of alignment is to center the diode's beam in the middle of that spontaneously emitted light. From then on, one can see an amplified output of the TA and monitor it with a photodiode or a power-meter – the photodiode is better because much faster – and walk the coupling to achieve the most power possible. The amplifier has two collimating lenses at the input and output: tuning the position of the input collimator helps achieving more output power and tuning the position of the output collimator is needed to get a symmetrical mode. The amplifier's output beam is very divergent in the vertical direction – even after the collimator – and this is corrected for by a cylindrical lens positioned right after the amplifier. A second optical isolator is mounted after that cylindrical lens and the beam is ready for further use with a power of about 1W at the output of the second optical diode. Slightly more power could be achieved by using better optical isolators: we found it hard to reach a high isolation – *i.e* transmission in the blocking direction – while having a good transmission in the passing direction: the compromise was  $10^4$  absorption with about 70% transmission. Supposedly the wavelength is on the edge of the operating range of the isolator which is made for 790nm light and have better performance for Rb-related wavelengths as opposed to the K-related wavelengths we have in the experiment described here.

A semiconductor amplifier with a tapered gain region (full name of a TA) is injected with a current of  $\sim 2,5$ A: as the *main intensity peak* of the seed diode laser is being amplified through stimulated emission, the power contained in the wings of the amplified laser spectrum also increases because photons that are spontaneously emitted in the gain medium can also be amplified. Although that part of the light is not temporally nor, in principle,

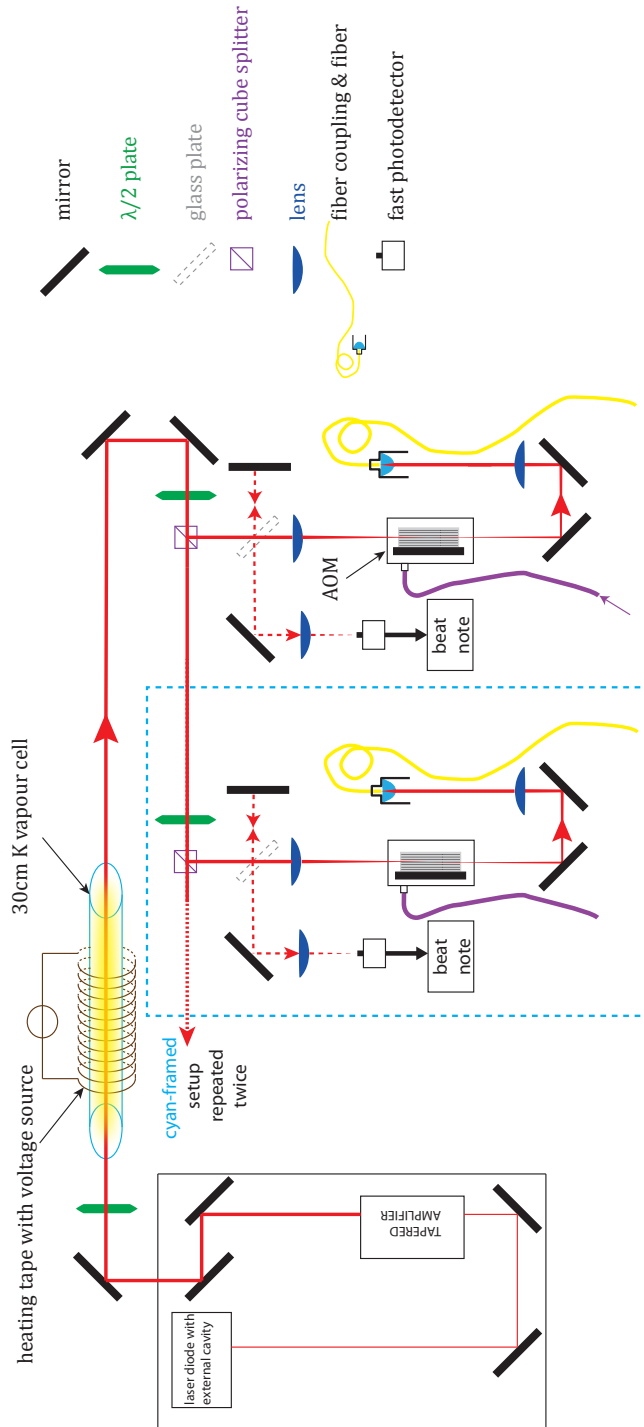


Figure 3.1: This figure shows the whole optical path from the laser diode to the fiber coupling. The setup is formed of 4 beams, the frequency of which is individually controlled by an AOM.

spatially coherent, the gain medium shape favors some specific directions and that amplified spontaneous emission is added to the mean peak. Amplified spontaneous emission can in some applications prove useful when one needs light without time coherence but with some degree of spatial coherence. For the wavelength needed to generate the flux lattice – namely 769,1nm – the *unwanted resonant light* in the wings of the spectrum on the D1 and D2 transition lines respectively at 770,1nm (1nm away from the peak) and at 766,7nm (2,4nm away from the peak) would lead to significant and even dominant scattering rate – as will be shown by in Sec. 3.3.2 – compared with that of the light of the 769,1nm peak we would actually be manipulating the atoms with.

The absorption of that parasite light by the cold atom cloud would lead to heating and to uncontrollable changes of internal states, considerably reducing the coherence time of the atoms during the experimental sequence; the point that needs also to be emphasized here is that the emergence of an artificial vector potential comes from the internal state dependence of the potential. For that reason, it is clear that we want to get rid as much as possible of any process adding some kind of randomness in the way atoms jump between their internal states.

Spectra are measured by an optical spectrum analyser ANDO AQ6315-E and gives us a power spectral density in dBm/nm. The device has a maximal resolution bandwidth of  $\Delta\lambda = 50\text{pm}$ ; 50pm at 770nm corresponds to 25GHz. This means it cannot make a difference between one peak containing  $X$  dBm in an interval  $[\lambda_0; \lambda_0 + \Delta\lambda]$  and any other power density profile (for instance two peaks) having  $X$  dBm in the same interval; the measurement is done with an increment of 5 pm.

Fig. 3.2 shows us the spectra of the diode and of the TA for comparison. We do see that also at large detuning the spectrum of the TA is quite far from reaching the noise floor: that is an evidence of the presence of a strong spontaneous emission. Using the EagleEye Fabry-Pérot cavity we measured the linewidth of the laser diode to be about 700kHz. As a result the spectrum of the laser diode seen with a high enough resolution is in fact much narrower than what we see in Fig. 3.2 and the resolution of the ANDO AQ6315-E is quite poor for our application.

### 3.3 Attenuation of resonant light in a vapor cell

In this section, we first want to determine how much we have to attenuate the resonant light of the amplified spontaneous emission in order to make it smaller or even negligible compared to the scattering due to the main peak at 769nm. After that, we measure the attenuation with different methods and conclude.

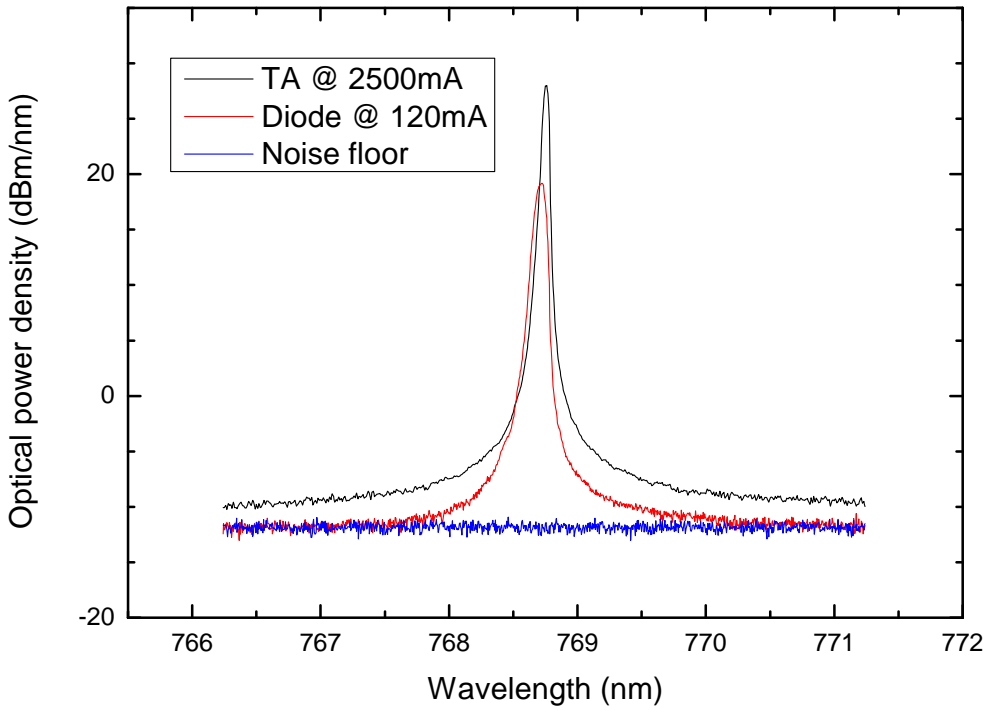


Figure 3.2: Spectra of the diode and the TA for comparison. The width of the peak in that figure is in no way an actual representation of the width since we measured it to be much narrower than the maximum resolution of the spectrum analyzer (50pm  $\iff$  25GHz at 770nm) used to acquire the above figure. In the wings of the spectrum, however, the measurement showed here is correct.

### 3.3.1 Estimating the needed attenuation

To characterize the influence of the spectrum on the atoms we first used the saturation parameter of a monochromatic light field

$$s(\delta, I) = \frac{I/I_{\text{sat}}}{1 + \left(\frac{\delta}{\Gamma/2}\right)^2} = \frac{s_0}{1 + \left(\frac{\delta}{\Gamma/2}\right)^2}$$

which describe how much or how often the two-level atoms are being driven to the excited state ; let us recall to the reader that atoms can spend at most half of the time in the excited state and this happens when  $s \gg 1$ . In our case, the optical power density is low enough for us to assume  $s_{0,\text{resonant}} \ll 1$ ; for the light of the main peak, the detuning to the D1 and D2 lines is big enough (about 0,5THz and 1Thz respectively) and the saturation parameter is low enough (about  $1000\text{mW}/(0,5\text{cm})^2/I_{\text{sat}}$ ) for us to assume  $\frac{\delta^2}{(\Gamma/2)^2} \gg s_{0,\text{peak}} \gg 1$ .

One can transform  $s$  into a saturation parameter density  $\tilde{s}(\lambda)$  by replacing the total intensity  $I$  by the spectral intensity  $\tilde{I}(\lambda) = \frac{dI}{d\lambda}$ . This allows us to integrate  $\tilde{s}$  and it gives a proper way to take a continuous intensity density  $\tilde{I}(\lambda)$  into account.

The scattering rate

$$\gamma_{sc}(\delta, I) = \frac{\Gamma \frac{s_0}{2}}{1 + s_0 + \left(\frac{\delta}{\Gamma/2}\right)^2}$$

being non-linear in  $I$ , one cannot turn it into a integrable density as easily. We could integrate the discrete data by summing each contribution  $\gamma_{sc}(\delta(\lambda), \tilde{I}(\delta, \lambda) \cdot \Delta\lambda)$  though.

A second, simpler approach consists in calculating the following ratio:

$$\rho = \frac{2\gamma_{sc}(0, I_{wing,D1}) + \gamma_{sc}(0, I_{wing,D2})}{2\gamma_{sc}(\delta_{D1}, I_{peak}) + \gamma_{sc}(\delta_{D2}, I_{peak})} \quad (3.1)$$

of the scattering rate of the resonant light in the wings to that of the main peak for both transitions. The weight 2 to 1 comes from the different transition strength already mentioned in Sec. 2.4.1. Considering a uniform intensity over an area  $A$ , the approximations for this second approach are the following:

- the power density in the wings is constant over the transition lines. The spectral width  $\Gamma$  of both transitions being approximately 6MHz, which correspond to  $\sim 12\text{fm}$  at the wavelength of the D1 and D2 lines, this assumption is justified by Fig. 3.2 which shows the spectral power density of the TA is varying slowly enough about 2nm off the peak for us to consider that the spectrum be constant over those 12fm.

$$I_{wing,D1/2} \times A = [\text{power density at } \lambda_{D1/2}] \times 12\text{fm}$$

- the peak is just a Dirac delta with a power

$$I_{peak} \times A = [\text{power density of the peak}] \times \Delta\lambda$$

equal to the maximum power density measured namely 28dBm/nm (see Fig. 3.2) taken over the resolution bandwidth  $\Delta\lambda$ .

Calculating this ratio of scattering rates gives  $\rho \approx 2700$ .

### 3.3.2 Results using a spectral intensity

Fig. 3.3 shows us the saturation parameter density  $\tilde{s}$  as a function of  $\lambda$ . The peaks related to the D1 and D2 transitions seem much more important than the one related to the intensity peak of the laser. Nonetheless we have to estimate the sum  $\int \tilde{s}(\lambda)d\lambda$  in order

to know precisely what the relative weight of the main peak of the TA to the resonant light in the wings of the TA spectrum is. The peaks could be so narrow that the main contribution to the sum comes from the broad wings of the transition peaks, even if the  $\tilde{s}(\lambda)$  has a lower value there than on the peaks.

In order to have a more precise description of the light on resonance, we fitted a function in the wings of the peak and computed the saturation parameter density with a step 1000 times smaller in the 15pm centered on the resonance – which means we added  $15\text{pm}/5\text{pm} \times 1000 = 3000$  points – than in the rest of the curve.

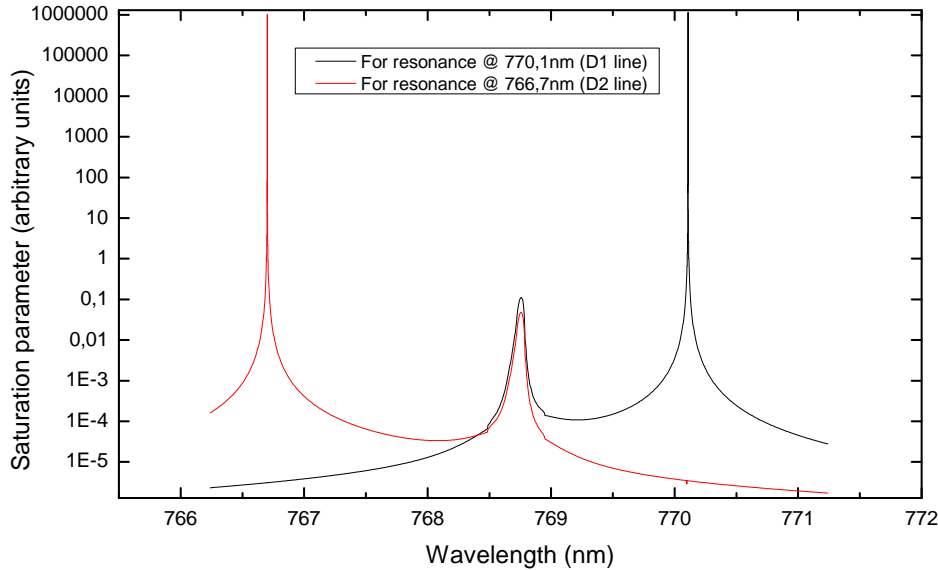


Figure 3.3: Saturation parameter density  $\tilde{s}(\delta, I; \lambda)$  vs. wavelength: the peak in the middle is related to the main intensity peak of the TA spectrum and the taller ones on its side come from the D1 and D2 lines.

Fig. 3.4 shows the integrated  $\tilde{s}(\lambda)$  and confirms the fact that the two peaks corresponding to the transition lines dominate the saturation parameter density. The importance of the transitions relative to the main intensity peak of the laser is given by the ratio of  $H_D$  to  $H_P$  (see Fig. 3.4) which are the proportions in the integral coming from the transition line ( $H_D$ ) and the main intensity peak ( $H_P$ ). For the D2 line – used for the measurement of Sec. 3.3.4 – it yields a ratio of about 6800. The contribution from the D1 line is about 3500. Taking into account both transition lines consists in summing both contribution. It is rather surprising that this last result agrees quite badly with the calculation of eq. (3.1): in any case, this method with the intensity density should be more accurate and it might mean that taking the full intensity density does matter.

Our conclusion is that we need to attenuate the resonant light by about  $10^4$  at least

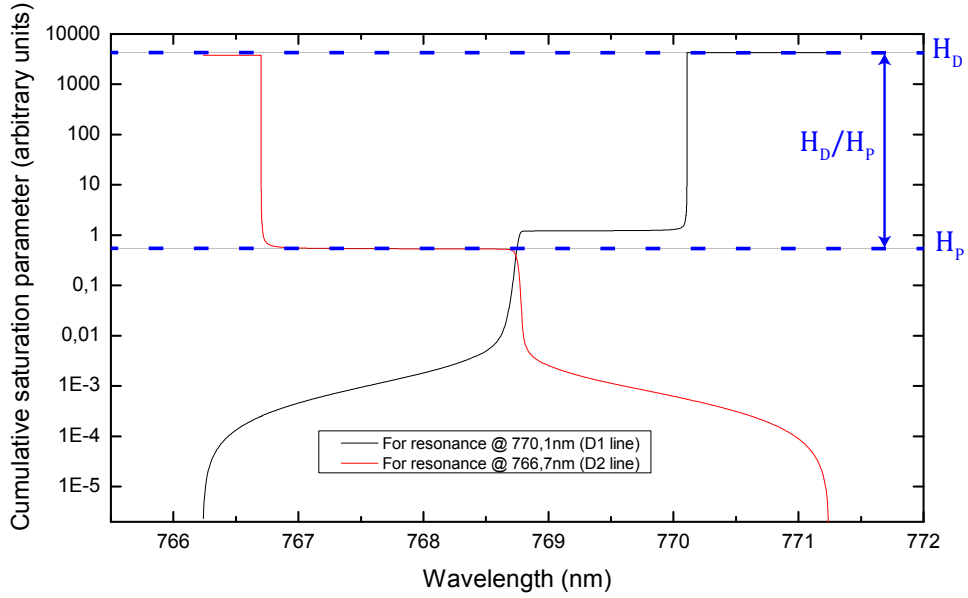


Figure 3.4: Integrated saturation parameter for both D1 and D2 potassium lines. In order to allow us an easy graphical reading of the importance of the peaks, the summing has been done by ascending  $\lambda$  (left to right) for one curve and the other way around for the second one. The factor  $H_D/H_P$  is the attenuation we have to reach in order to bring the scattering of the D2 line to the same level as the scattering from the main intensity peak of the TA light.

and  $10^5$  if the goal is to make the scattering rate due to the D1 and D2 transitions not only smaller but negligible.

### 3.3.3 Theoretical description of light absorption in the atomic vapour

Here we give a model of how the atoms in the cell are interacting with the light and filtering it. First, we would like to use that model in order to know what temperature and/or cell length we need in order to reach the right absorption of  $10^4$ , or  $10^5$  to be on the safe side. We would also like to compare the model to some data we measured in order to see if we can explain what is happening in the cell. It will be used as one additional indication of the fact that we are not able to reach enough resolution to measure clearly the attenuation factor even with three different measurements techniques.

### Exact equation of absorption by a Doppler-broadened linewidth

Let us consider a straight cell with a section of area  $A$  containing an atomic vapor and a monochromatic laser of wavelength  $\lambda_L$  with a uniform spatial intensity distribution propagating in it along the  $z$  axis. The atoms in the cell are at temperature  $T$  and feature an atomic transition modeled by a two-level system at the frequency  $\nu_0$ . The physics of absorption in this resonant medium is the following: photons of the very well-defined spatial laser mode are absorbed which bring the atoms to the excited state; the spontaneously emitted photons coming from the decay back to the ground state are scattered in random modes; this process leads to a depletion of the laser mode which means the beam is weakening as it propagates through the cell. As a result the intensity  $I$  is a decreasing function of  $z$ .

First we underline the fact that the atoms are moving in the vapor, experiencing a Doppler shift that leads to the broadening of the spectrum. We call  $n$  the actual density. The proportion of atoms having their speed in  $[v; v + dv]$  and therefore a detuning  $\delta(v) = \nu_0 - (\nu_L - v/\lambda_L)$  is proportional to the Boltzmann factor  $\exp\left(\frac{1}{k_B T} mv^2\right)$  and more precisely equal to

$$\frac{1}{\sqrt{2\pi}U} \exp\left(\frac{v^2}{2U^2}\right) dv \text{ with } U = \sqrt{\frac{k_B T}{m}}.$$

Let us now count the energy in and out a slice of the vapor exposed to laser light between  $z$  and  $z + dz$  during  $dt$ :

- The laser energy entering the slice is  $\mathcal{E}_{in} = I(z) \cdot A \cdot dt$ .
- The laser energy coming out of the slice is  $\mathcal{E}_{out} = I(z + dz) \cdot A \cdot dt$ .
- The energy scattered in random spatial modes is:

$$\mathcal{E}_{sc} = \underbrace{\int_{v=-\infty}^{+\infty} nAdz}_{\substack{\text{sum over all} \\ \text{possible speeds}}} \cdot \underbrace{\frac{1}{\sqrt{2\pi}U} \exp\left(\frac{v^2}{2U^2}\right) dv}_{\substack{\text{total number of} \\ \text{atoms in the slice} \\ \text{proportion of atoms} \\ \text{at a given speed}}} \cdot \underbrace{h\nu_0}_{\substack{\text{average energy of} \\ \text{one scattered photon}}} \cdot \underbrace{\gamma_{sc}(\delta(v), I)dt}_{\substack{\text{number of scattered} \\ \text{photons per atom in} \\ \text{dt} \\ \text{for a given speed}}}$$

Conservation of energy is of course  $\mathcal{E}_{in} = \mathcal{E}_{out} + \mathcal{E}_{sc}$  which after the substitution  $\nu_L - v/\lambda_L = \nu$  leads to differential equation of the spatially varying intensity  $I = s_0 I_{\text{sat}}$ :

$$\frac{ds_0}{dz} = -G \cdot \frac{s_0}{1 + s_0} \int_{-\infty}^{+\infty} \frac{e^{-\frac{(\nu-\nu_L)^2}{2(U/\lambda_L)^2}}}{1 + \left(\frac{\nu-\nu_0}{\Gamma\sqrt{1+s_0}/2}\right)^2} d\nu \text{ with } G = \frac{n h \nu_0 \Gamma \lambda_L}{2 \sqrt{2\pi} U I_{\text{sat}}}. \quad (3.2)$$

The integral appearing in eq. (3.2) is a convolution of a Gaussian and a Lorentzian profile: that convolution is called a *Voigt profile* (see on Fig. 3.5 for compared plots). More specifically, if  $x \mapsto G(x; \sigma)$  is the centered normalized Gauss distribution of variance  $\sigma^2$

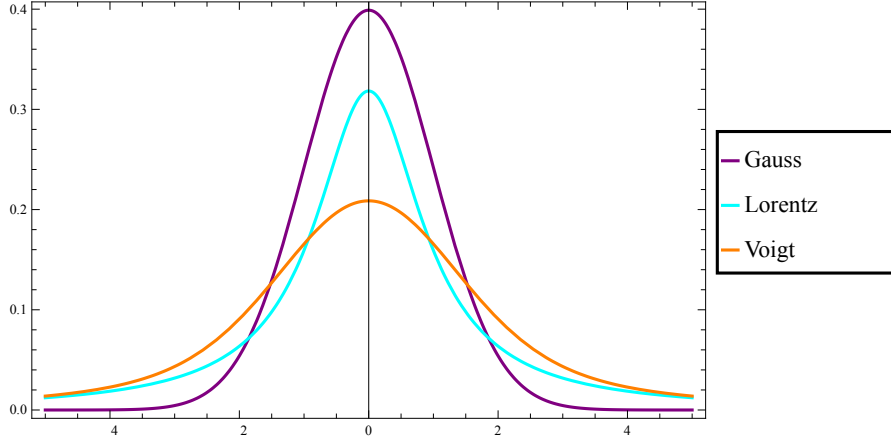


Figure 3.5: Plot of the normalized Voigt, Gauss and Lorentz profiles.

and  $x \mapsto L(x, \gamma)$  is the centered normalized Lorentz distribution of halfwidth at half maximum  $\gamma$ , then the Voigt distribution  $\mathcal{V}(y; \sigma; \gamma) = \int_{-\infty}^{+\infty} G(t; \sigma) L(y - t; \gamma) dt$ . Consequently the integral in eq. (3.2) is proportional to  $\mathcal{V}(\nu_0 - \nu_L; \frac{U}{\lambda_L}; \frac{\Gamma}{2}\sqrt{1 + s_0})$ .

We should mention that scattering of light can be treated by making use of the light scattering cross section for an atom  $\sigma$  defined by

$$\sigma = \frac{\text{total scattered power}}{\text{incoming power per unit area}} = \frac{h\nu\gamma_{sc}}{I}.$$

This does not add anything to the treatment but can lead to easier physical interpretation.

### Simplifying the problem

In the general case the width is power broadened. We will be in that situation when we measure the attenuation as a function of the intensity with resonant light; the result of that are shown in Sec. 3.3.5. We assume the power broadened linewidth  $\Gamma\sqrt{1 + s_0}$  is small compared to the Doppler width  $U/\lambda_L$ . The Gaussian function is then constant over the width of the Lorentzian and the integral in eq. (3.2) amounts to

$$e^{-\frac{(\nu_0 - \nu_L)^2}{2(U/\lambda_L)^2}} \cdot \frac{\pi}{2} \Gamma \sqrt{1 + s_0}$$

which means eq. (3.2) boils down to

$$\frac{ds_0}{dz} = -e^{-\frac{(\nu_0 - \nu_L)^2}{2(U/\lambda_L)^2}} \frac{\pi}{2} \Gamma G \frac{s_0}{\sqrt{1 + s_0}} = -\tilde{G}(\nu_0) \frac{s_0}{\sqrt{1 + s_0}}. \quad (3.3)$$

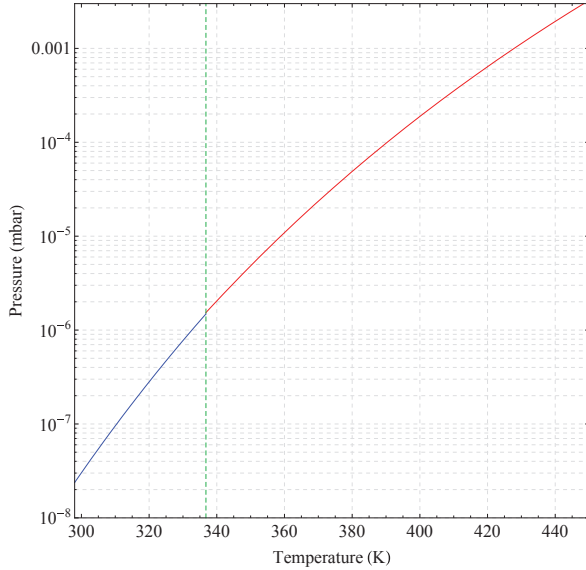


Figure 3.6: Saturation pressure of potassium *vs.* temperature. The growth is “almost exponential”, in any case faster than polynomial. The green, dashed, vertical line shows the melting point. Taken from Ref.[27]

For intensity such that  $s_0 \ll 1$ , we recover the usual Beer-Lambert law  $\frac{dI}{dz} = -\alpha I$  with an intensity-independent optical depth per unit length

$$\alpha = \frac{\pi}{2} \Gamma G e^{-\frac{(\nu_0 - \nu_L)^2}{2(U/\lambda_L)^2}}.$$

On resonance  $\alpha = \frac{\pi}{2} \Gamma G$ . From Ref.[28], the optical scattering cross section on resonance is  $\sigma_{\text{res}} = \frac{h\nu_0\Gamma/2}{I_{\text{sat}}} = 3\lambda_0^2/(2\pi)$ , hence an optical density OD on a length  $l$  of

$$\text{OD} = \frac{3}{4\sqrt{2\pi}} n \lambda_0^2 l \cdot \frac{\Gamma}{U/\lambda_0}$$

The number  $n\lambda_0^2 l$  of photons scattered on atoms of “area”  $\sim \lambda_0^2$  is just weighted by the ratio of the natural width  $\Gamma$  to the Doppler width  $U/\lambda_0$ .

The only parameter we do control in  $G$  is the density  $n$ .

We assume the vapor pressure is dilute enough in the cell so that it can be described by an ideal gas. In that case it is possible to write  $n = \frac{N}{V} = \frac{p}{k_B T}$  and use for  $p$  the saturation pressure  $p_{\text{sat}}(T)$  shown in Fig. 3.6. The factor  $G$  tells us how strong the absorption is; we have  $G \propto p/T^{3/2}$  so increasing the temperature at constant pressure lowers the absorption because it spreads the Doppler shift of the atoms further out. In our case, however,  $p$  is  $p_{\text{sat}}(T)$  which grows exponentially with  $T$  (clear on Fig. 3.6) and the overall effect is a sharp increase of the attenuation as  $T$  rises.

By using a fit for  $p_{\text{sat}}(T)$  and assuming we want to filter with a 10cm long cell – which is the standard length we have in our laboratory – we determined that 80°C would be enough to reach an attenuation factor around  $10^5$ . However, the measurement did not confirm this; in next subsection, we will see that we actually cannot know exactly how much the cell is attenuating because of a lack of resolution and signal-to-noise ratio.

We must here make a small comment about isotopes. The potassium that is used in the experiment and that we want to prevent from heating by absorption of resonant light is the fermionic species  $^{40}\text{K}$  which has a natural abundance of about 0,01% and has its D2 line at 391,016296THz according to Ref. [27]. The vapor cell contains natural potassium which contains 93% of  $^{39}\text{K}$  and 7% of  $^{41}\text{K}$ . We can thus assume that, inside the filtering vapor cell, only  $^{39}\text{K}$  with its D2 line at 391,016170 THz absorbs and “removes” resonant photons from the laser light. The isotope shift is thus of 126MHz which is smaller than the half-width at half-maximum of the Gaussian Doppler-broadened line which is worth  $\sqrt{2\ln(2)} \times U/\lambda \approx 430\text{MHz}$ . As a result, using enriched potassium would not increase significantly the attenuation.

### 3.3.4 Measurement of the absorption

We want to see how much attenuation we can reach. As we want to reach at least a factor of  $10^4$  in attenuation, we already know that it will be hard not to be limited by any kind of noise if we want to span 5 orders of magnitude in power to values under a  $\mu\text{W}$ . Every measurement mentioned in this section has been made with the light of a diode laser tuned close to the D2 line.

#### Measuring with a photodiode and an oscilloscope

The measurement in the section has been done in the following way: we periodically scan the frequency of the laser by sending a triangular signal to the piezoelectric transducer of the external cavity of the laser diode (we are not using the TA but only a few tens of mW from the diode) and the attenuated laser light coming out of the cell is sent on a photodetector; the closer to resonance the laser frequency is, the more it is absorbed and the closer to 0 the signal goes on the oscilloscope. Of course, the attenuation is measured where the detected laser light is weakest. Absorption was very small at room temperature so the cell needs to be heated.

Fig. 3.7 shows the types of signal we were detecting. The upper one is the full signal and the two other pictures are zooms from different full signal measurements. The light intensity for the lower one is weaker than for the middle one. The attenuation factor is just  $\frac{\text{total signal off resonance}}{\text{signal at max. absorption}}$  based on Fig. 3.7.

Fig. 3.8 is a plot of the absorption as a function of the temperature of the cell: we reach a maximum value.

We measure an attenuation factor threshold of about 700, which is too small for our purpose. But it looks like our measurement is limited. Indeed, we notice that, at some point, when one diminishes the intensity, thus saturating less the transition which allows

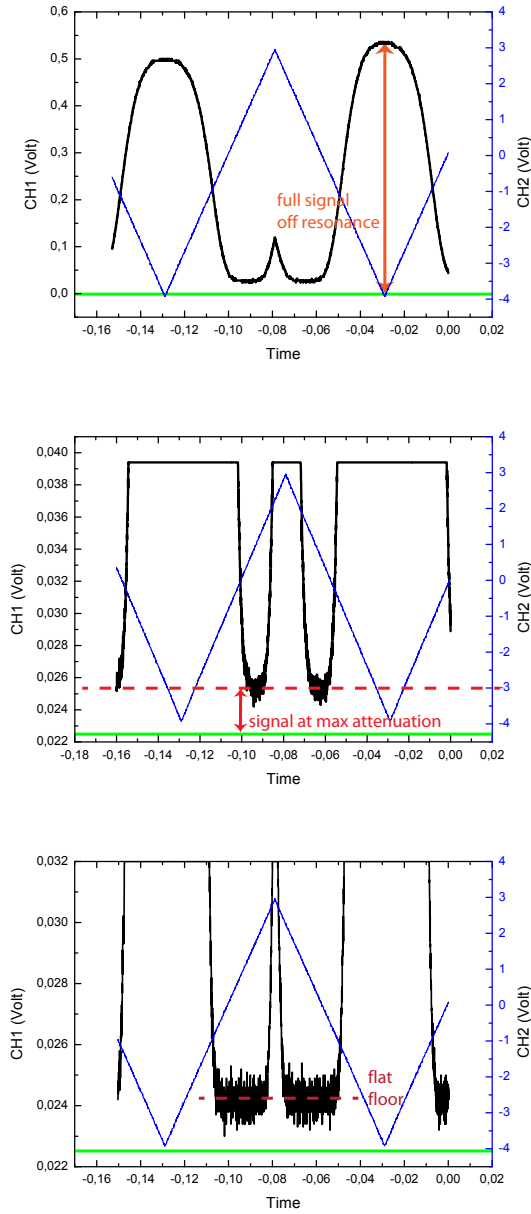


Figure 3.7: Photodiode signal of the absorption of light in the vapor cell as seen on a oscilloscope (explained in the text). The black line is the photodiode signal. The blue line is the periodic ramp send to the piezoelectric transducer that tunes the wavelength of the photodiode's light. The green line is the zero line of zero signal obtained when the light is blocked.

us in principle to achieve a higher attenuation, the point of highest attenuation does not come closer to zero but it actually widens forming the *flat plateau* we can see on the lower

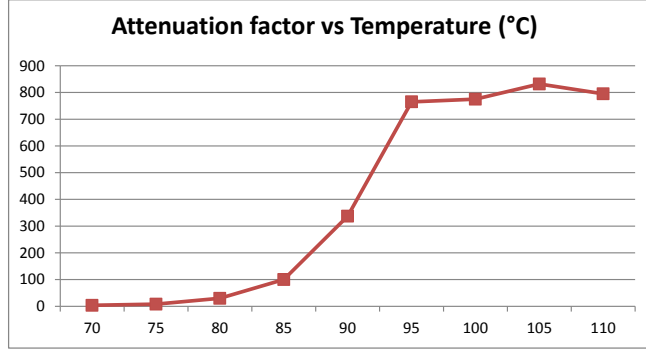


Figure 3.8: Measurement of attenuation as a function of temperature up to 120°. The measurement were made using a photodiode and an oscilloscope, like the result of Fig. 3.7.

picture of Fig. 3.7: this could mean that there is still some light coming through which is not attenuated because it is off resonance and that light could form the flat feature. As it is off resonance it would be no problem for us to have that amount of light remaining in our spectrum. We first added a fiber between the output of the cell and the photodiode to get rid of hypothetical parasite light in different spatial modes and stray light: it did not change anything. As a result, learning more on what is happening demands to measure the absorption with a good frequency selectivity.

For that purpose, we use two kinds of spectrum analyzers.

### Measuring with the SIRAH Fabry-Pérot optical spectrum analyzer (EagleEye)

The analyzer used here is a Fabry-Pérot cavity with a resonance frequency that one can tune thanks to a piezoelectric transducer which changes the cavity length. We will not go here into the details of the theory of a Fabry-Pérot interferometer/spectrum analyzer.

We measured how the transmission at the cavity resonance evolved as we were tuning the laser on and off atomic resonance by changing the voltage across the transducer *controlling the grating of the external cavity of the diode laser*, not to be confused with the transducer of the Fabry-Pérot EagleEye cavity. Fig. 3.9 is “artificial data” (generated with Mathematica) and has been added here to quickly give the reader a sense of what is being measured.

The signal displayed by the device is said to have a definition of “some MHz” in the datasheet; 10MHz correspond to a resolution of  $\lambda_L/\nu_L \times 10\text{MHz} = 20\text{fm}$  and it is 2500 times better than the 25GHz maximum resolution of the ANDO spectrum analyzer (see next subsection). A so-called “lock-loose-look” measurement technique is available via the SIRAH software provided; this can be used to increase the resolution down to 20kHz and allowed

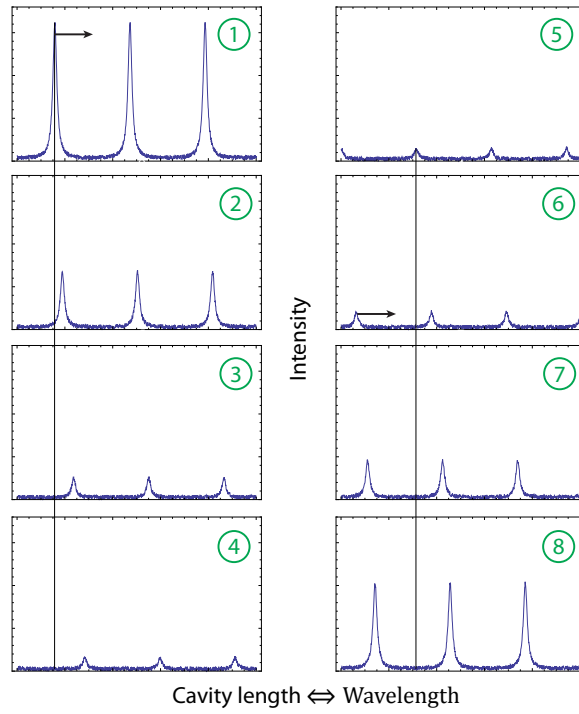


Figure 3.9: This figure is a plot of a simulation (using Mathematica) of data that can be measured with the EagleEye and it displays how the signal of the attenuation acquired by the EagleEye looked like as the piezo transducer of the diode laser cavity was tuned to slowly bring the laser frequency in and off resonance across the Doppler-broadened transition (from 1 to 8). The black line is a reference showing that the peak is moving as it gets attenuated.

us to measure a linewidth of 700kHz of the diode laser.

The attenuation measurement with the laser passing only once through the 10cm long cell with the EagleEye gave an attenuation factor of about 500 and were consistent with those obtained with the photodiode and the oscilloscope but slightly lower; in any case, they are too low in comparison to what the attenuation we want to reach.

In order to increase the attenuation one solution was then to *have the beam pass several times through the cell* to increase the length of absorption. We chose to make three passes. If the length of each pass is equal and if they do not overlap, the resulting absorption factor is then theoretically the cube of the one-pass factor.

With three passes we reached attenuation in excess of  $43\text{dB} \approx 20000$  measured thanks to the EagleEye, which is quite satisfactory. Unfortunately the built-in photodetector of the EagleEye could not provide enough amplification and it prevented us from reaching good enough signal-to-noise ratio to measure more than 43dB attenuation.

Trials have been made with another cavity and a photodiode having a better amplification but the transmission on cavity resonance was too low with this other cavity to be able to reach better signal-to-noise ratios although the signal would be plenty for other purposes, *e.g* a cavity-based Pound-Drever-Hall lock.

### Measuring with the ANDO diffraction-grating-based optical spectrum analyzer (AQ6315E)

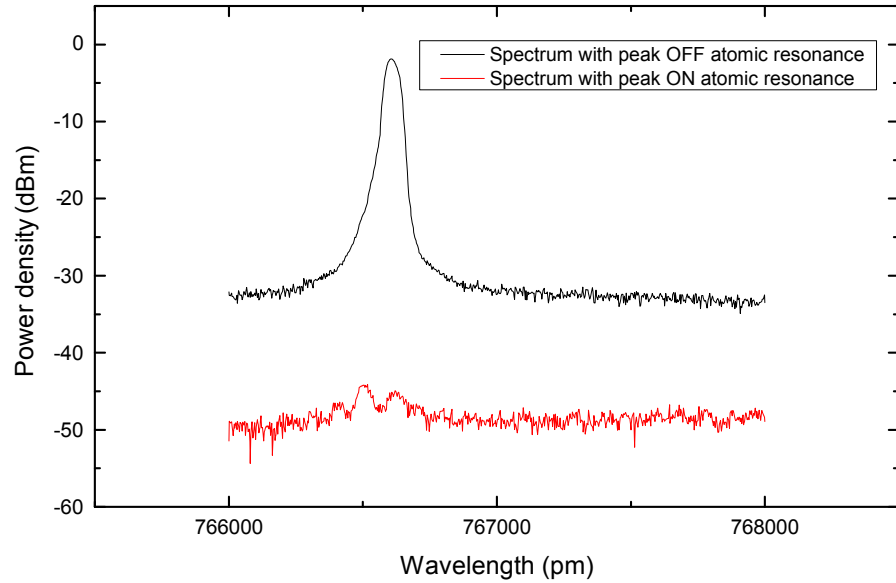


Figure 3.10: Spectrum with and without absorption through the cell measured by the diffraction-grating-based ANDO spectrum analyzer. The higher noise floor appearing in the case where the signal is not being attenuated comes from the device settings and is not real.

The principle of the measurement is the same than with the Fabry-Pérot cavity: the laser is tuned on resonance thanks to the piezo transducer of the external cavity of the laser and the intensity peak of the laser light goes down. However, due to the poor resolution, it is not possible to see the peak moving as presented in Fig. 3.9. Fig. 3.10 gives an example of the maximum absorption and no absorption cases. We observe values consistent with the 43dB of attenuation with the EagleEye spectrum analyzer.

We then carried out measurements of attenuation factor versus intensity to try and fit them to the results coming out of equation eq. (3.3).

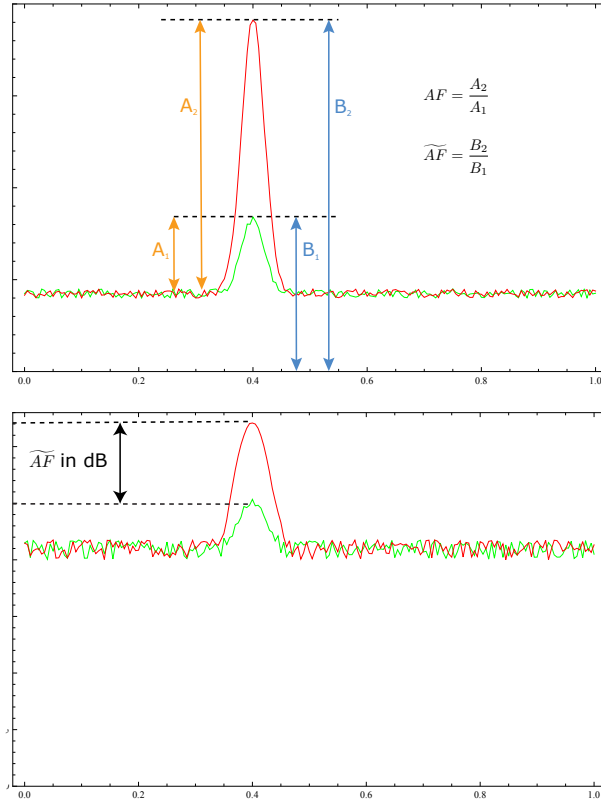


Figure 3.11: Visual explanation of the difference of definition of an attenuation factor measured in linear and log scales with randomly generated data.

### 3.3.5 Analysis of the data

#### Correcting for the noise

$S_{pk}, S_{at}, S_{no}$  denote the power density of the main peak of the laser light, of the attenuated peak and of the noise floor in dBm/nm respectively.  $P_{pk}, P_{at}, P_{no}$  are the same quantities in mW/nm and we have  $P[\text{in mW}] = 10^{S/10}$ . The attenuation factor is read directly on the optical spectrum analyzer as a height difference between two peaks: it is

$$\widetilde{AF} = P_{pk}/P_{at} = 10^{\frac{S_{pk}-S_{at}}{10}}.$$

The actual full attenuation factor  $AF$  is

$$\frac{P_{pk} - P_{no}}{P_{at} - P_{no}}.$$

In the case  $P_{no} \ll P_{pk}$ , we can write

$$AF \approx \frac{P_{pk}}{P_{at} - P_{no}} = \widetilde{AF} \cdot \left(1 - \frac{P_{no}}{P_{at}}\right)^{-1}.$$

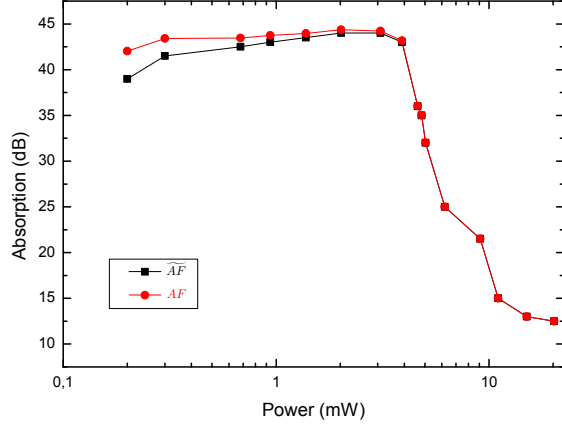


Figure 3.12: Plot of the corrected and the approximate attenuation factor as a function of the laser power entering the cell.

$\widetilde{AF}$  is close to  $AF$  only if the power of the attenuated peak is still well above the noise *i.e* if the signal is not too much attenuated which is not quite the case in our measurements. Fig. 3.11 gives a visual explanation (with randomly generated data).

Results are shown in Fig. 3.12. We see here a very flat plateau at low intensity. In this regime, the attenuation should be independent of intensity and we do expect the curve to become horizontal for small intensity as shown by the red curve on the left graph of Fig. 3.13. However, the plateau of Fig. 3.12 is much lower than what we expect from the previous model. That is why it was necessary to investigate if it could be the actual plateau or if the measurement is somehow limited.

### Fitting the data

Thanks to the model of Sec. 3.3.3, we are able to check how our analysis of the data makes sense. Eq. (3.3) can be formally integrated thanks to

$$\int \frac{\sqrt{1+t}}{t} dt = \ln \left( \frac{\sqrt{1+t}-1}{\sqrt{1+t}+1} \right) + 2\sqrt{1+t}.$$

Using this last equation, we have :

$$\left[ \ln \left( \frac{\sqrt{1+s}-1}{\sqrt{1+s}+1} \right) + 2\sqrt{1+s} \right]_{s_{in}}^{s_{out}} = -\tilde{G}(\nu_0) \cdot l \quad (3.4)$$

$l$  being the length of the cell and  $s_{in,out}$  being evidently the values of  $s$  where the beam goes in and comes out of the cell.  $-\tilde{G}(\nu_0) \cdot l = \eta$  is here an unknown constant parameter. Given a certain arbitrary  $\eta$ , we can numerically solve eq. (3.4) for  $s_{out}$  using different values of  $s_{in}$  and plot the curve  $10 \cdot \log_{10}(s_{out}/s_{in})$  vs.  $s_{in}$ : this curve is the attenuation factor in

dB as a function of the power entering the cell *i.e* exactly what is shown in Fig. 3.12.

Moreover we add a scaling factor  $f$  according to the following transformation for every data point:

$$\left( \begin{array}{c} \text{measured power} \\ \text{entering the cell in mW}, \text{attenuation in dB} \end{array} \right) \longmapsto \left( f \times \begin{array}{c} \text{measured power} \\ \text{entering the cell in mW}, \text{attenuation in dB} \end{array} \right)$$

in order to account for the fact that we are using the normalized quantity  $s$  on the x-axis. Fig. 3.13 shows how data and fitting curve superimpose for two different couples  $(\eta, f)$ : on the left is a choice of parameters that tries to account for the plateau of the data in green, on the right is a fit that appears to be good. Fits have been made by eye and is more of a sanity check than a quantitative evaluation of parameters.

We see that trying to recover the plateau in the fit leads to a very poor fit whereas theory is much closer to data in the right graph. Our model learns us that absorption should be going much higher than what we measure as one goes into the  $s \ll 1$  region of intensity-independent attenuation. The standard deviation characterizing the Doppler broadening is  $U/\lambda_L \approx 365\text{MHz}$  at  $100^\circ\text{C}$  and the resolution of the ANDO optical spectrum analyzer is 50pm which is equivalent to 25GHz  $\gg 365\text{MHz}$ . We can again assume the remaining small peak which yields the flat plateau of Fig. 3.12 is some light in the 25GHz centered on the D2 line that cannot be suppressed because it is too far away from the center in units of  $U/\lambda_L$ .

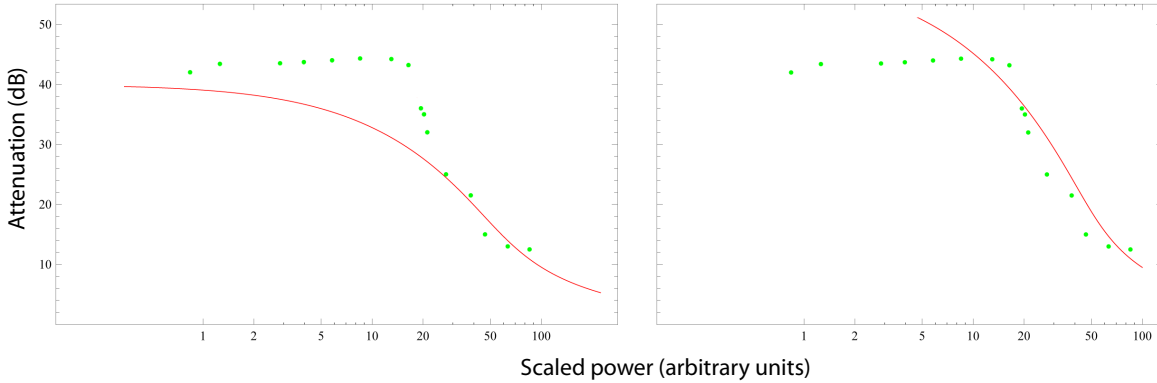


Figure 3.13: Two graphs with the data in green and the fitting curve in red for two different sets of parameter  $(\eta, f)$  applied to the same set of data. The graph on the left is a good fit determined only *by eye*. It was not possible to fit correctly the flatness of the plateau at low intensity; however it was possible to fit well the decreasing part for higher intensity and lesser attenuation. The discrepancy between the model and the data is probably due to the fact that the resonant light is attenuated more than what the plateau of the data shows but this resonant light is covered at high attenuation by off-resonant light that we cannot distinguish due to the low resolution of the optical spectrum analyzer.

### 3.3.6 Conclusion & issues concerning each method

What is probably happening is the following: the cell suppresses the resonant light quite strongly – above 20000 times as we saw it, possibly orders of magnitude higher – but at some (spectral) distance from the resonance, at which the cell does not filter out efficiently, there is still an important part of non-attenuated light that comes through the cell and is detected. This remaining light prevents us from seeing how much the main laser light peak with a width of 700kHz has gone down on the photodiode. Indeed, the measurement with the photodiode and the oscilloscope is as frequency-selective as the photodiode whose spectral range is several hundred nanometers broad and cannot make a difference between light in a frequency interval of a few Doppler width.

The Fabry-Pérot spectral analyzer obviously allows us to discriminate much better between the importance of different frequencies so does the diffraction-grating based analyzer. For the latter the signal-to-noise ratio and especially the resolution are too small to measure further and conclude in a definitive way as to what is happening to the light passing through the cell. As far as the Fabry-Pérot cavity (EagleEye) is concerned, it is the signal-to-noise ratio reached by the photodetector which limits our measurement.

For both spectral analyzers signal-to-noise ratio could be increased by using a larger beam since it would provide more power for equal saturation parameters. The optimum but realistic solution to actually measure higher attenuation if need be would be to use a cavity – ensuring a good enough resolution – reaching high transmission on resonance as well as a better photodetector than the one of the EagleEye.

## 3.4 Other options for filtering out the resonant light

The advantage of an atomic vapor filter is that it automatically filters out the right wavelengths. Unfortunately it has to be heated to reach the right attenuation factor and that poses in practice some small problems when trying to make the setup nice and compact. It is also, as we saw, hard to measure with a good enough spectral resolution that allows us to fully understand what attenuation factor we reach at the chosen wavelength.

The first alternative to the atomic vapour filter is the (*Fabry-Pérot*) *etalon*. The transmission of the etalon as a function of frequency is periodically peaked around some values which correspond to the transmitted light interfering constructively. Such filtering etalons are usually a few mm thick (unlike the EagleEye (Fabry-Pérot) cavity), and the position in wavelength of the transmission peak is usually tuned by temperature. The maximum suppression between two peaks of such an etalon is  $F^2$  where  $F$  is the finesse of the cavity. That means that  $F = 300$  would be enough to suppress by a factor of about  $10^5$  and such a finesse is quite easy to achieve for standard etalons. The only problem one could face using an etalon is that the D1 and D2 resonances are not equally far away from the main peak. That could demand using 2 different etalons in a row or need a not so straightforward fine tuning of the etalon properties.

A second well-suited alternative is the *birefringent filter* like the *Lyot filter* or the *Šolc filter*. Such filters use the different index of refraction for perpendicular polarization components of the light in a highly birefringent material to select, via a polarizer, the light in a narrow band that have the “correct” wavelength. They are usually composed of several stages assembled in a chain: the more stages are built, the narrower the filter is. Like etalons, they have a periodic transmission (as a function of the  $\lambda$ ). For details on birefringent filters, the reader can refer to Refs.[29] and [30]. It might very well be a good solution but we have not been able to investigate more so far.

The last alternative is to use *interference filters*. Such filters are made of thin dielectric layers; when the light passes through, it is reflected on the successive layers and the reflected waves interfere; that allows a wavelength to pass only under certain conditions. In particular, one could use optical edge filters for our purpose which allow wavelength above (longpass) or below (shortpass) a certain threshold value to be transmitted: either two shortpass, two longpass or one of each would be needed. Longpass (resp. shortpass) filters have a cut-on (resp. cut-off) value that can be tuned by changing the incidence of the light on the filter. The problem with edge filters is that they usually have a pass/block transition of one to several nm and we would like to separate features that are 1nm apart (the D1 line and the peak): that is why that solution might just not work. Shortpass and longpass filters sold by THORLABS let 0.01% through on the attenuated side *i.e* have an attenuation factor of  $10^4$ .



# Chapter 4

## Phase noise and Phase-Locked Loop (PLL)

In this chapter, we first explain the reasons for the phase-lock loop designed to suppress phase noise between the Raman beams, as well as the main principles of this loop and then continue by characterizing its performance.

### 4.1 Why do we need a phase-locked loop ?

The four beams of the Raman setup are shone on the atom cloud and interfere to form the lattice potential that enables us to mimic a strong magnetic field acting on charged particles. How precisely the beams interfere is set by the relative phase between the beams. Each of the four beams is described by an electric field of the form  $E_0 \hat{\epsilon} \cdot \exp(i(\omega t - \vec{k}_\alpha \cdot \vec{r} + \Phi_\alpha))$ . As long as the phase  $\Phi_\alpha$  is constant, it is of no importance in our case what particular value it takes: it only sets the absolute position of the beam in space (modulo the unit cell). If, however,  $\Phi_\alpha$  happens to be some unwanted time-dependent phase, then it would make the lattice shake with time *as a whole*. For two physical reasons we would like to avoid this troublesome lattice shaking.

We saw that one of the main attributes of the optical flux lattice scheme is that it creates a non-zero geometrical phase and this so-called Berry's phase is directly related to the artificial magnetic field: the amount of geometrical phase that is picked up by any wavefunction  $|\phi\rangle$  moving around in the lattice depends solely on its path through the potential and not on any detail of the dynamics. If the lattice were to randomly wobble, the geometrical phase associated with a well-defined spatial path will also have a random component and this directly corresponds to an random component of the artificial B-field.

Secondly, the shaking of the lattice can be a means of transferring kinetic energy to the atoms which have been previously carefully cooled down to quantum degeneracy. This happens if the shaking frequency is resonant with the transition energy between adjacent bands of the lattice band structure. In our case, the gap between the first very flat band and the second one is (following Ref.[17]) about one third of a recoil energy for potassium

$E_R = \hbar^2 k_L^2 / (2m_K) \approx 2\pi \times 8,4\text{kHz}$ . We thus want to get rid of phase noise with frequency on the order of a few  $E_R$  at least. The low frequency end of the range were we want to attenuate noise is set by the maximum duration of the experiment, which is set by the scattering rate of the 769nm light, and would be around 30ms, which corresponds to  $1/30\text{ms} \approx 33\text{Hz}$ .

Since the four beams come out of the same laser emitting light at  $\omega_L = 2\pi\nu_L = ck_L$  and are separated via three polarizing cubes, all four Raman beams are coherent up to the input of the fiber: indeed, any kind of noise of the laser is transmitted in exactly the same way to the four beams.

That main source of noise is the fiber going from the laser table – where we installed the laser for the Raman beams – to the experiment table. The laboratory environment induces vibrations of the fiber because of surrounding acoustic noise or other kinds of parasitic vibration in the range of tens of Hz to a few hundred kHz ; also, slow temperature drifts of the air surrounding the fiber can cause changes in its transmission properties. The consequence of this noise is effectively to change the index of refraction of the fiber, which causes a change in the phase of the light at the ouput. What we will actually be doing is locking the phase of the light after the fiber to its phase before the AOM.

In order to control the phase of the light via the AOM, we need to be able to control easily the frequency fed to the AOM. This is achieved by using a **Voltage Controlled Oscillator** (VCO). Appendix D shows how the AOM *imprints its phase* of the input RF wave and also *allows us to control the phase of the light*. Since the noise is introduced by the optical fiber, which has nothing to do with a RF signal, having a perfectly noiseless RF signal fed to the AOM would not help; that is why we need a feedback loop and more precisely a **Phase-Locked Loop** (PLL). The VCO, when free-running, has some phase noise mainly due to usual electronic noise on the control voltage or on the operating voltage but it will be suppressed by the PLL. In Fig. 4.1 the comparison between the noise spectrum of the light measured after the fiber and the noise of the free-running VCO output shows that the fiber noise is dominating.

## 4.2 How does our PLL work ?

### 4.2.1 Main lines of the loop

We follow the scheme that can be found in Ref.[31].

A bit of light is reflected off the straight-cut fiber core-air interface at the end of the optical fiber (the input interface is angle-cut). This back-reflected light propagates a second time inside the fiber, then inside the AOM and so carries twice the phase noise  $\delta\phi$  with a shift  $2\omega_{AOM}$ . We pick off some of that back-propagating light on a glass plate used to also pick off some noise-free forward-propagating light (called main beam or carrier in the text) and beat the noisy and noise-free light against each other on a photodiode. The resulting beat note yields an RF signal at  $2\omega_{AOM}$  carrying the phase noise  $2\delta\phi$ . This RF signal is

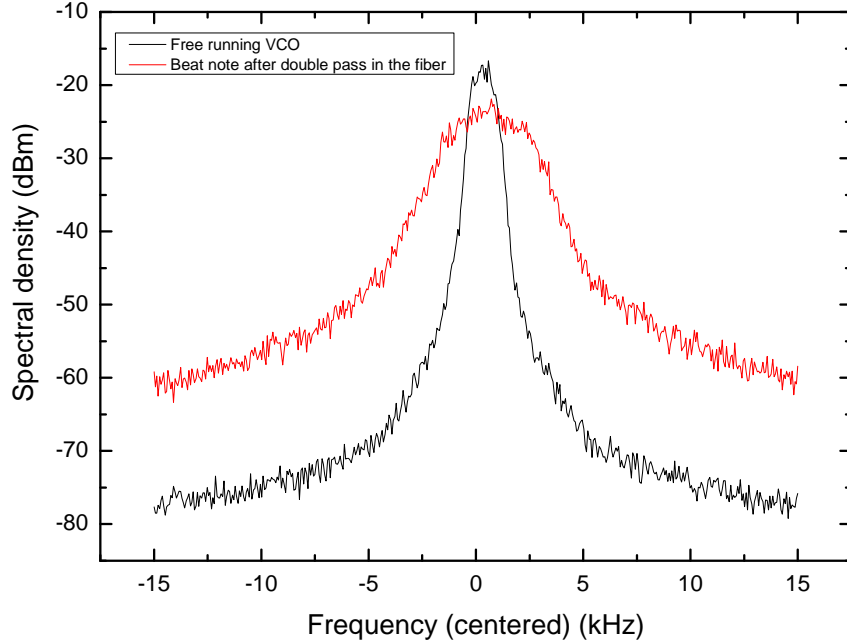


Figure 4.1: Power spectrum of the phase noise of a free running VCO and of the noise generated by the optical fiber as measured by an RF spectrum analyzer. It is clear on that picture that the noise coming from the fiber has a much wider spectrum. As far the amplitude is concerned, the two curves here have been measured with different circuits, therefore their absolute value of the power in dBm cannot be directly compared.

again beat against a noise-free RF reference signal at  $2\omega_{AOM}$  in a balanced mixer which outputs a *DC error signal* proportional to  $\cos(2\delta\phi(t))$ . The error signal is fed back to the AOM that controls the frequency of the light via a P or PI controller, which is the *loop filter*. The feedback mechanism – if properly adjusted – drives the error to 0.

Let us mention one crucial point common to each PLL, namely that they all have a “built-in” integrator. The tuning voltage of the VCO is the control parameter and it is locally proportional to its output frequency. The measured output of the VCO that one tries to stabilize is a phase, which is the integral of the frequency: that is why any PLL necessarily contains an integrator. The basic control theory about feedback loops needed to grasp the mechanism is described in Appendix E but we add only one thing here on that topic: the loop must have a *high open loop gain* for the noise to be efficiently suppressed, and that this gain is tunable via the loop filter. The essential parts of the PLL are drawn in Fig. 4.2.

The loop and all its steps are described in more detail in Appendix F.

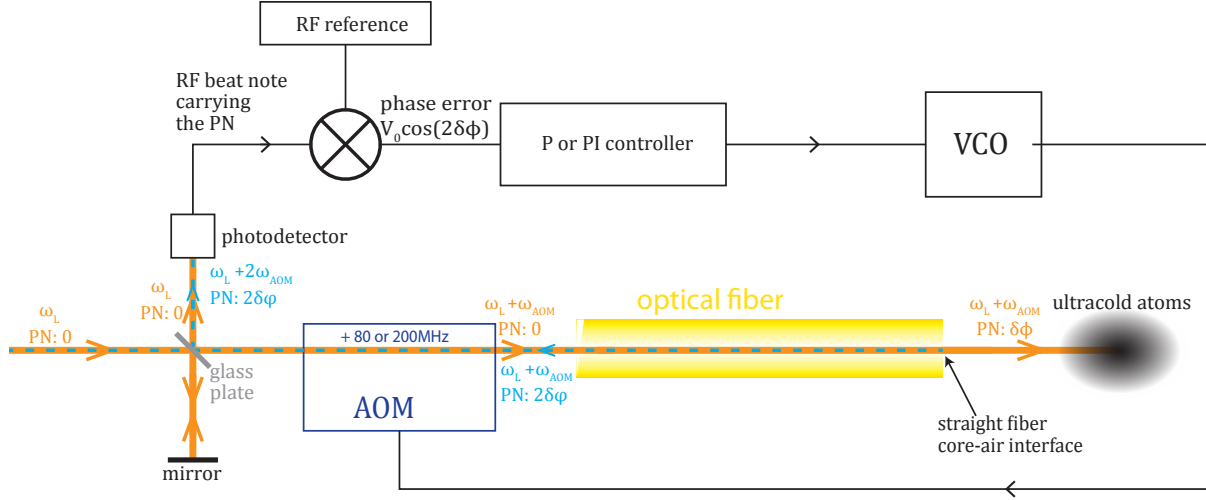


Figure 4.2: Principle of operation of the PLL: here are only drawn the crucial parts and quantities needed to understand what is happening. “PN” means “phase noise”. The two lines next to the arrowheads give first the angular frequency of the light at that point in the loop and then the phase noise that it carries. Of course, the phase noise is there anymore when the feedback mechanism is operating.

Dashed blue: back-propagating light.

Orange solid: forward-propagating light.

### 4.2.2 Inherent limitations

Let us mention here crucial characteristics in our loop which limit its performance.

First of all, our technique relies on the interference of the light before the AOM and the fiber and after a double pass in the fiber. The interference have to actually take place on the photodiode otherwise there is no error signal generated. The condition for the light to interfere is that the difference in optical path between the two interfering beams is less than the coherence length. As we already said in Sec. 3.2, we measured a laser diode linewidth of 700kHz. Assuming the TA does not significantly broaden that main peak, we have a coherence length of  $c/700\text{kHz} \approx 430\text{m}$  which is much longer than the  $\sim 11\text{m}$  (counting  $2 \times (5\text{m of fiber and a bit more in open air})$ ) of path difference between the two beams: that condition is met in our setup.

We assumed that the phase noise  $\delta\phi(t)$  in the fiber is the same on the first travel as on the way back after reflection off the straight-cut tip of the fiber. That says implicitly that the time-dependent random variable  $\delta\phi(t)$  must not change too much as the light propagates through the fiber during the time  $10\text{m}/c$  and that corresponds to  $\delta\phi$  having spectral components *much smaller than*  $c/10\text{m} \approx 30\text{MHz}$ .

*We have to avoid accumulating a phase shift of  $\pm 180^\circ$  along the loop (see Appendix E*

for an explanation). With  $\Delta_{fib} = 10\text{m}$  of optical fiber as well as, say,  $\Delta_{cab} = 5\text{m}$  of cable, a phase shift of  $\pi$  rad corresponds, thanks to the equality  $k \cdot (\Delta_{fib} + \Delta_{cab}) = \pi$ ,  $k = 2\pi f/c$ , to  $f = 10\text{ MHz}$  which is of course the same ballpark than the limitation due to condition we just brought up.

Lastly, the most important problem comes from the AOM; indeed, this device diffracts the light by means of a sound wave in a crystal. When the transducer moves and creates the wave, the latter has to propagate inside the crystal *while carrying the signal* and reach the spatial position of the beam during the so-called *dead time* to be able to transmit the signal to the laser light. The dead time is represented on the figure of Appendix F. That dead time is also the origin of an important phase lag. The problem lies in the fact that a sound wave is very slow for electronics standard. The data sheet mentions a speed of sound of  $C_s = 4.2\text{mm}/\mu\text{s} \approx \frac{c}{71400}$ .

We measured the AOM dead time with the following simple method: a square pulse is used to drive the AOM and the light diffracted by the AOM is detected by a photodiode. An oscilloscope is used to display both the RF square pulse and the photodiode output: the dead time is – neglecting the propagation in cables if they are short enough – the time difference between the instant the two signals are going up. It was not possible to reach a high diffraction efficiency with a dead time under 300ns (corresponding to a “dead length” of  $C_s \times 300\text{ns} = 1.26\text{mm}$ ). 300ns corresponds to a  $\pi$  phase lag at  $1/(2 \times 300\text{ns}) \approx 1.67\text{MHz}$ . As a result, we cannot have an amplitude gain around 1 close to 1.67MHz if we want the loop not to oscillate; if it is much lower, the loop is not efficient anymore. It can be well above unity, but starting from 1.67MHz, getting higher in frequency means having more fluctuation due to phase lags  $> \pi$  in the fed back signal and the feedback process loses gradually its efficiency anyway. So the dead time is clearly the bandwidth limiting factor.

Coming from a similar cause, the *rise time* has to be taken into account: that rise time is due to the fact that after the sound wave has reach the beam, its efficiency at diffracting the beam is full only once it has propagated through the entire beam. By definition, that delay depend on the beam size and the datasheet mentions a linear dependence of  $\text{RiseTime} = 0.15\text{ns}/\mu\text{m} \times \text{BeamSize} + 5\text{ns}$  (for the 200MHz AOM). The beam size of the TA mode is very hard to determine and it has some very peculiar shape – with a certain degree of symmetry, though – but it was definitely under 1mm which corresponds to 155ns of dead time. That means that the dead time is really the limiting factor. Also the rise time is supposed to be independent of how the AOM is aligned as long as the beam size (set by the focal length of the lens right before it) is maintained constant.

### 4.2.3 The lock-box – Use of a double integrator

A lock-box containing the loop filter has been designed and is showed in details in Appendix A. The circuit of Fig. 4.3 is basically the actual loop filter which has been implemented in the setup. This kind of loop filter is called a *PI controller* whenever the switch is in the “PI” position and a P controller otherwise.

In the loop, the controller is located between the phase detector (*i.e* the mixer) which outputs a voltage  $v_d$  and the VCO, whose input is the tuning voltage  $v_t$ . Here we considere

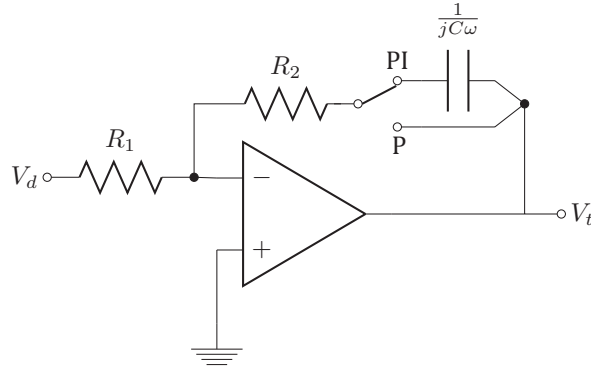


Figure 4.3: The above circuit is a representation of the (active) loop filter used for the PLL studied here. It can be switched between P gain and PI gain and was kept fairly simple.

the corresponding quantities in the Fourier domain (see Appendix F for more explanation) which are  $V_d$  and  $V_t$ .

The complex transfer function  $F_{PI}(\omega) = V_t/V_d$  is straightforward to calculate. One can use the formula for a usual inverting amplifier and use for the capacitor its complex impedance  $\frac{1}{j\omega C}$  as a resistance in series with  $R_2$ . We add a factor  $-1$  because the offset stage after the loop filter is also inverting. It yields:

$$F_{PI}(\omega) = \beta \frac{1 + j\omega\tau}{j\omega\tau} \text{ with } \tau = R_2 C, \beta = \frac{R_2}{R_1}.$$

Evidently,  $F(\omega) \rightarrow \beta$  as  $\omega\tau \rightarrow \infty$  and  $F_{PI}(\omega) \sim \frac{\beta}{j\omega\tau}$  as  $\omega\tau \rightarrow 0$ . This controller has the advantage of the infinite gain for DC input coming from the integrator part as well as a non-vanishing frequency-independent gain at low enough frequency due to the proportional part. Fig. 4.4 shows the transfer function of the PI controller. Both  $|F_{PI}|$  and  $\text{Arg}(F_{PI})$  undergo a transition around  $1/\tau$  from the integrator regime to the proportional one.

Slow drifts of some control voltage or of the VCO tuning sensitivity, which can be explained by temperature drifts, ageing of electronics or multitude of other causes amount to forcing a small constant offset on the tuning voltage of the VCO. That small offset can also come from a mere frequency mismatch in the adjustment of the VCO frequency to the reference frequency when the loop is adjusted. We have observed such drifts and we estimated them to about a tenth of radian over 3 to 5 minutes. That would be no problem in the cold atom experiment; indeed at that speed, it means that the lattice would just slowly translate over time as experimental sequences are repeated, which should not have any influence on the physical results. But we comment here shortly on how to get rid of such drifts. They correspond to forcing an offset on  $V_t$ .  $V_t$  becomes  $V_t + \eta$ . If the gain  $F_{PI}(\omega)$  is just a constant proportional gain  $F_0$ , and if the phase detector output  $V_d = K_D \Phi_e$ , where  $\Phi_e$  is the phase error in the frequency domain (Appendix E provides more detail about definitions) then we have  $V_t = F_0 K_D \Phi_e$  and that relation means clearly that it forces also

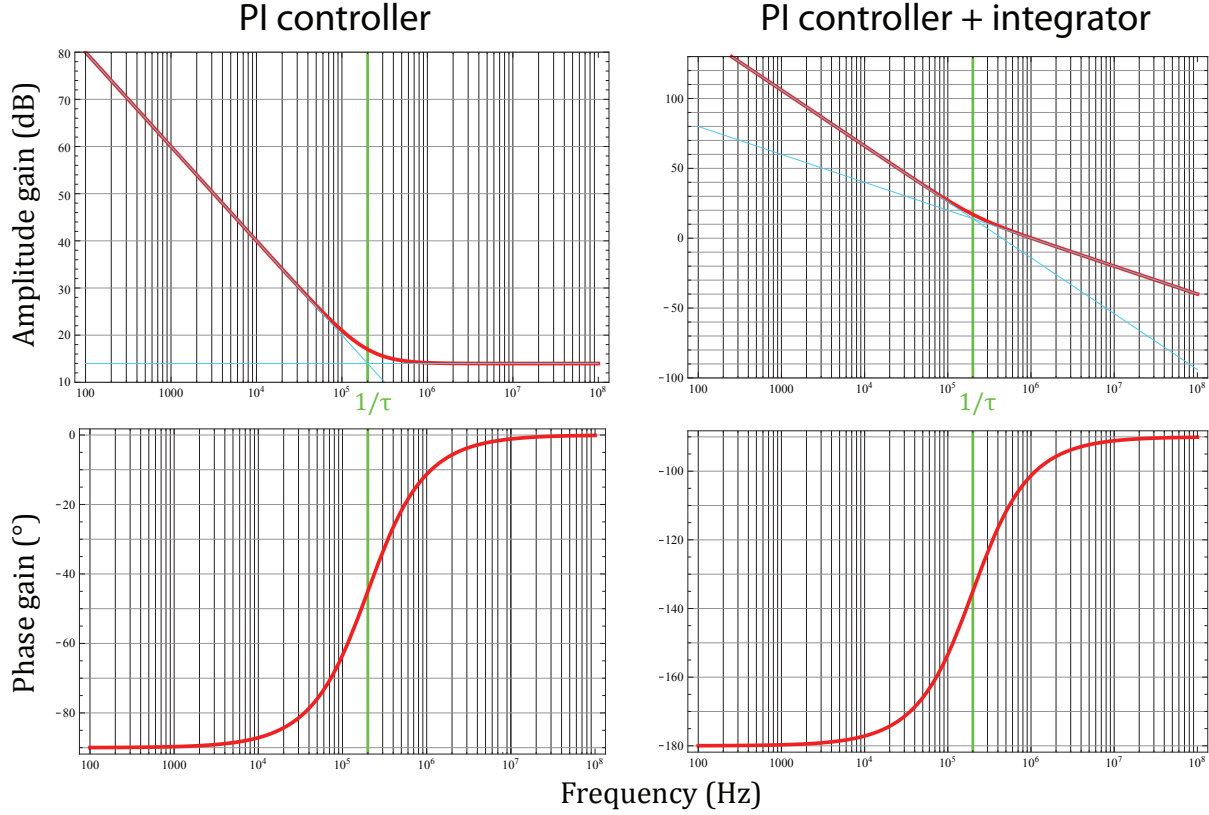


Figure 4.4: This figure shows what the theory predicts for the amplitude and phase gain – *i.e.* the Bode diagram – of a PI controller (on the left) and of a PI controller with a second integrator in series (on the right) with a time constant  $\tau$  arbitrarily chosen at  $5\mu\text{s}$ . We can see the transition from an integral gain at low frequency to a proportional gain. *On the right, we can see what we should be measuring in our closed loop.* The light blue lines are the asymptotes, which can be used as a simplified transfer function.

an offset on  $\Phi_e$ . The intrinsic integrator of the closed loop allows the system to correct for a voltage offset, which should be a frequency error in open loop, by a phase error. Using an additional integral gain, we know that  $F_{PI}(\omega)$  is infinite for  $\omega = 0$  *i.e.* for a DC voltage and to maintain a finite  $V_t$ ,  $\Phi_e$  has to be zero in the steady state.

## 4.3 Performance, frequency response

Phase-lock has been achieved with the loop described in Sec. 4.2.1. Let us have a closer look at the performance of the lock.

### 4.3.1 Measurements with a spectrum analyzer

#### The spectrum analyzer

We give here a short explanation of what the analyzer does in order to understand that we are actually seeing the right thing. The principle of operation of a spectrum analyzer is simple: it displays the power of the electrical signal that is fed to it in a certain frequency interval, that power being proportional to the squared voltage amplitude of the electrical signal. That interval is called the *resolution bandwidth* and it describes basically the smallest frequency distance between two peaks for the analyzer to be able to make a difference between that pair of peaks and a single peak (assuming the power of the peak pair and the single peak is the same).

A noisy oscillating signal  $V_n$  can be cast in the form:

$$V_n(t) = V_0(1 + \delta A(t))\cos(\Omega_0 t + \delta\phi(t)), \delta A \ll 1, \dot{\delta\phi} \ll \Omega_0$$

The function cos could be replaced by any other periodic function with harmonics *e.g* a triangular waveform. If  $\delta\phi = 0$ , the signal has pure amplitude noise  $\delta A$  and it is therefore obvious that the spectrum analyzer displays that amplitude noise by definition of its measurement process.

If  $\delta A = 0$ , the signal has pure phase noise  $\delta\phi$ . The easiest case here is to consider the telling example of a phase perturbation with a single frequency components  $\delta\phi(t) = \beta\sin(\Gamma t)$  where  $\beta \ll 1$ . The signal is said to be “phase modulated” in that case.

Using first  $\cos(\Psi) = (e^{i\Psi} + e^{-i\Psi})/2$ , expanding then  $e^x \approx 1 + x$  for  $|x| \ll 1$ , and finally applying  $\sin(a) \cdot \sin(b) = (\cos(a - b) - \cos(a + b))/2$ , one easily derives the following result – probably already known to the reader – :

$$\cos(\Omega_0 t + \beta\sin(\Gamma t)) \approx \cos(\Omega_0 t) + \beta\cos([\Omega_0 + \Gamma]t) - \beta\cos([\Omega_0 - \Gamma]t).$$

That means that a monochromatic phase noise with frequency  $\Gamma$  creates so-called *sidebands* around the main signal – called *carrier* – at  $\Omega_0$  placed on either side of the carrier at a distance  $\Gamma$  and with a  $\pi$  phase difference. The amplitude ratio  $A_{\text{sidebands}}/A_{\text{carrier}}$  is just the phase modulation amplitude  $\beta$ . Phase noise with a broad spectrum around a center frequency  $\Omega_0$  can be interpreted as a Fourier superposition of phase modulation with many monochromatic components which each produce a sideband with a certain amplitude shifted by a small amount away from  $\Omega_0$ . By measuring the power spectrum which directly translates into amplitude spectrum, one has an access to the phase noise.

One important point to be added: when the spectrum analyzer is measuring a signal with both non-vanishing  $\delta\phi$  and  $\delta A$ , one cannot make a difference between the effect of phase and amplitude noise *a priori*.

#### The power spectrum of the phase-locked signal

The focusing of the interference on the photodiode is optimized using the height of the beat note peak on the spectrum analyzer: using the two mirrors that controls the direction

of the strong carrier and the weak back-reflected beam independently, one carefully walks the mirror until the height is maximum. We observed that a part of the beat note comes from the interference of the carrier with a small part of the *light that is back-reflected on the output face of the straight-cut AOM crystal*. Indeed, this back-reflected beam is also shifted by  $2\omega_{AOM}$ , and so produces interference at the same frequency that the beat note we are interested in, but does not carry the phase noise of the optical fiber. One obvious solution to limit this problem would be to use AOMs with an angle-cut crystal. The strength of this parasitic component varies within about 10dB from alignment to alignment but it is always at least 20dB below the beat note we use.

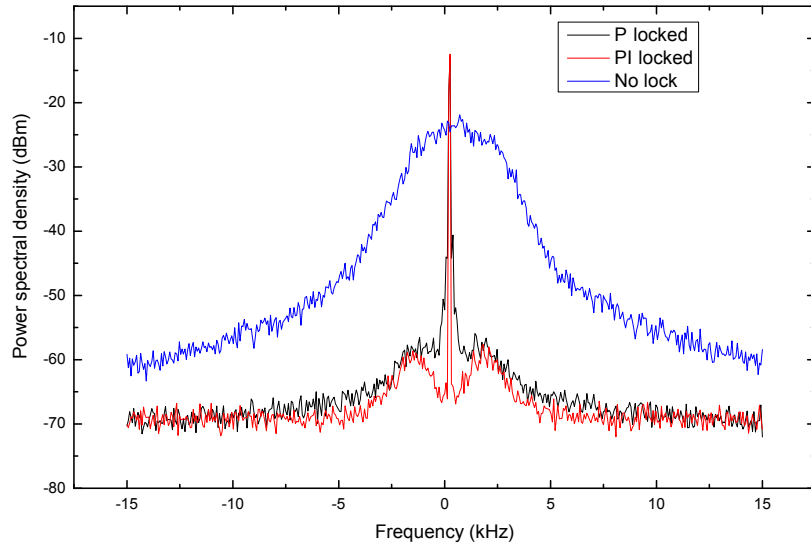


Figure 4.5: Measurement of the phase noise by a spectrum analyzer, with and without lock. The efficiency of the phase-lock is dramatic and shows that the spectrum, wide of about 10kHz is reduced to a peak with a width under 10Hz. One can clearly see the difference between the P-locking and the PI-locking at low frequency. The absolute center frequency is  $2 \times f_{AOM} = 400\text{MHz}$

Fig. 4.5 shows a comparison of measurements from a spectrum analyzer with and without lock. It is clear that the phase noise has been suppressed by a great deal and the phase-locked spectrum is much narrower. The noise is suppressed by 30 to 40dB and the signal can be considered a “Dirac delta peak” to the extent that the width is below the lower bound of the resolution bandwidth of the spectrum analyzer used here *i.e* 10Hz. We can also see that the additional integrator adds some gain at low frequencies as expected.

When the gain is too high and there is positive feedback at some frequency, one can see sharp peaks on both side of the main peak appear, showing that the noise at that frequency is being really amplified in the close loop which is of course a bad setting.

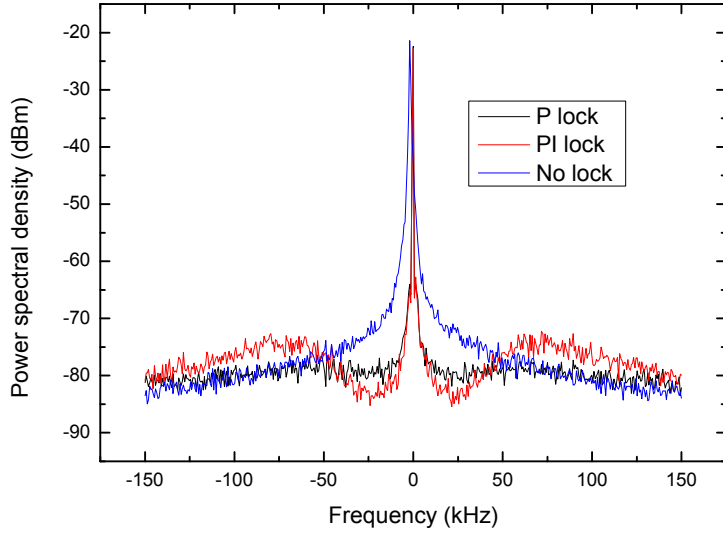


Figure 4.6: Measurement of the phase noise by a spectrum analyzer on a broader scale. The PI-locked spectrum has been tuned to a quite high gain and it shows the phenomenon of noise enhancing in the wings.

In order to make sure we are really suppressing the noise introduced by the fiber, we had two phase-locked beams interfere and beat against each other after the fiber. The reader can find in Sec. F.1 a proof of how beating beams against each other allows one to extract the phase difference between the beams. It is better not to measure the spectrum in the presence of higher electronic noise at very low frequency – so-called *flicker* noise or  $1/f$  or *pink* noise for instance – and therefore we locked one beam at  $\nu_L + f_{AOM}$  and another one at  $\nu_L + f_{AOM} - 1\text{MHz}$  which produced a beat note at 1Mhz. The result of that measurement is shown in Fig. 4.7. Indeed the beat note is very narrow when both beams are phase-locked and broad otherwise. It proves that the phase lock nicely does the job it has been build for.

The limitation of the phase-lock performance is when the noise is attenuated down to the noise floor of the signal. If that noise floor is set by a light-related noise, which can be here mainly the photon shot noise (which comes from the fact that photons arrive at a random rate on the detector) or the laser intensity noise (which comes from the diode laser being not ideal, for instance because the pumping current is not stable enough) of the strong carrier and the spectrum reaches that noise floor when phase-locked, then it is impossible to get to a higher attenuation by changing the PLL because such noise will always be included in the signal that generates the error voltage. It would be a problematic situation if the light-related noise were lower than any kind of electronic noise embedded in the beat note signal: that would prevent us from seeing how much the phase noise is actually attenuated. Determining whether or not the main noise is electronic or photon

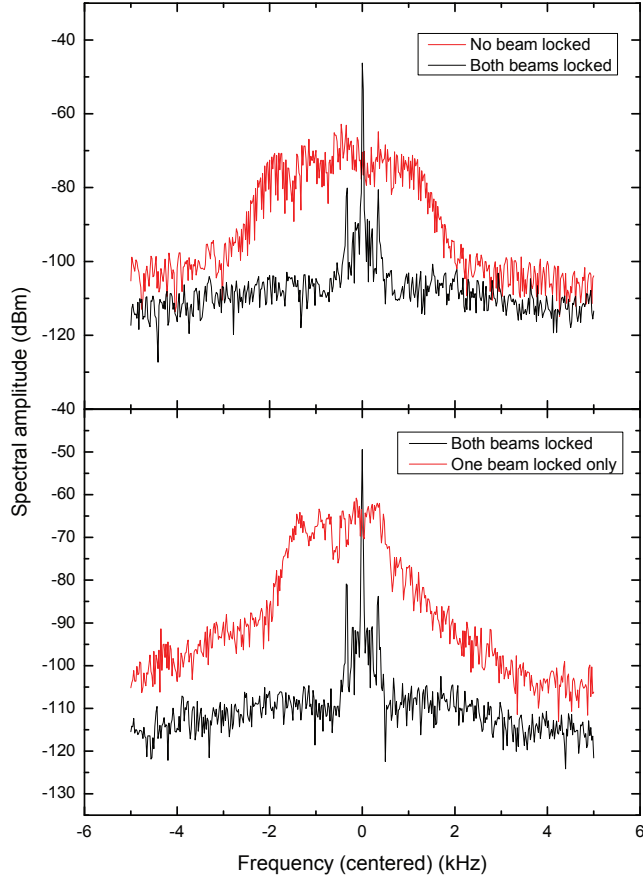


Figure 4.7: Measurement of the phase noise on the beat note between two phase-locked beams. It shows unambiguously that the noise due to the fiber is suppressed. One of them has been phase-locked with the trial lock-box (connected with wires) which is less efficient and the small peaks about 500Hz away from the main peak should not be there with two of the PCB version lock-box. The absolute center frequency is 1MHz.

related is very simple: one only needs to block the detected light and if the noise floor significantly goes down, then the noise is mainly due to the light noise. Our measurement was indeed limited by a light-related noise for the measurements of this subsection.

By having a look at the noise spectrum on a broader scale like on Fig. 4.6, we can see that the suppressed noise is indeed reaching the noise floor within a few dB. Seen on an even broader scale of, say, 2MHz, the noise floor has been observed to be very close to the level reached at the borders of this figure.

However, the absolute position of that floor – and not the attenuation – depends strongly on the mode of the laser; on an even wider scale of 50MHz, we see the influence of the mode on the beat note’s shape. We can see the two spectra in Fig. 4.8 which differ by the fact that we slightly changed the pumping current of the laser diode by 2 or

3mA out of 120mA in total between the two, whereas the spectrum of the noise on the scale of a few tens or hundreds of kHz of the previous figures is not affected at all when the current is changed by 2 or 3mW. The two modes displayed here clearly have very different noise floor at the base of the sharp central peak. We conclude from this observation that, still at the base of the sharp central peak, the noise is dominated by laser intensity noise of the photodiode. About 20MHz away from the sharp peak of the black curve, we can see a flatter noise floor, which is the photon shot noise. The laser diode mode drifts slightly with time despite the temperature control of the diode laser. It might be possible to suppress such drifts by locking the diode to a cavity. The laser diode mode can even be the cause of sidebands of the main peak in the range of tens of kHz. They disappear as well when the pumping current is slightly changed.

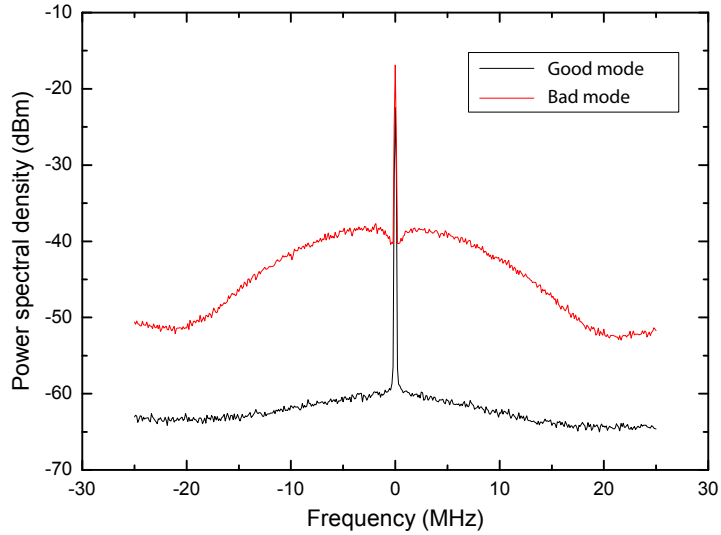


Figure 4.8: This figure shows that two modes are very different in shape over tens of MHz and change the noise floor level on which stands the phase noise peak we want to suppress. One can switch between the bad and the good modes by simply tuning the pumping current of the laser diode.

### 4.3.2 Frequency response

Using a network analyzer, one can measure the frequency response. The network analyzer has a pretty simple principle of operation: it sends an AC voltage  $V_{0,in} \cos(\omega t + \chi_{in})$  through a network and measures then  $V_{0,out}$  and  $\chi_{out}$  after it. The network has to be linear in the sense that the output must still have an angular frequency  $\omega$ . The device has three port: a source port (called “LF OUT”) which emits a signal, a reference port (called “R”) where  $V_{0,in}$  and  $\chi_{in}$  are measured and a test port (called “T”) where  $V_{0,out}$  and  $\chi_{out}$  are

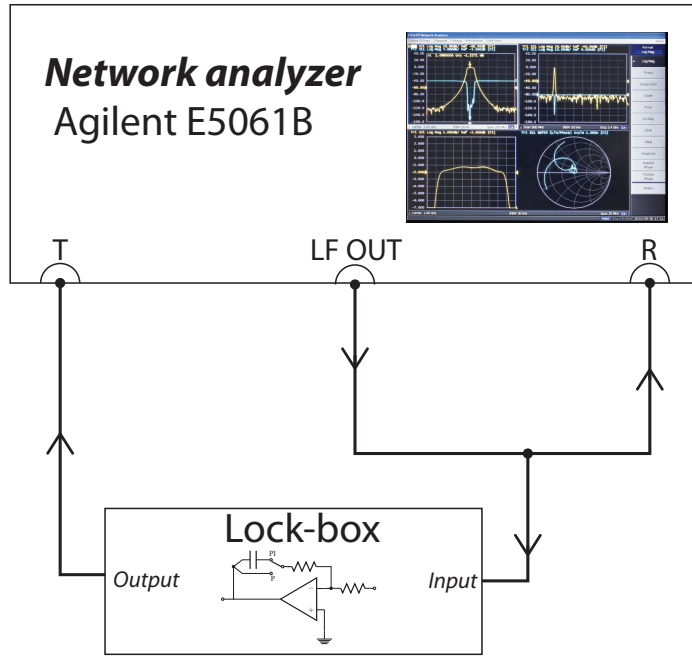


Figure 4.9: It is shown here how to connect the network analyzer to the lock-box when we want to measure the transfer function of the lock-box alone

measured. A vector network analyzer displays  $\chi_{out} - \chi_{in}$  and  $V_{0,out}/V_{0,in}$  while a scalar one only displays the latter.

The first thing we can test is the frequency response of the lockbox alone with the connections shown in Fig. 4.9 and the result of that measurement is presented in Fig. 4.10. That figure corresponds to the response of the lockbox with settings of gain corresponding to a usual use where the loop is actually phase-locked without too high a gain. The loop is able to acquire lock with such a low gain because the rest of the loop provides other stages of amplification which increase the gain. It is not possible to test the frequency response of the lock-box alone when it has an integrator: indeed, as we mention in Appendix E (Sec. E.4) the DC component of the input can build up into a large voltage and drive the controller into saturations and out of lock. When the loop is closed, it becomes possible to test the integrating part of the controller.

The next step is to see how the whole loop responds. In order to inject the noise into the network, one can use the schemes showed in Fig. 4.11. Resistive power splitters/combiners which work from DC to 4.2GHz are used to successively:

- inject a signal in the loop
- sample some of it as a reference
- “wait” for the signal to propagate along the loop

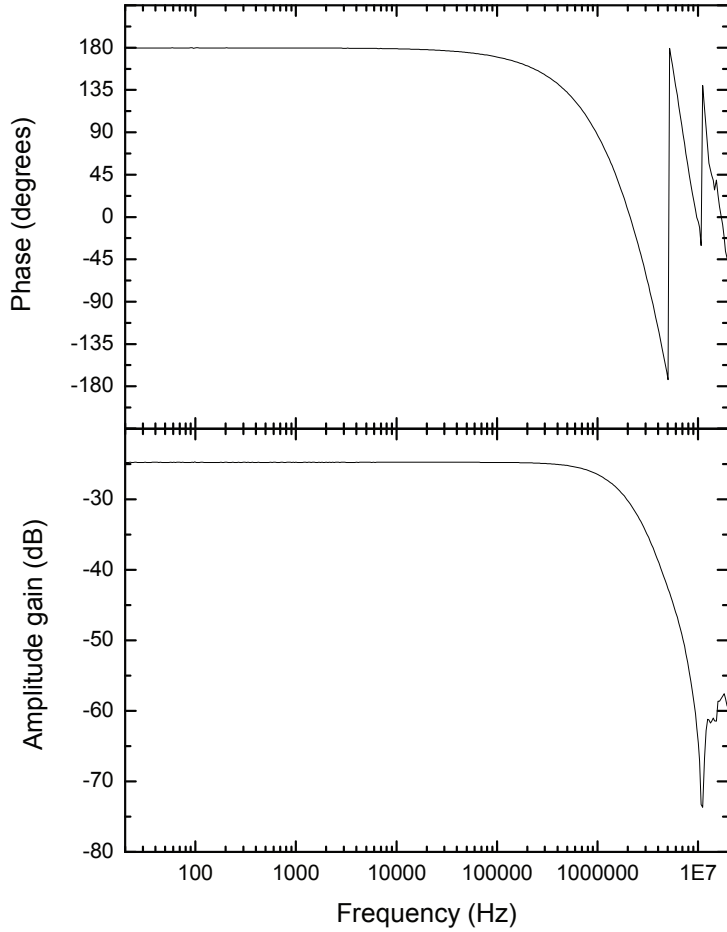


Figure 4.10: The above graphs show the amplitude and phase gain of the lock-box alone as measured by a network analyzer. The amplitude response is nicely proportional up to about 1MHz. As expected the phase is also constant equal to  $180^\circ$  (and not  $0^\circ$  due to the convention of the network analyzer).

- probe it after the (linear) loop as processed it.

The results of that measurement are shown in Fig. 4.12. First we see that turning up the proportional gain of the loop filter just translates the curve up and down, like it should. As far as the lock with a PI controller is concerned, we do see the smooth transition from the behaviour of a doubly-integral controller with a slope of  $-40\text{dB}$  per decade to a single integral controller with half the slope around  $70\text{-}80\text{kHz}$ . We see that it looks much like the theory on the right of Fig. 4.4.

We can find the point of unity gain. It is not directly the point where the lines of Fig. 4.4 cross the  $0\text{dB}$  line because there are splitters in the loop.  $P_x$  denotes here the power *in dBm* at point  $x = 1, 2, 3, T, R$  in Fig. 4.11. The open loop gain is the gain between the points 2 and 3:  $G_{ol} = P_3 - P_2$ . The gain displayed by the network analyzer is  $P_T - P_R$ . The resistive

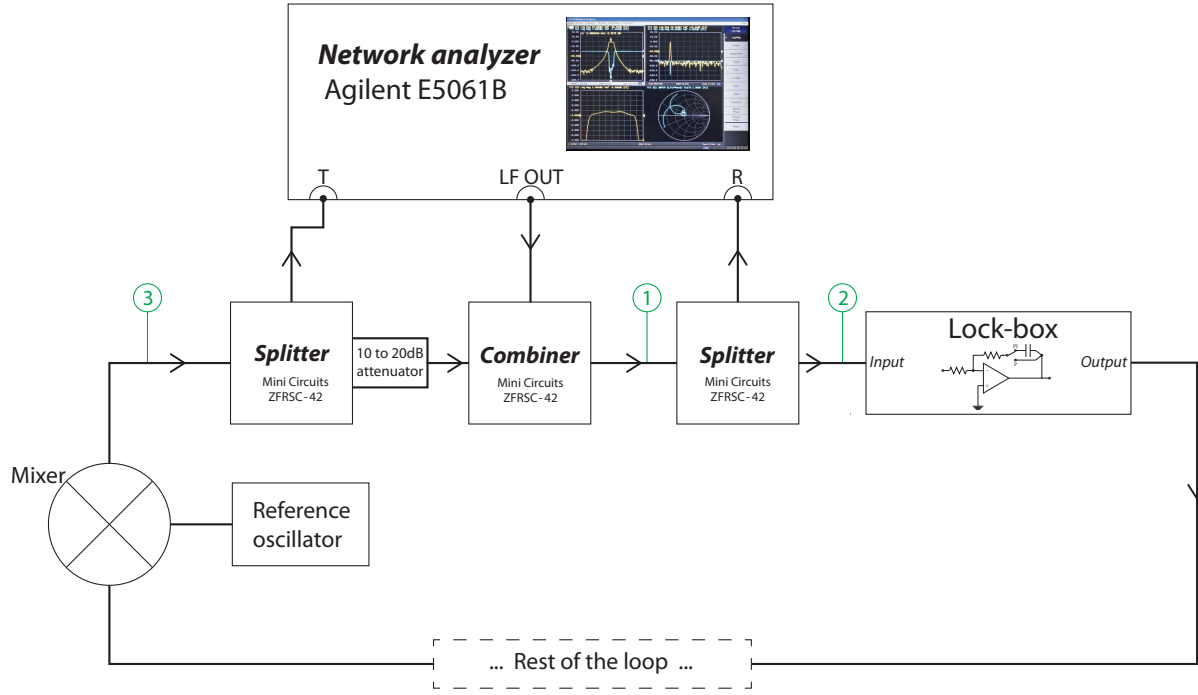


Figure 4.11: Connections used to measure the transfer function of the whole loop in phase-lock. It has been done using the splitters/combiners in the way shown in the above figure. All the loop is exactly identical to what is in Appendix F except for the splitters/combiners and the network analyzer stuck between the mixer and the lock-box. The 10 to 20dB attenuator is used to prevent the signal emitted from LF OUT to leak through the splitter connected to the T port, reach that port and spoil the measurement. Indeed, the resistive splitters/combiners used do work at DC but have a very poor degree of isolation between ports. Without that attenuation, when the gain is low enough the leaked signal takes over the signal that has propagated around the whole loop and the transfer function is artificially flattened at frequencies where the loop is in fact still completely operational.

splitters are such that  $P_R = P_1 - 6\text{dBm} = P_2$  and  $P_T = P_3 - 6\text{dBm} = P_2 + G_{ol} - 6\text{dBm} = P_R + G_{ol} - 6\text{dBm}$ . It means that the quantity of Fig. 4.12 is  $G_{ol} - 6\text{dBm}$  and that unity gain  $G_{ol} = 0\text{dB}$  happens where the curves reaches -6dB. We can then read that the unity gain point is around 430kHz (resp. 820kHz) for the green (resp. red) curve.

Let us now look at the phase. For the P controller, it starts at  $90^\circ$  because of the inherent integrator of the PLL and its evolution as frequency increases is dominated by a delay coming, for a large part, from the dead time. For the PI controller, it starts with the expected  $90^\circ$  difference compared to the P gain and in the range where it should transition to a purely P gain, the delay becomes dominant.

The alignment process needs one optimization step when one takes the dead time into account: the AOM is firstly align to get the highest diffraction efficiency and then the

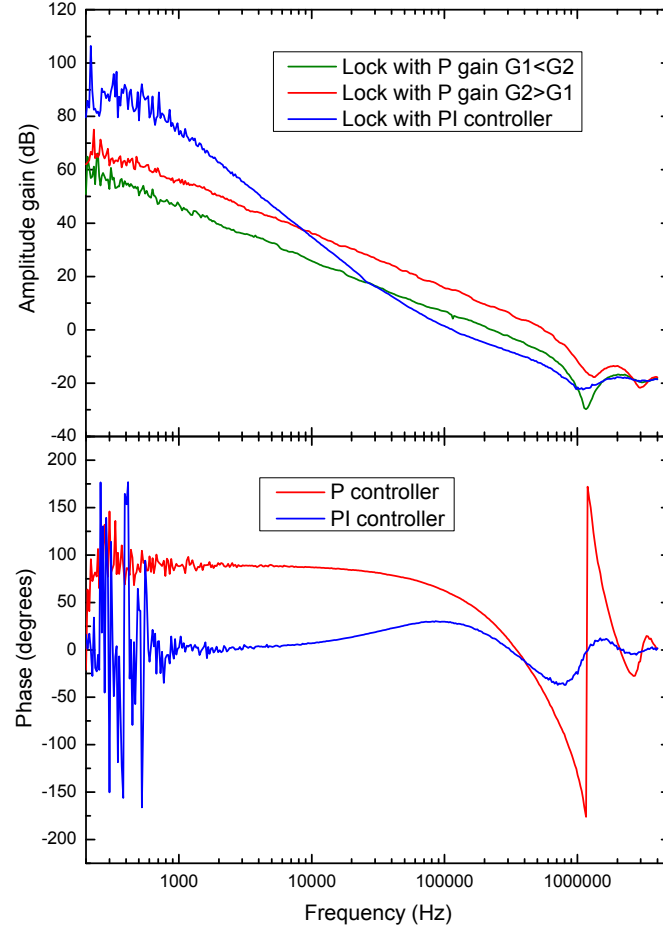


Figure 4.12: Results showing the transfer function around the whole PLL as measured according to Fig. 4.11 in different configuration of the loop filter. Commented in the text.

dead time is measured and minimized while checking that the diffraction efficiency does not go down significantly. Fig. 4.13 presents the data coming from three alignment with different dead time but same gain. Obviously the dead time has a significant influence on the phase lag around the loop. The phase in radians related to a delay of  $\Delta t$  is  $\phi_{\text{rad}} = \omega \cdot \Delta t = 2\pi f \cdot \Delta t$  and so  $\phi_{\text{deg}}/360^\circ = \Delta t \cdot f$ . According to that last formula, the slope of the data gives us the corresponding delay. The following table gives us the outcome of a fit of the lines of Fig. 4.16.

Value from fit (ns)	Measured value (ns)
630	340
680	460
810	530

It means that the dead time is not the only origin of the phase shift despite the fact that we see an important influence of the dead time.

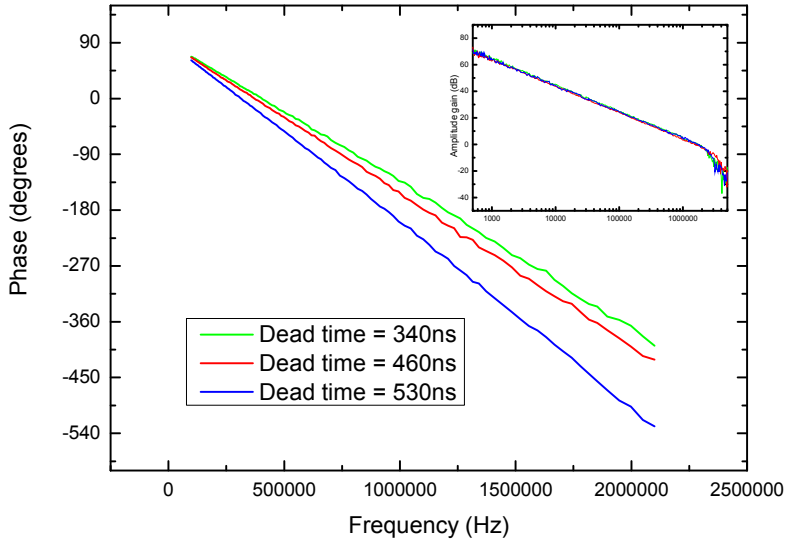


Figure 4.13: Here we can see how the phase changes as the dead time is being adjusted, with constant amplitude gain (insert on the upper right). It has an important contribution but cannot account for the whole delay.

### 4.3.3 Transient response and steady-state error

In this subsection, we want to show how the fast and how good the loop is acquiring lock.

As we switch on the signal, even if the loop is well adjusted and stable, it cannot be instantaneously in lock because the signal has at least to complete once the loop path at finite speed in order to allow the “feedback equation”  $\Phi_e = \Phi_r - \Phi_s$  (Secs. E.2 & E.3 provides more specification about that) to have any meaning at all.

Determining the locking speed is simple in its principle: we send a pulse to the AOM and monitor the error signal on an oscilloscope to see when it falls in the phase-locked state where the error signal is equal or close to 0. It can be done by two methods. One is to just switch the RF signal fed to the AOM on and off.

The other method is somewhat more involved. The AOM can be operated in a feedback loop, the purpose of which is to lock the *intensity* of the beam diffracted by the AOM in the first order. That lock is independent of the phase lock we have been describing so far in this chapter. It consists in, firstly, detecting the intensity of the diffracted beam with a photodetector; the voltage produced by that photodetector is fed back to the AOM driver and the latter makes sure that detected voltage is following a control voltage. It allows us to ramp up and down the diffracted light with an arbitrary form.

It is very important for us to see how much time it takes for the loop to acquire lock for the following reason: the lattice potential cannot be there at full height during the

whole time of the experimental sequence on quantum degenerate atoms lasting a few tens of ms, it has to be switched on and/or ramped up. If the laser beams have noisy phases for too long, the atoms could heat during that time and completely spoil the result and reproducibility.

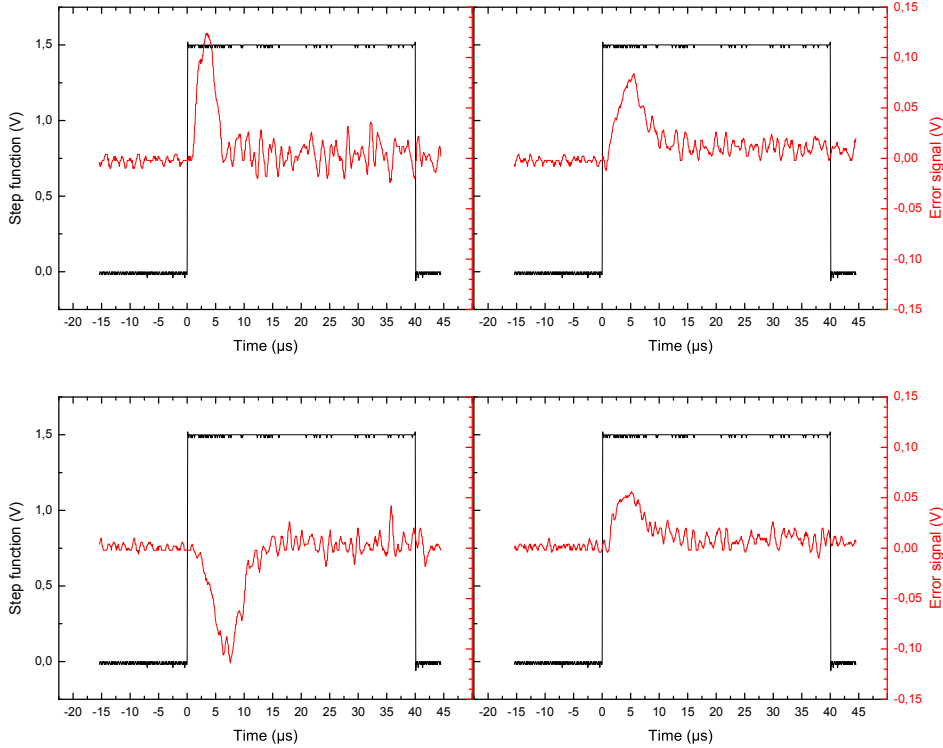


Figure 4.14: This figure shows four transient responses to a pulse. We see that the error signal is regulated after around  $10\mu\text{s}$ . The exact response changes when we measure at different moments because the random phase noise produces different error signals at different times. We still see some noise at high frequencies in the phased-locked state.

Fig. 4.14 shows the error signal when the loop is quickly switched on to 90% of the maximum diffracted intensity. It has to be compared to Fig. 4.15 where the error signal measured without the lock (the loop filter is shorted) and we see the blatant difference. The system goes in the locked state where the error signal is maintained close to 0 in about  $10\mu\text{s}$ .  $1/10\mu\text{s} = 100\text{kHz}$  is much more than the critical frequency mentioned in Sec. 4.1: the noise would not have enough time to come into play while the loop is not locked and it should not harm the experiment.

We can clearly see that there is still some noise even when the error signal is kept at 0 because the gain is not high enough for the whole noise spectrum to be completely attenuated; that remaining noise is not so critical because it is located above 600kHz in the frequency domain, which is also far away from the frequencies mentioned before in

Sec. 4.1. It is important to have in mind that *changing the overall proportional gain is obviously going to change the transient response* since it means that we attenuate more or less each frequency.

The process of optimization is really crucial. Reducing the dead time allows us to reach higher gain because the point of  $\pi$  rad phase shift is sent to a higher frequency. As a result, a wider range of frequencies are attenuated and we see that it is relevant in the case of our PLL because some noise – albeit not harmful in the experiment mentionned here – is still there in the steady state. *Changing the gain also changes the dynamic response*: the locking speed is increases if the gain is turned up. After optimizing the delay along the loop, it is important to turn the gain of the lock-box as high as possible, as long as there is no peaking appearing in the spectrum on the side of the main peak in the phase-locked state.

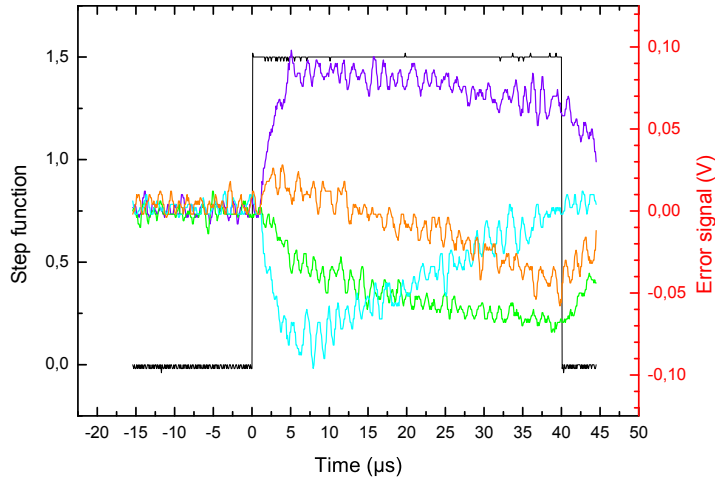


Figure 4.15: We have here four shots of what the error becomes when the loop is not phase-locked (and the AOM is operated with a square pulse). The frequency mismatch between the VCO signal and the reference signal is here close to the minimum achievable.

We mentioned in Sec. 4.2.3 (also in Sec. E.4), the fact that using a P controller or a PI controller changes the steady-state error. We tested it and one can observe the comparison between different behaviour on Fig. 4.16. An error has been introduced by just tuning the VCO frequency slightly off the reference frequency. It is separated in long (on the right) and short (on the left) time scales because we had to use a low integral gain, hence a high capacitor ( $C=100\mu F$ ) corresponding to a large relaxation time  $\tau = RC$ ,  $R \sim 1000\Omega$  in order to be able to switch on with the controller being already on PI position. With a higher integral gain, the loop is not stable on switching on and it is directly driven into a saturation of operational amplifiers of the lock-box. The dynamic response of Fig. 4.16 cannot be directly compared to Fig. 4.14 because how the gain of the two figures compare is not known. On the left side, we see the fast transient response coming from the P part of the controller that allows the loop to acquire lock very fast. After a few  $\mu s$ , it looks

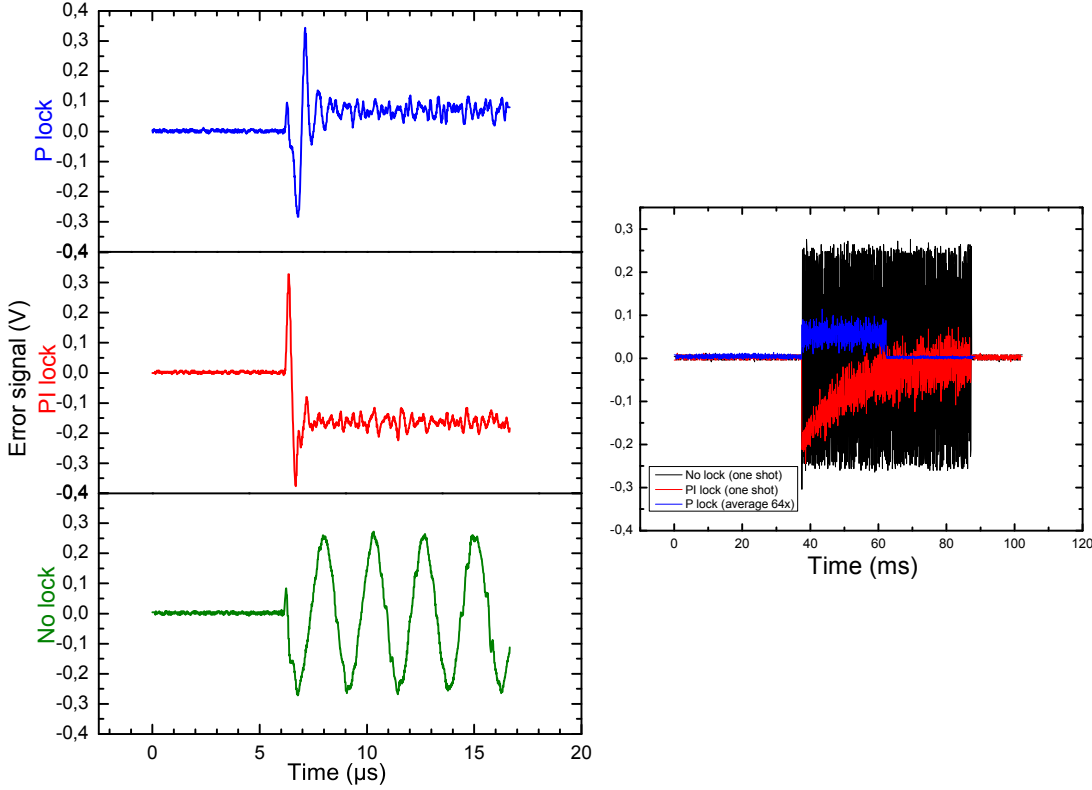


Figure 4.16: Time evolution of the error signal with different gain of the loop filter: measurements over  $17\mu\text{s}$  on the left and  $100\text{ms}$  on the right. We see how the final phase-locked steady state is reached after an evolution over two very different time scales.

like nothing is happening anymore. The time needed to acquire lock is about three times smaller than on Fig. 4.14 because the gain is different. On the right side is how it eventually evolves on a much longer time scale: with P gain, we have a constant error, and with PI gain, the error reduces to a steady state of 0.

#### 4.3.4 Performance of the lock as a function of the light intensity

We show here how the lock performs when the intensity is brought down to a very low value. The question is to know whether ramping up the lock is a doable way to operate and would not submit the atoms to a noisy flux lattice. We use here the intensity lock to regulate the value. The maximum of 100% signal corresponds to about  $110\text{mW}$  of power which is about two thirds of the intensity that would have been used with the TA on the atoms.

Fig. 4.14 shows the noise profile measured by a spectrum analyzer on a  $10\text{kHz}$  span. We see that the phase-lock is still very efficient at transforming the broad signal into a sharp peak. Even at 1% of the maximum intensity, the lock is still working. At 5%, using a PI controller instead of a P controller helps a lot to get a much cleaner phase-lock at low

frequencies and we see that the lock is still very efficient. In that configuration, the use of a double integrator with a PI controller was not stable at 1%. We did not investigate with lower integral gain of the PI lock but it would be nice to be able to switch from P to PI during the ramping up which is not possible with the current version of the lock-box (but will be on an upgraded version.)

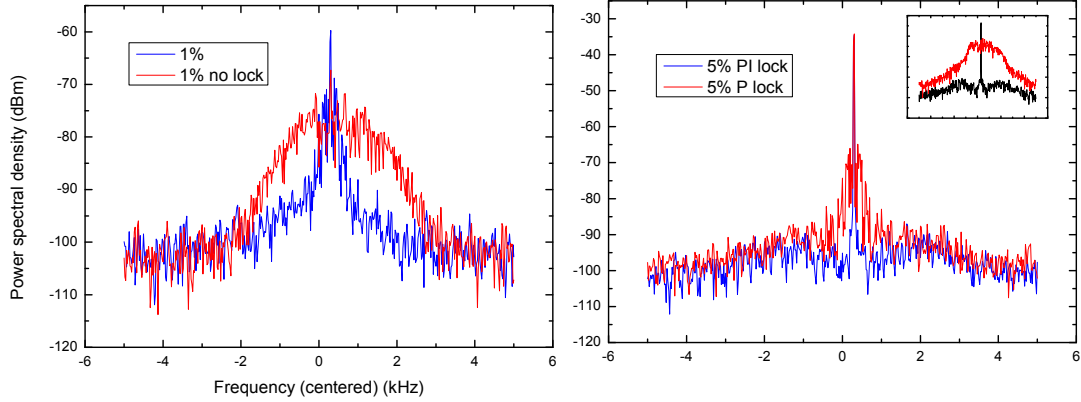


Figure 4.17: We are interested here in seeing whether the lock still works when the intensity is only a small fraction of what it would be when the optical lattice is fully loaded. It indicates us whether it is feasible to ramp up the flux lattice. The small insert in the upper right of the right graph shows the spectrum locked and not locked at 100% intensity.

The conclusion of that is the following: it is possible to switch on the lattice at, say, 1% where its effect should be negligible and ramp it up while staying in lock in a few tens of  $\mu\text{s}$ . With a new version of the lock-box it will be possible to remotely switch on the integral gain.

Should anything go wrong when used on the atoms, it is possible to investigate further:

- whether a lower integral gain of the PI controller can help the loop being stable at 1% while suppressing better the low frequency noise.
- how the the lock behaves by actually ramping up the lattice and looking at the time evolution of the error signal, as we did in Sec. 4.3.3.



# Chapter 5

## Conclusion & outlook

We exposed in this thesis how we build the setup required for the four laser sources necessary to the optical flux lattice scheme. The latter is a quite involved notion, which demands to understand well the quantum interaction of a light field with an atom; it gives us a good example of how puzzling quantum mechanics still is.

The idea of the quantum simulation of a charge in a magnetic field in the context of such a lattice is related to the crucial notion of *Berry's phase* which comes from a Hamiltonian with position-dependent off-diagonal elements. We explained how to engineer such a Hamiltonian with four laser beams.

When adapted to potassium 40, this scheme becomes more complicated than the simple model we of the chapter 2. The optical setup is fairly simple, and includes only common optical elements up to one thing: it is necessary to filter out some parasitic light because the light source used, a semiconductor amplifier, has a too broad spectrum. We showed that it is possible to attenuate it enough. In case the result on the atom is somehow problematic, it could be a good thing to try and measure the attenuation with better tools than the ones explained here for more precise qualitative characterization of the attenuation.

We faced also another problem: the optical fiber leading the four beams to the table where atoms are cooled down is a source of much noise in a frequency range up to 100kHz. That noise would without doubt cause a blurring of the effects of the engineered Hamiltonian and the reproducibility would be very poor. That is why a solution had to be found in order to be suppressed that noise; the right concept that came into play here was the phase-locked loop. We demonstrated in the last chapter that it was possible to get rid of the noise thanks to the coherent interaction of light and sound driven by an electrical RF signal which occurs in an acousto-optical modulator.

Implementing such a scheme – which is only a few weeks away as these lines are written – would undoubtedly be a great advance in the field of quantum simulation with ultracold gases. It would valid one more important possibility in the toolbox of that experimental field, which has already proven itself efficient, for instance is the investigation of the BEC-BCS crossover (more in Ref.[32]). One of the goal of that toolbox is to try and test the relevance of models connected to high-temperature superconductivity. As suggested in Ref.

[33], the idea would not be to try and reproduce very closely all the complexity of a high- $T_c$  superconducting sample but rather to try and find minimal Hamiltonians which exhibit the crucial properties of such a sample. Such a design of simple Hamiltonian would also be a very efficient tool at exploring the complexity of quantum Hall effect and topological properties of metals.

It is possible to engineer Hamiltonians that simulate more intricate interactions, such as non-abelian gauge fields. This could open the field of topological quantum computation [34]. That quantum computation paradigm, connected to the fractional quantum Hall effect, is rather far away from being mastered but has also the large advantage of being robust against quantum decoherence.

# Appendix A

## More details on the electronics

We give here more details on the content of the electronics we designed and some explanation about it.

The lock-box has been integrated to a box containing the electronics for the intensity lock which drives the AOMs. Each of these boxes has been originally build independently of the phase-locked loop we described in this thesis and contained for that reason a VCO. This VCO has been removed from its socket (or unsoldered in one case) and a home-made “SMA-VCO socket” adaptor has been build. It allows us to connect the output of the VCO of Fig. A.1 to the intensity lock circuit inside the box via a SMA cable and use the intensity lock almost as if it were working with its “normal” VCO.

In Figs. A.1 & A.2, we can see the content of the lockbox as a circuit. After the BNC input, there is the input impedance  $R_2$ , which is typically  $50\ \Omega$ . It could and should even be placed on the BNC (and not on the PCB board) if possible. We did not use an input impedance because we were not working with high enough frequencies.  $R_{609}$  controls the gain of the instrumentation amplifier IC601. Infinite  $R_{609}$  corresponds to unity gain and maximal bandwidth of the amplifier. C603, C604, C609, C609, C618, C619 are all filtering capacitances.

The output of IC601 goes on partly to the monitor output.  $R_6$  is also here to increase the gain of the differential amplifier IC603.  $R_8$  should attenuate any noise coming out of IC603 that could add to the main signal.

The rest of the output of IC601 is the input of the loop filter, which is a P or a PI controller. A slot for a capacitor C612 has been added for a potential differential gain. This slot has never been used though.

$R_{612}$  limits the gain and reduces any voltage coming from IC602B to IC601 that could damage IC601. Indeed, the instrumentation amplifier AD8429 (from ANALOG DEVICES) burnt twice from unknown causes. In the final version, the AD8421 (from ANALOG DEVICES) was used. However, we know C606 can charge and have a voltage of 15V across it. Such a voltage directly connected to the output of (with  $R_{611}$  turned to 0) IC601 could damage IC601. Keeping a not too low value of  $R_{612}$  protects IC601.  $R_{612}$  cannot be too high otherwise the gain is limited at a low value and the bandwidth of the lock as well.

R612 was for that reason chosen to about  $400\text{-}500\Omega$ . R607 controls the proportional gain and the frequency where the PI controller goes from P to I gain and C606 controls the integral gain. R607 can only be tuned with a screwdriver from the board and not via the front panel. SW601 can switch the loop filter between P and PI controller or just short it to have a free running loop.

After that comes a summing amplifier; it sums the output of IC602A, a tunable voltage between 0V and 15V (coarse offset) and a much smaller voltage on the order 1-10mV (fine offset) in order to tune the VCO to the frequency we want to operate the AOM at. The fine offset is tuned via a tunable by hand by a potentiometer on the front panel, while the potentiometer the coarse offset is turned thanks to a screwdriver also on the front panel. The OPA2132A from TEXAS INSTRUMENT OPA2132A is one chip that contains both IC602A and IC602B.

Where the output of IC602B goes is controlled by a jumper on JP3. It can go either to an external VCO as tuning voltage via a BNC on the front panel (jumper between 3 and 5) or to the VCO soldered on the printed circuit board (PCB) (jumper between 3 and 4). The constant 12V or 5V operating voltage is provided by IC5. The tuning voltage of the VCO on the PCB can also come from IC5 if the jumper is between 2 and 4; in this case, it is tuned via the potentiometer R9.

The circuit of Fig. A.3 is the part of the lock-box that generates the operating voltages  $\pm 15\text{V}$  used for the operating amplifiers as well as the VCO. The unregulated input voltages of Fig. A.3 comes from the circuit of Fig. A.4: a transformer, connected to the mains (230V AC), and a rectifier have been added at the back of the box for the intensity lock.

The output of the VCO is connected to a SMA connector. The RF signal coming out here goes to the intensity lock which allows to ramp up and down the beam diffracted by the AOM and suppress fluctuations in the intensity of the beam after the fiber. The principle of operation of this intensity lock is worth mentioning: the amplified RF signal fed into the AOM needs to be power-modulated in order to regulate the optical power of the diffracted light; in order to achieve that, the input power of the amplifier is multiplied by a DC component in a mixer and that trick allows to achieve a fast and efficient regulation of the power.

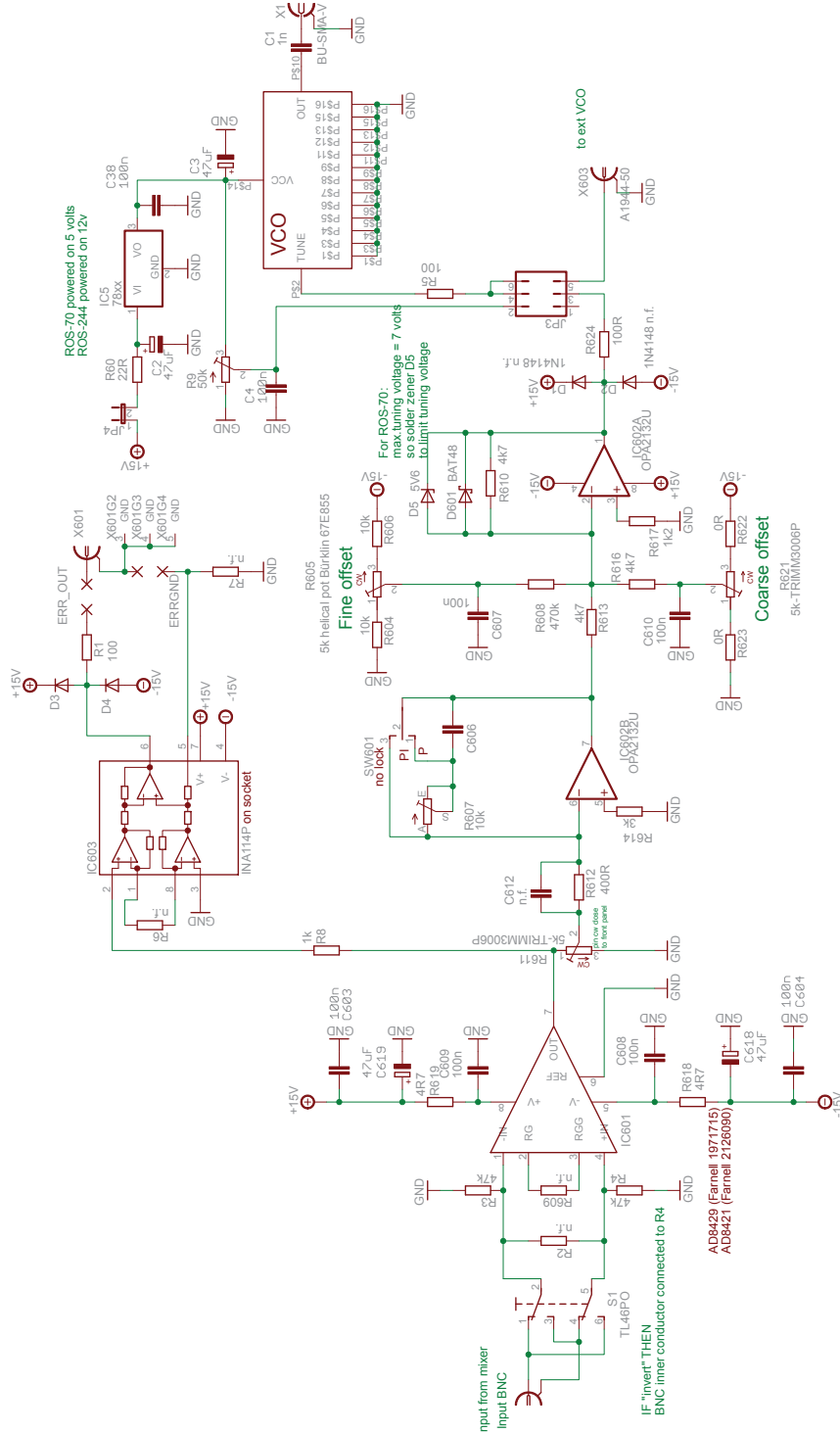


Figure A.1: Circuit of the lock-box which have been designed for the PLL. It contains – among other thing, the loop filter – of the PLL and the VCO which generates the RF signal that is fed into the AOM after an stage of amplification from  $\sim 9\text{dBm}$  to  $\sim 33\text{dBm}$ .

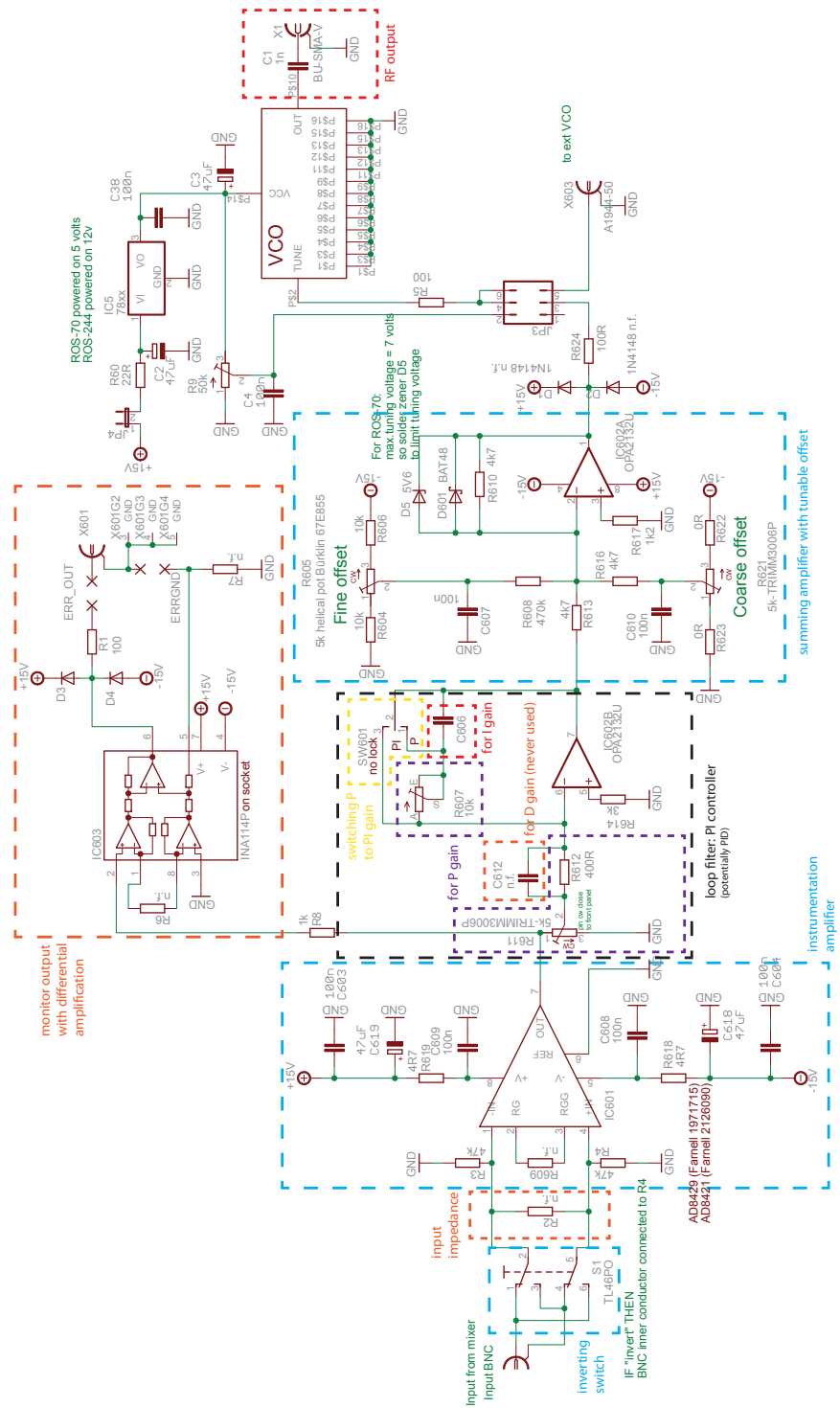


Figure A.2: We can see here what is the function of each part the lock-box. In the text, we give some more details about the components.

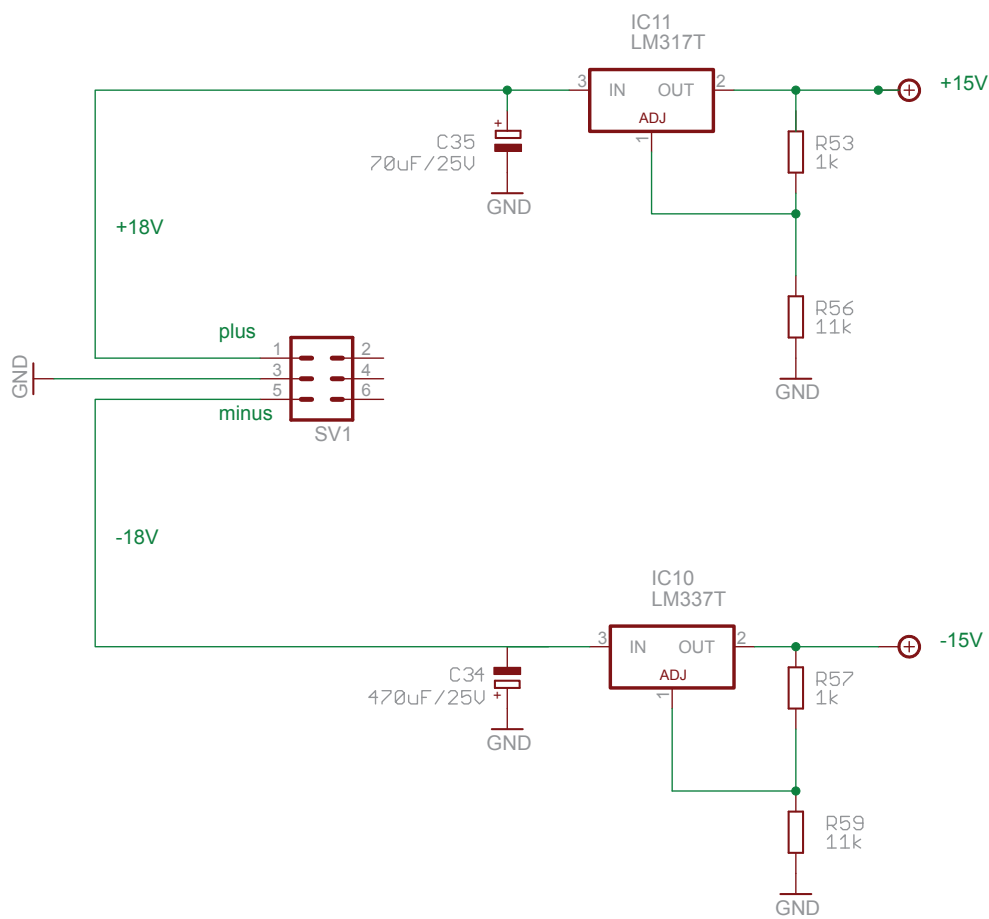


Figure A.3: Part of the lock-box which deals with the DC voltage needed to operate the VCO and the operational amplifiers. The unregulated  $\pm 18V$  inputs come from the circuit of Fig. A.4.

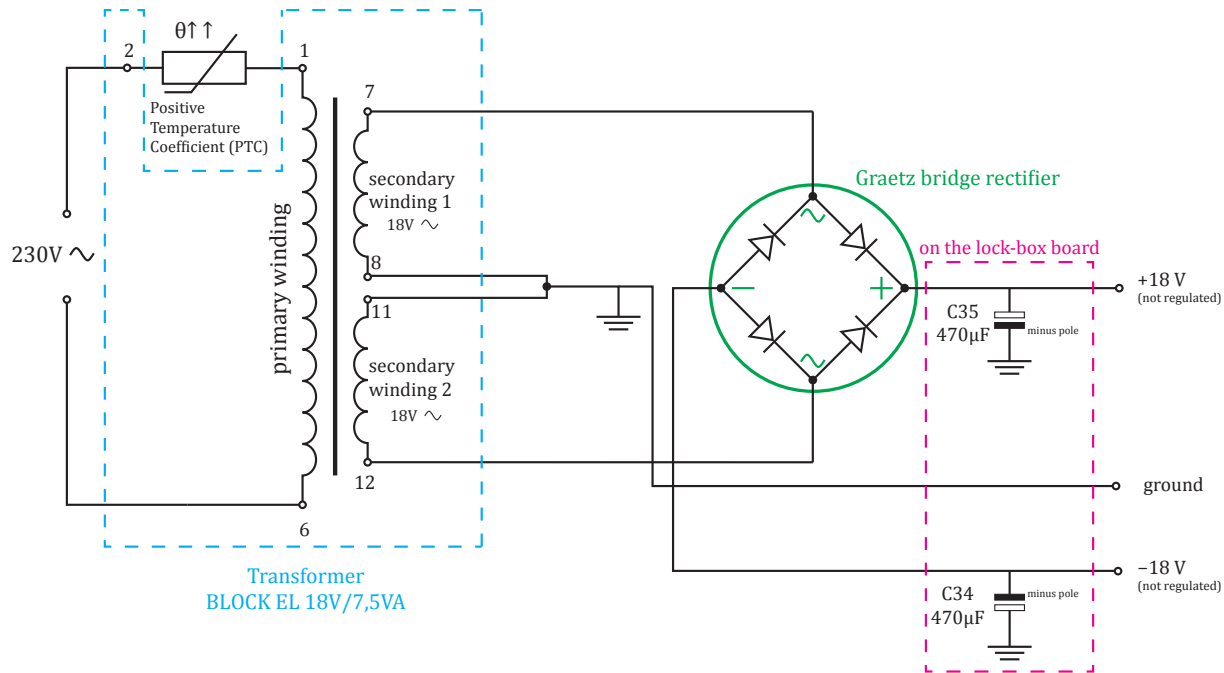


Figure A.4: Circuit added in the electronics box for AC to DC conversion. The electrolyte capacitors C35 and C34 are of course the same as on the previous figure.

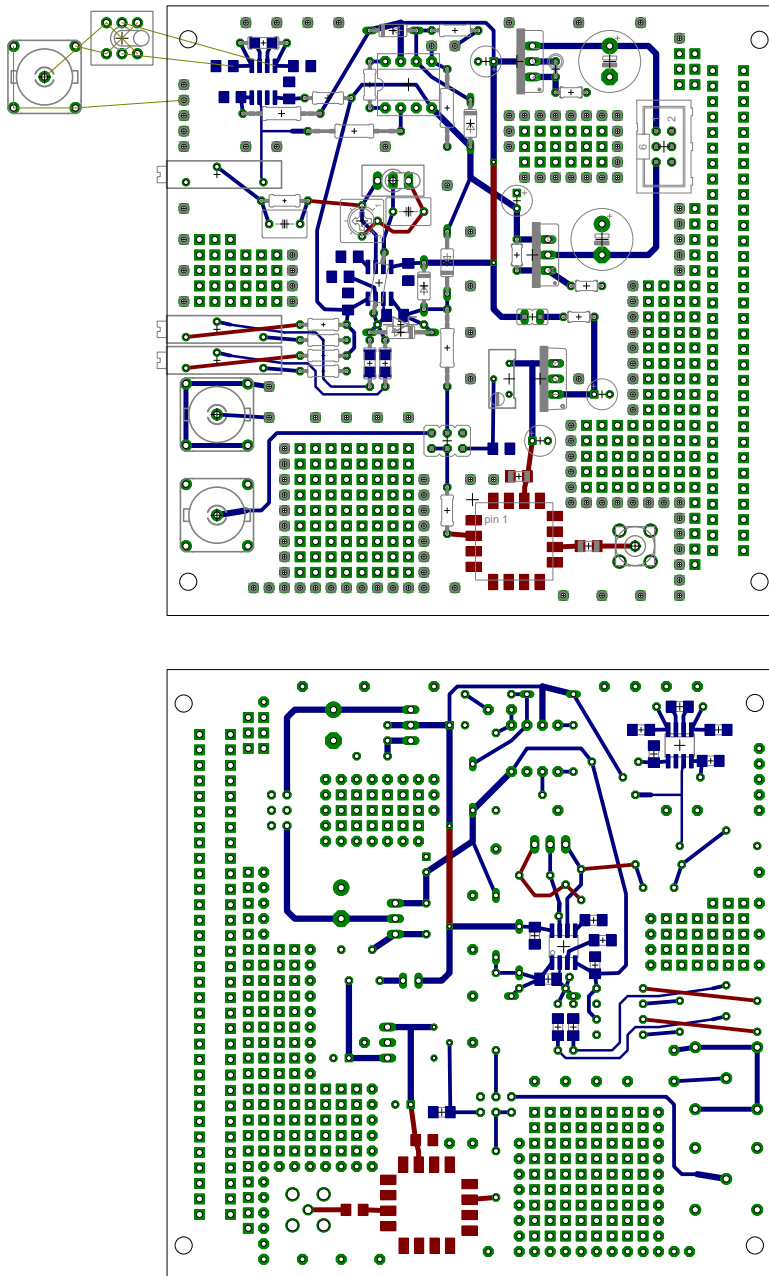


Figure A.5: Picture of both sides of the lock-box printed circuit board. Red and blue correspond to conducting strips printed on the one side or the other of the board. The upper picture is the side with the most parts, and in particular the VCO. The lower picture is the side with all the operational amplifiers.

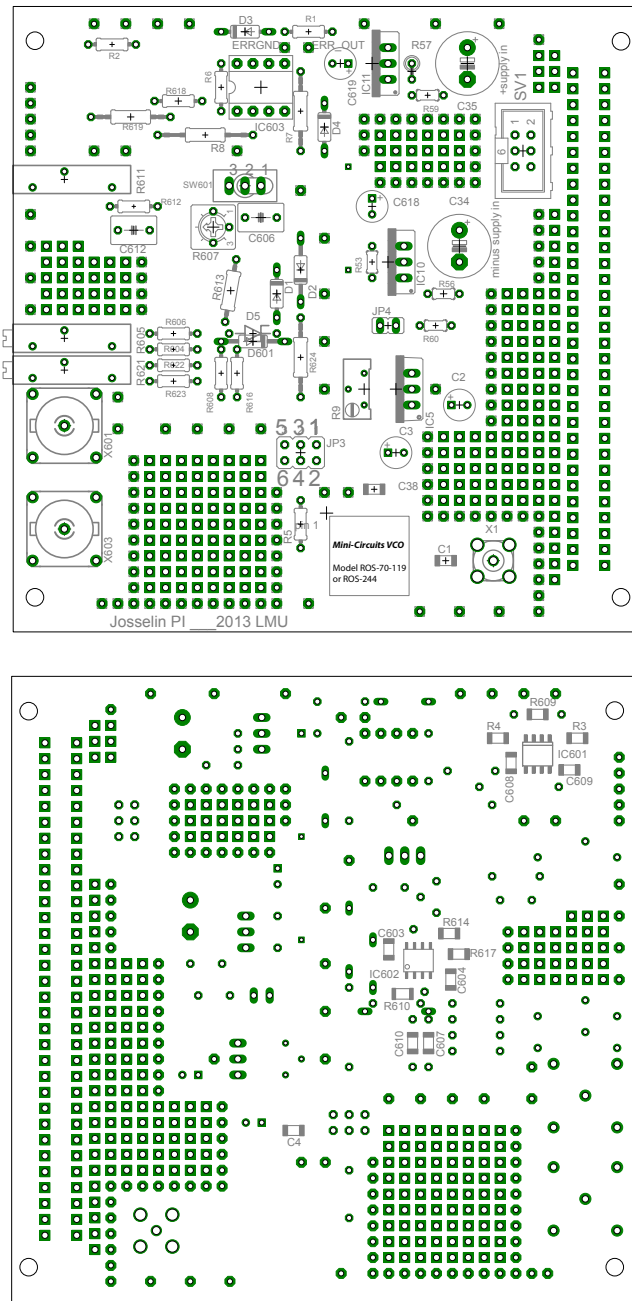


Figure A.6: Picture of both sides of the lock-box printed circuit board with the name of each component and its location.

## Appendix B

# Effective Schrödinger equation for an adiabatic evolution

We assume the atom is a simple two-level system. We consider the presence of a position-dependent coupling  $\hat{U}(\vec{r})$  between the ground and excited state  $|g\rangle$  and  $|e\rangle$  in the Hamiltonian  $\hat{H} = \hat{p}^2/(2m) + \hat{U}$ .  $\hat{U}$  has two eigenstates that form an orthonormal basis  $\{|\chi_1(\vec{r})\rangle, |\chi_2(\vec{r})\rangle\}$  for every  $\vec{r}$  with the eigenvalue  $\hbar\omega_1$  and  $\hbar\omega_2$ : For any time  $t$ , one can decompose the state-vector  $|\psi\rangle$  of the atom on the basis:

$$|\psi(\vec{r}, t)\rangle = \psi_1(\vec{r}, t)|\chi_1(\vec{r})\rangle + \psi_2(\vec{r}, t)|\chi_2(\vec{r})\rangle.$$

Since  $\{|\chi_1\rangle, |\chi_2\rangle\}$  is an orthonormal basis, we have the following properties:

$$\hat{\mathbb{I}} = |\chi_1\rangle\langle\chi_1| + |\chi_2\rangle\langle\chi_2| \quad (\text{B.1})$$

$$\langle\chi_1|\chi_2\rangle = 0 \implies \langle\vec{\nabla}\chi_1|\chi_2\rangle + \langle\chi_1|\vec{\nabla}\chi_2\rangle = \vec{\nabla}0 = 0 \quad (\text{B.2})$$

$$\langle\chi_j|\chi_j\rangle = 1 \implies \langle\vec{\nabla}\chi_j|\chi_j\rangle + \langle\chi_j|\vec{\nabla}\chi_j\rangle = \vec{\nabla}1 = 0$$

It follows from the last line that

$$\langle\chi_j|\vec{\nabla}\chi_j\rangle + \left(\langle\chi_j|\vec{\nabla}\chi_j\rangle\right)^* = \langle\chi_j|\vec{\nabla}\chi_j\rangle + \langle\vec{\nabla}\chi_j|\chi_j\rangle = 0 \text{ which means } \langle\chi_j|\vec{\nabla}\chi_j\rangle \in i\mathbb{R}^3 \quad (\text{B.3})$$

Using  $\vec{\nabla}(|\chi_j\rangle) \equiv |\vec{\nabla}\chi_j\rangle$ , we have:

$$\hat{p}|\psi\rangle = -i\hbar\vec{\nabla}(\psi_1|\chi_1\rangle + \psi_2|\chi_2\rangle) = -i\hbar\vec{\nabla}\psi_1|\chi_1\rangle - i\hbar\psi_1|\vec{\nabla}\chi_1\rangle - i\hbar\vec{\nabla}\psi_2|\chi_2\rangle - i\hbar\psi_2|\vec{\nabla}\chi_2\rangle$$

An adiabatic evolution with  $|\psi\rangle$  prepared in  $|\chi_1\rangle$  leads to  $\forall t, \psi_2(\vec{r}, t) = 0$  and so:

$$\begin{aligned} \hat{p}|\psi\rangle &= -i\hbar\vec{\nabla}\psi_1|\chi_1\rangle - i\hbar\psi_1\left(|\chi_1\rangle\langle\chi_1| + |\chi_2\rangle\langle\chi_2|\right)|\vec{\nabla}\chi_1\rangle \text{ thanks to (B.1)} \\ &= -i\hbar\vec{\nabla}\psi_1|\chi_1\rangle \\ &\quad - i\hbar\psi_1\langle\chi_1|\vec{\nabla}\chi_1\rangle|\chi_1\rangle \\ &\quad - i\hbar\psi_1\langle\chi_2|\vec{\nabla}\chi_1\rangle|\chi_2\rangle \end{aligned}$$

$$\begin{aligned}
\hat{\vec{p}}^2|\psi\rangle = \hat{\vec{p}} \cdot \hat{\vec{p}} |\psi\rangle &= -i\hbar\vec{\nabla} \cdot (\hat{\vec{p}}|\psi\rangle) \\
&= -\hbar^2 [\vec{\nabla}^2\psi_1] |\chi_1\rangle - \hbar^2 \vec{\nabla}\psi_1 \cdot |\vec{\nabla}\chi_1\rangle \\
&\quad - \hbar^2 \vec{\nabla} \cdot [\psi_1 \langle \chi_1 | \vec{\nabla} \chi_1 \rangle] |\chi_1\rangle - \hbar^2 \psi_1 \langle \chi_1 | \vec{\nabla} \chi_1 \rangle \cdot |\vec{\nabla} \chi_1\rangle \\
&\quad - \hbar^2 \vec{\nabla} \cdot [\psi_1 \langle \chi_2 | \vec{\nabla} \chi_1 \rangle] |\chi_2\rangle - \hbar^2 \psi_1 \langle \chi_2 | \vec{\nabla} \chi_1 \rangle \cdot |\vec{\nabla} \chi_2\rangle
\end{aligned}$$

$$\begin{aligned}
\langle \chi_1 | \hat{\vec{p}}^2 | \psi \rangle &= -\hbar^2 [\vec{\nabla}^2\psi_1] - \hbar^2 \vec{\nabla}\psi_1 \cdot \langle \chi_1 | \vec{\nabla} \chi_1 \rangle \\
&\quad - \hbar^2 \vec{\nabla} \cdot [\psi_1 \langle \chi_1 | \vec{\nabla} \chi_1 \rangle] - \hbar^2 \psi_1 \langle \chi_1 | \vec{\nabla} \chi_1 \rangle^2 \\
&\quad - \hbar^2 \langle \chi_2 | \vec{\nabla} \chi_1 \rangle \cdot \langle \chi_1 | \vec{\nabla} \chi_2 \rangle
\end{aligned}$$

$$\begin{aligned}
\langle \chi_1 | \hat{\vec{p}}^2 | \psi \rangle &= \left( -i\hbar\vec{\nabla} \right)^2 \psi_1 - \left( i\hbar \langle \chi_1 | \vec{\nabla} \chi_1 \rangle \right) \cdot \left[ -i\hbar\vec{\nabla}\psi_1 \right] \\
&\quad - \left( -i\hbar\vec{\nabla} \right) \cdot \left[ i\hbar \langle \chi_1 | \vec{\nabla} \chi_1 \rangle \psi_1 \right] + (i\hbar \langle \chi_1 | \vec{\nabla} \chi_1 \rangle)^2 \psi_1 \\
&\quad + \hbar^2 |\langle \chi_2 | \vec{\nabla} \chi_1 \rangle|^2 \text{ thanks to (B.2)} \\
&= \left[ \hat{\vec{p}}^2 - \hat{\vec{A}} \cdot \hat{\vec{p}} - \hat{\vec{p}} \cdot \hat{\vec{A}} + \hat{\vec{A}}^2 \right] \psi_1 \\
&\quad + W \\
&= \left( \hat{\vec{p}} - \hat{\vec{A}} \right)^2 + W
\end{aligned}$$

with  $\hat{\vec{A}} = i\hbar \langle \chi_1 | \vec{\nabla} \chi_1 \rangle \in \mathbb{R}^3$  and  $W = \hbar^2 |\langle \chi_2 | \vec{\nabla} \chi_1 \rangle|^2$ .  $\hat{\vec{A}}$  is real thanks to (B.3). The Schrödinger equation is:

$$i\frac{d}{dt}|\psi\rangle = i\frac{d}{dt}(\psi_1(\vec{r}, t)|\chi_1(\vec{r})\rangle + \psi_2(\vec{r}, t)|\chi_2(\vec{r})\rangle) = \hat{H}|\psi\rangle = \frac{\hat{\vec{p}}^2}{2m}|\psi\rangle + \psi_1 \hbar \omega_1 |\chi_1\rangle + |\psi_2 \hbar \omega_2 \chi_2\rangle.$$

We project the last equation on  $|\chi_1\rangle$ , set  $\psi_2 = 0$  and get:

$$i\hbar \frac{\partial \psi_1}{\partial t} = \psi_1 \langle \chi_1 | \frac{\hat{\vec{p}}^2}{2m} | \chi_1 \rangle + \hbar \omega_1 = \left[ \frac{\left( \hat{\vec{p}} - \hat{\vec{A}} \right)^2}{2m} + W(\vec{r}) + \hbar \omega_1 \right] \psi_1$$

This last equation proves formally that an adiabatic evolution with position-dependent eigenstates leads to the quantum simulation of a vector potential  $\vec{A}$ . The simulated artificial magnetic field is then of course just  $\vec{B} = \vec{\nabla} \times \vec{A}$ . Also a scalar potential  $W$  appears.

## Appendix C

### Picture of the cell and oven for filtering resonant light

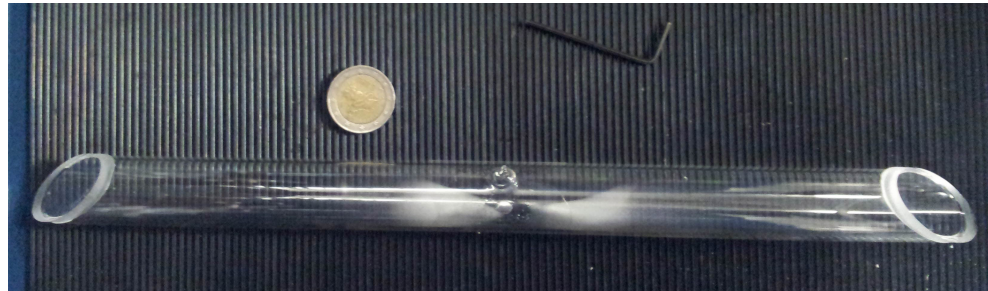


Figure C.1: Picture of the 30cm long potassium through which the laser goes in order to remove the resonant light. We can see the Brewster-cut input faces.

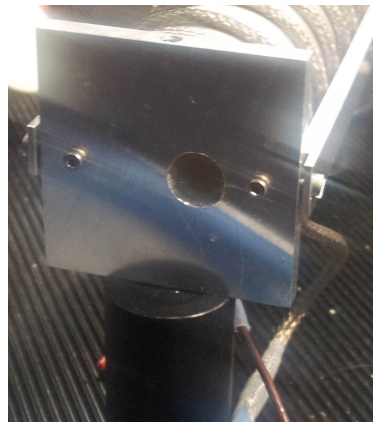


Figure C.2: Side of the cell that is not visible on Fig. C.3. The hole is where the laser beam enters the cell.

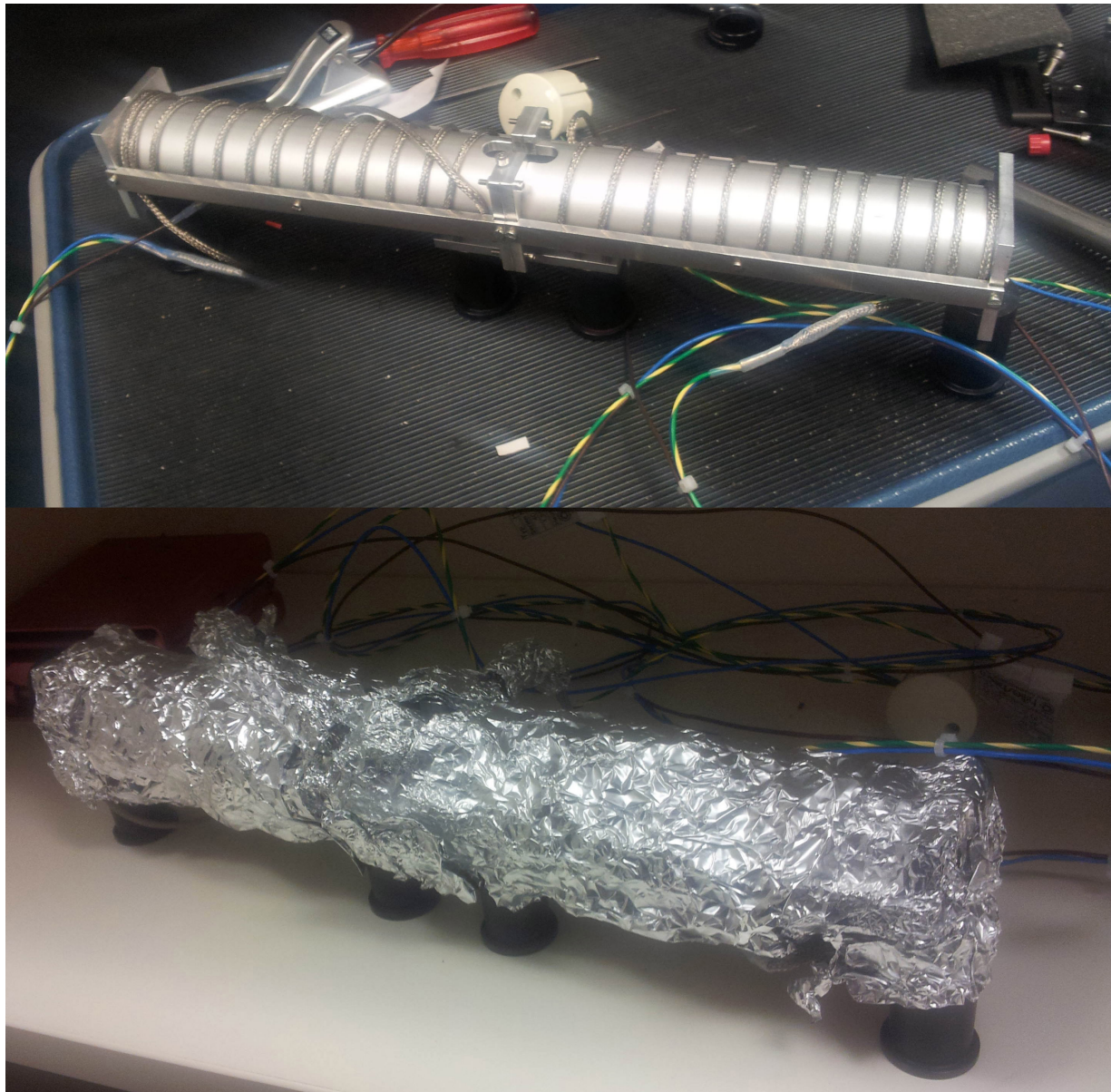


Figure C.3: Upper picture: aluminium oven used to heat up the cell inside it. It is mounted on pedestals. We can see the heating wire wound around it and bars prevent the wire from moving. The oven is made of two identic parts which are screwed together in the middle. We can see a hole in the middle where the cell is visible. That point has more heat exchange than the rest and, as a result is colder: the potassium condenses there and it prevents it from condensing on the input faces of the cell. The oven has been designed using AUTODESK Inventor.

Lower picture: same oven wrapped up in aluminium foil for insulation. Indeed, for a given power fed to the heating wire, more heat exchange with the surrounding air lowers the cell temperature reached.

## Appendix D

### The acousto-optical effect, a coherent interaction

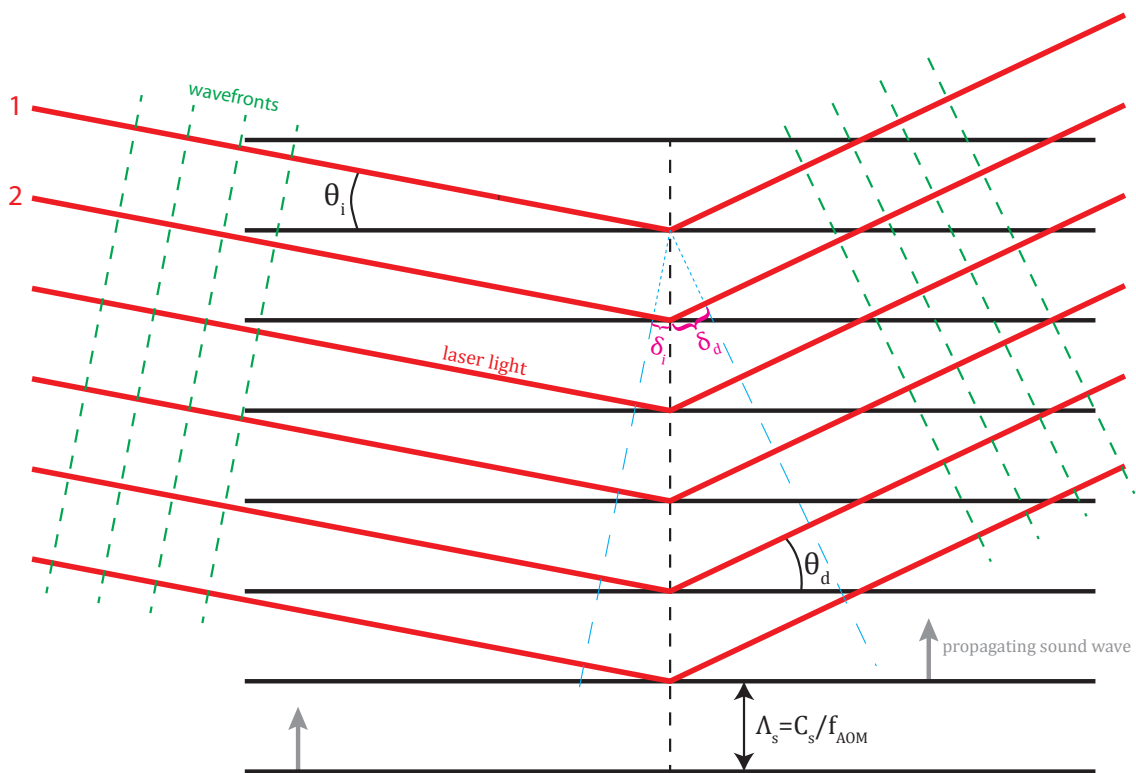


Figure D.1: Here is a model that shows how the light and sound wave really interact. In reality the compression and dilatation in the crystal are sinusoidal and the diffraction planes are not so clearly defined but that model is very good at describing the simple physics of the acousto-optical effect.

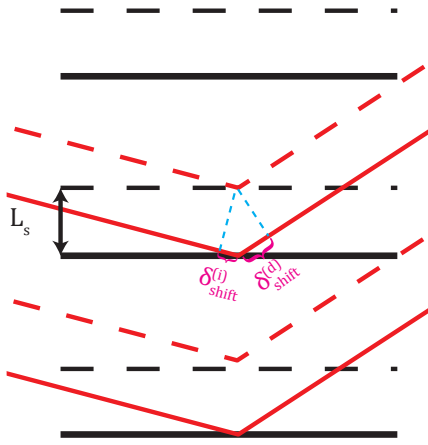


Figure D.2: We show thanks to this figure how a phase shift of the RF signal induces a phase shift on the light.

In our setup, acousto-optical modulators are used. Such devices transmit an RF signal from cables to light beams: it is, in a sense, the complement to a photodetector.

A very simple way to understand the way an AOM works is in the particle picture: photons (light quanta) are passing through a medium where phonons (sound quanta) are also propagating but in the transversal direction. They can interact, and when a phonon “collides” with a photon, momentum and energy are conserved. This leads to an increase in the transversal component of the photon’s momentum and an increase in the frequency or energy of the photon. This is how the photons can be deviated and shifted in frequency.

The interaction described above is coherent, which means the phase of the light is not scrambled while it interacts with the sound. **The phase of the sound is imprinted on the light**, which is *a priori* not obvious when explained with phonons and photons. To understand how this occurs, we need to go a bit more in detail and we basically follow the description of Ref.[35] in chapter 19. The sounds compresses and dilates the atoms in the crystal with a spatial periodicity  $\Lambda_s$ ; this can be interpreted as a grating which diffracts the light. We model the grating by equidistant planes and the light is diffracted by all planes it is shining on, as shown in Fig. D.1. All this resembles very much the situation of X-ray or neutron Bragg scattering. Let us note here that in the case Bragg diffraction for neutrons, there is also incoherent scattering (due to thermal agitation of the atoms on the lattice) which is not present in the acousto-optical effect.

We see light only in the directions where it interferes constructively. In Fig. D.1, the path difference between path 1 and path 2 is  $\delta_i + \delta_d$ . The condition for constructive interference is  $\delta_i + \delta_d = \Lambda_s(\sin(\theta_i) + \sin(\theta_d)) = n\lambda_L$  where  $n$  is an integer that denotes the diffraction order. However this is not the full story because the grating is moving and so the path from the diffracting planes – seen as sources – to an immobile observer in the lab frame is decreasing with time for the light wave, leading to a Doppler shift given by (in

the case of a source moving with  $v_{\text{source}} \ll c$ )  $\Delta\nu = \frac{v_{\text{source}}}{c} \nu_L$ . On Fig. D.1 we see clearly that from one plane to the other, the path difference is  $\delta_i + \delta_d = n\lambda_L$  and an emitting plane has its path changed by that path difference during the period  $1/f_{AOM}$ : as a result,  $v_{\text{source}} = n\lambda_L f_{AOM}$ . Now using  $\nu_L = c/\lambda_L$ , we have  $\Delta\nu = n f_{AOM}$ .

Now if the phase of the sound wave is shifted by  $\Delta\Phi_s$  by changing the phase of the RF wave fed to the transducer, it means the planes are just all translated by a length  $L_s$  such that  $\Delta\Phi_s = K_s L_s$  (see Fig. D.2) with  $K_s = 2\pi/\Lambda_s$ . Just like before, the path length difference for the light compared to the situation before the shift is

$$\delta_{\text{shift}}^{(i)} + \delta_{\text{shift}}^{(d)} = L_s(\sin(\theta_i) + \sin(\theta_d)).$$

That path difference corresponds to a phase  $\Delta\Phi_L = k_L(\delta_{\text{shift}}^{(i)} + \delta_{\text{shift}}^{(d)})$  with  $k_L = 2\pi/\lambda_L$ . Combining all these results with the condition  $\Lambda_s(\sin(\theta_i) + \sin(\theta_d)) = n\lambda_L$  readily yields  $\Delta\Phi_L = n\Delta\Phi_s$ . It means that one can really imprint the phase of the electric signal on the light with an AOM. With the Direct Digital Synthesis (DDS) technology of RF function generators, one can control very precisely the phase of an RF signal and, as a result, also that of the light.

# Appendix E

## Basic control theory and PLLs more specifically

### E.1 The general feedback loop

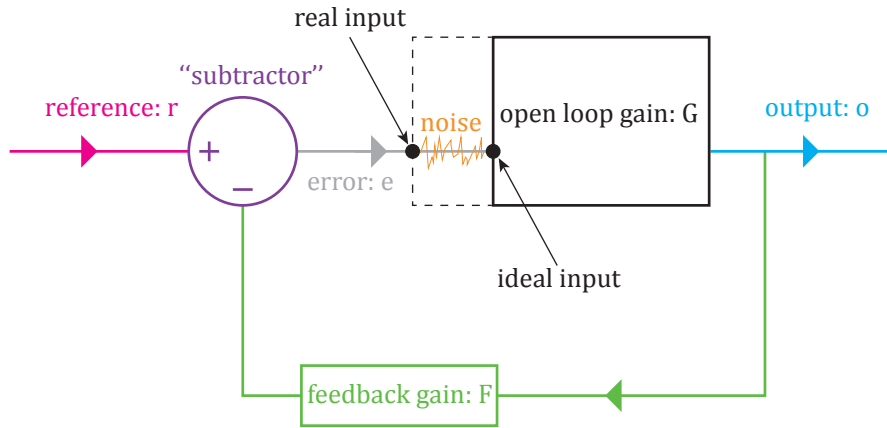


Figure E.1: Very general representation of a negative feedback loop. One can understand and deduce all of the important properties of such a loop from this diagram.

The probably most intuitive idea used to control a system with any kind of output quantity is to form a closed loop, where the output is used to regulate the input. It is very efficient at stabilizing an unstable behaviour compared to an open loop system. A close loop can be represented in a simple form by the block diagram in Fig. E.1.

The problem is the following: we want to use the output  $o$  of whatever device is inside the black block, but it has some intrinsic noise or deviation as soon as it is connected. The goal is to have a nice and constant output that follows the reference  $r$  and thus have a vanishing error  $e = r - Fo$  using a *negative feedback loop*. Positive feedback would merely mean  $e = r + Fo$ . To achieve this we can change the time-independent *open loop gain*  $G$ .

Let us note that we have not assumed anything about the sign of  $F \cdot G$ , which determines whether the feedback is positive or negative. We drew in Fig. E.1 a feedback block with a (time-independent) gain  $F$  because it is the most general case; in electronics, however, inputs and outputs are mostly voltages (or currents) and so a simple wire can be used to close the loop, setting  $F = 1$ .

Our loop is described by  $o = Ge, e = r - Fo$  which means

$$e = r - F \cdot Ge \Leftrightarrow e/r = \frac{1}{1 + F \cdot G}, F \cdot G \neq -1. \quad (\text{E.1})$$

A vanishing error thus corresponds to  $G \gg 1$  if we assume that  $F = 1$ . If we manage to build a system that follows these extremely simple equations with a high open loop gain  $G$ , then the error will be attenuated by itself. **This will happen regardless of whether the feedback is negative or positive and only stems from eq. (E.1).** The important point of *this model* is that the error  $e$  determines itself and one must not see the attenuation process as happening sequentially. If it did, and one could describe the process as  $e_{n+1} = r - FG e_n$ , then this arithmetico-geometric sequence would go to zero if  $G < 1$ . In this case, the smaller  $G$  is, the faster the error would decrease, but this does not correspond to the **steady-state situation** which we describe in the frame of this feedback loop and where the error is always instantaneously defining itself according to  $e(t) = r - F \cdot Ge(t)$ .

Still assuming  $F = 1$ , having a high  $G$  does not really mean that the error is amplified but that the gain  $G$  can be seen as a **sensitivity when the loop is closed**: the higher  $G$  is, the smaller the error can be for the system to start “feeling” it. Now if  $G = -1$ ,  $e/r$  is infinite, the system behaves like an oscillator, which is the worst possible case if we are trying to suppress noise. This happens in the case of *positive feedback*. Naively, if the feedback stays negative, nothing can go really wrong. If we think about more elaborate and realistic time-dependent situations as in Sec. E.4, negative feedback is not always straightforward. For  $G \ll 1$ ,  $e \approx r$ : nothing happens, the noise remains unchanged.

## E.2 General consideration about PLLs

The principle of a PLL is to have a signal follow a reference, where the signal oscillates and is represented by the periodic function  $\psi \mapsto P(\psi)$  characterized by a global *time-dependent phase*  $\psi(t)$ ; we consider  $\psi$  to have a central frequency  $\bar{\omega}$ , and so  $\psi(t) = \bar{\omega}t + \phi(t)$  where the rms value of  $\dot{\phi}$  is much smaller than  $\bar{\omega}$ . The instantaneous frequency is defined by  $\omega(t) = \dot{\psi}(t)$ . The most commonly used variable oscillator in electronics is the VCO for which the relationship between tuning voltage  $v_t$  and angular frequency  $\omega_s$  is

$$\omega_s(t) = \bar{\omega}_s + K_V v_t(t) = \bar{\omega}_s + \dot{\phi}_s(t)$$

where  $K_V$  is the tuning sensibility in MHz/V (usually slightly frequency-dependent but we will not consider it here).

Our goal is to have a vanishing difference between the reference and the VCO phases

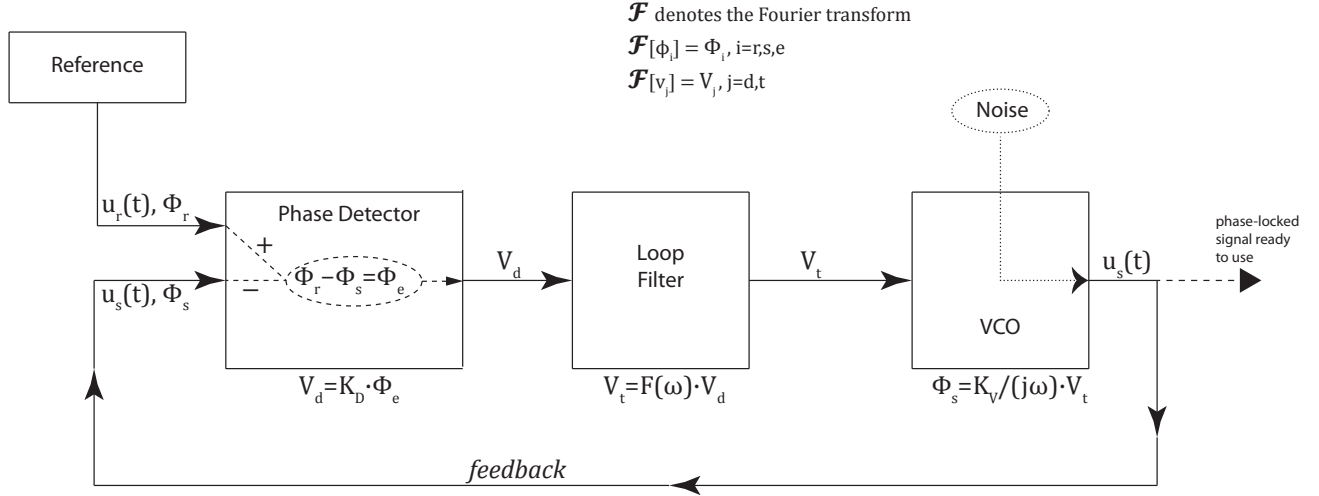


Figure E.2: A PLL consists of three main parts: a phase detector, a loop filter and a VCO assembled in a closed loop. Quantities denoted by capital letters on this picture belong to the frequency domain.

$\phi_r$  and  $\phi_s$ . The phase difference between the VCO and the reference is measured by a *phase detector* and turned into a voltage called the *error signal*. The following table sums up the description of each quantity;  $\emptyset$  does not mean that the quantity cannot be defined but that it is not useful for us.

Quantity in the time domain	Quantity in the frequency domain	Description
$u_s(t) = U_{0s} \cos(\omega_s t + \phi_s)$	$\emptyset$	RF voltage of the signal, of the reference
$u_r(t) = U_{0r} \cos(\omega_r t + \phi_r)$	$\emptyset$	angular frequency of the signal, of the reference
$\omega_s, \omega_r$	$\emptyset$	phase of the signal, of the reference
$\phi_s, \phi_r$	$\Phi_s, \Phi_r$	phase error
$v_d$	$V_d$	error voltage, output of the phase detector
$v_t$	$V_t$	tuning (input) voltage of the VCO
$K_D, K_V$	$K_D, K_V$	gain of the phase detector, of the VCO
$\emptyset$	$F(\omega)$	transfer function of the loop filter

This error is then processed by a *loop filter* which is the main component with some tunable parameters to help us attenuate the error. The processed error is then *fed back* to the VCO and the loop is closed.

It is important here to notice that any PLL, independent of its loop filter, always has a “built-in”, intrinsic integrator in the VCO: the voltage  $v_t$  is the control parameter and it is locally proportional to its frequency deviation according to  $\omega_s(t) = \bar{\omega}_s + K_V v_t(t)$ . The measured output of the VCO that one tries to stabilize is a phase  $\phi_s = \int \dot{\phi}_s = K_V \int v_t(\tau) d\tau$ , which leads to the presence of an integrator.

The frequency of the signal which we wish to phase-lock has nothing to do with the speed of variation of the error; in our case, the frequency of the radiofrequency signal that we phase-lock is 200MHz and we want to suppress noise with Fourier components of at most 500kHz.

### E.3 The PLL in the Fourier domain

Let us now study the more specific frame of the PLL, which is also a feedback loop. We follow mainly the explanation of Ref.[36] and invite the reader to use that book for further development about PLLs. We consider the general block diagram representation of a PLL shown in Fig. E.2 where the gain  $G$  of Fig. E.1 is decomposed into the loop filter, the VCO and the proportional gain of the phase detector.

We are interested in how the loop reacts at different time scales. In order to investigate this, we will be studying the frequency response of our loop and will therefore switch, for some part of the explanation, to the frequency/Fourier domain. In order to quantitatively describe the loop we assign to each part of it – also called a *network* – a *transfer function*  $\mathcal{H}$  represented in the Fourier domain by:

$$\mathcal{H}(\omega) = |\mathcal{H}(\omega)| e^{i \text{Arg}(\mathcal{H}(\omega))}$$

where  $\text{Arg}(\mathcal{H}(\omega))$  and  $|\mathcal{H}(\omega)|$  are the gains in phase and amplitude respectively.

This transfer function is by definition the *ratio of the output quantity to the input quantity* and in the case of a usual PLL, quantities are either phases or voltages.  $|\mathcal{H}|$  tells us how much the signal is amplified or attenuated as it goes through the network whereas  $\text{Arg}(\mathcal{H})$  expresses how much delay the network introduces *i.e* how fast the network can process the time-dependent input signal. A basic Fourier analysis result we should mention – even if we will not use it – is that multiplying frequency dependent transfer functions of networks that are connected in series is equivalent to a *convolution* in the time domain (and *vice versa*) ; a basic result we will use is that an differentiation (resp. a integration) amounts to a multiplication by  $j\omega$  (resp.  $\frac{1}{j\omega}$ ) in the Fourier domain.  $j$  is the imaginary unit defined by  $j^2 = -1$ .

Thus, with the convention that capital letters are quantities in the frequency domain:

$$\begin{aligned} V_d(\omega) &= K_D \Phi_e(\omega) \\ V_t(\omega) &= F(\omega) V_d(\omega) \\ \Phi_s(\omega) &= \frac{K_V}{j\omega} V_t(\omega) \end{aligned} \quad (\text{E.2})$$

$K_V$  and  $K_D$  are taken to be frequency-independent contrary to the loop filter gain  $F(\omega)$ .

Now using the definition  $\Phi_e = \Phi_r - \Phi_s$ , we can compute the ratio  $\Phi_s/\Phi_r$  as a function of  $K_D$ ,  $K_V$  and  $F(\omega)$  thanks to eq. (E.2) and it yields:

$$H_L(\omega) = \frac{\Phi_s}{\Phi_r} = \frac{G_{ol}(\omega)}{1 + G_{ol}(\omega)} \text{ where } G_{ol}(\omega) = \frac{K_V K_D F(\omega)}{j\omega} \text{ is the open loop gain.}$$

The very purpose of our lock is that we want to have  $\Phi_r = \Phi_s$  which happens only in the limit  $|G_{ol}| \rightarrow +\infty$ : *we want to reach a high open loop gain* as we mentionned previously in Sec. E.1. As we already said, the tunable part of  $G_{ol}$  is the filter's transfer function  $F(\omega)$  and that is what we will be studying. The *error gain* is  $\Phi_e/\Phi_r = 1 - H_L(\omega)$  and must go to zero as much as possible.

It is very often assumed that the filter must have some low-passing function because the error signal always contains some quickly oscillating components that has to be suppressed in addition to its average value which is the relevant content.

A filter is said to have a proportional (P) gain when its ouput voltage depends *linearly* on the input voltage  $v_{in}$ , and accordingly is said to have an integral gain (I), (resp. derivative (D) gain), when it depends linearly on  $\int v_{in}$  (resp.  $\frac{dv_{in}}{dt}$ ). We will not deal here with non-linear filters for which Fourier analysis cannot be applied.

Let us now describe the properties of these different filters.

## E.4 Analysis of the simplest controllers

We first briefly examine the behaviour of the P controller, the I controller and the D controller so as to have a better feeling about what is to be done with our loop filter.

$$\text{P controller: } v_{out}(t) = K v_{in}(t) \iff V_{out}(\omega) = K V_{in}(\omega) \quad (\text{E.3})$$

$$\text{I controller: } v_{out}(t) = \frac{1}{\tau_I} \int_0^t v_{in}(t') dt' \iff V_{out}(\omega) = \frac{1}{j\omega\tau_I} \cdot V_{in}(\omega) \quad (\text{E.4})$$

$$\text{D controller: } v_{out}(t) = \tau_D \frac{dv_{in}}{dt} \iff V_{out}(\omega) = j\omega\tau_D \cdot V_{in}(\omega) \quad (\text{E.5})$$

Not much mathematical insight is required to understand that the phase gain of the P (resp. I, D) controller is just a constant  $0^\circ$  (resp  $-90^\circ$ ,  $+90^\circ$ ). It is also obvious to see that  $|F_I(\omega)| \rightarrow \infty$  as  $\omega\tau_I \rightarrow 0$  and *vice versa*, that  $|F_D(\omega)| \rightarrow 0$  as  $\omega\tau_D \rightarrow \infty$  and *vice versa* and that, of course  $|F_P(\omega)|$  is just a constant.

The standard way to represent a transfer function  $G(\omega) = V_{out}/V_{in}$  is to plot  $20\log_{10}(|G(\omega)|)$  (in deciBels) and  $\text{Arg}(G(\omega))$  (in degrees) as a function of – usually logarithmically scaled –  $\omega$ : it is called the *Bode diagram*. The Fig. E.3 shows the amplitude gain for the three basic controllers with the slope of  $-20\text{dB}$  (resp.  $+20\text{dB}$ ) per decade – a decade is an interval  $[f; 10f]$  for any  $f \neq 0$  – of the I (resp. D) controller.

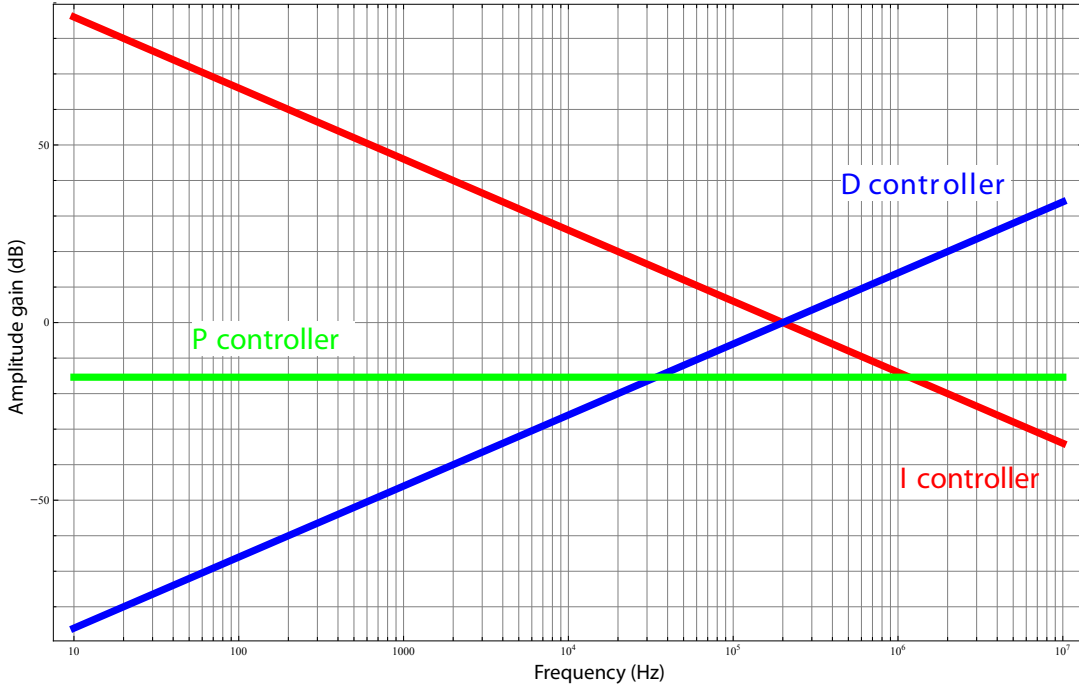


Figure E.3: This picture shows the amplitude gain of the three most basic controllers that one can imagine. For the I and D controllers, the gain is frequency dependent with a slope of  $\pm 20\text{dB}$  per decade.

What does this mean for the actual implementation of such a filter?

Firstly, one must keep in mind that we want to reach a high gain of the filter in order to have a high open loop gain  $|G_{ol}|$ .

The P controller has everywhere a constant, finite gain. If the gain is too low, the controller has merely no effect and the bigger the gain, the closer  $\Phi_s$  gets to  $\Phi_r$  for any frequency.

The I controller has infinite gain at 0 frequency *i.e.* for the DC component. As  $\omega$  increases, the integrator integrates a term which is oscillating – with a constant amplitude – always faster and so the output is just cancelling out and reaches gradually lower values. The strength of the I controller is that *it can build up a very large output* by adding up the error over time and so it is efficient for low frequencies. As time passes by, the DC component of the error comes into play and since its gain is infinite, the error is always getting closer to 0 but not fast. The integrator is said to *improve the steady state error*.

Also the I controller can be seen as taking the past of the input signal into account (and so it induces a negative phase shift *i.e* a phase lag).

The infinite gain for  $\omega = 0$  can also turn into a problem. Indeed, most signal generators output a oscillatory signal with a slight DC offset. If the loop is not appropriately tuned, the output that builds up because of the offset can drive the whole loop into a saturation limit (*e.g* saturation of op amps) which means the system is just stuck out of lock and must be reset.

The D controller has infinite gain at infinite frequency. When the input oscillates – with a constant amplitude – fast, it is changing in time very fast and the output of the D controller is larger : that controller is said to *improve the transient response of a loop* because it is able to respond much faster than the other two types. The D controller cannot directly throw the loop out of lock by having a diverging output like the I controller. The D controller can be seen as taking the future of the input signal into account (and so it induces a positive phase shift *i.e* a phase lead).

The disadvantage of the D controller and its diverging gain at high frequencies is its sensitivity to certain kinds of common noise with high frequency components. For instance, the electronic, thermal – also called Johnson-Nyquist – noise of any finite impedance has a frequency-independent (*i.e* white) power spectrum, which means that noise at low frequencies contributes as much as noise at higher frequencies at which D gain can have a very high gain, inducing instable operation of the phase-lock. In a controlled loop with a derivative gain, resonances easily make the system highly unstable.

Of course, any non-ideal controller is not able to operate equally well at any arbitrary frequency and has some inevitable low-passing features which amounts to having a built-in integrator (or double integrator, or triple, etc.). Now we know what the controllers can be used for as far as the amplitude gain is concerned. Of course every loop has its peculiarities and it must be carefully considered how they interact with the loop filter.

Let us now also briefly make some important comments about how the phase gain comes into play. The loop we are studying is based on *negative* feedback: if we detect a positive phase error  $\phi_r > \phi_s$ , the job of the loop is to act back on itself so as to compensate for that error by a positive shift of  $\phi_s$ .

We restrict ourselves to sinusoidal time-dependent signals since it is possible to describe any signal as a sum of sinusoids. As the signal goes through the loop, it accumulates time delays – for instance because it is propagating through cables with a finite velocity – which correspond to phase lags of the quantity  $G_{ol}$ ; if the signal is multiplied by  $-1$  over the path of the loop, which corresponds to a phase lag of  $\pm 180^\circ = \pm\pi$  rad, the error will have reached the value  $-\epsilon$  by the time the correction for an error  $+\epsilon$  is being applied and thus the error is pushed in the wrong direction because *negative feedback has been transformed into positive feedback*. We mentioned in Sec. E.1 that if the feedback becomes positive, the system behaves like an oscillator at unity gain instead of suppressing noise. The feedback is nevertheless not either positive or negative and can be inbetween; the closer to  $\pi$  radian

the phase gain gets, the “more positive” the feedback is. We recall here what we already wrote in Sec. E.1: if the amplitude gain is very high where the feedback is positive and the system is well described by eq. (E.1), then the system attenuates noise all the same. In order to now determine whether the system is stable or not, one must look further away in the Bode diagram for the value of the phase is at the point of unity gain  $|G_{ol}| = 1 = 0\text{dB}$ . The frequency where the phase lag of the loop is  $\pm\pi$  is called  $\omega_\pi$ .

As a result, it is very important to measure where the unity gain point  $|G_{ol}| = 0\text{dB}$  (assuming there is only one such point) and/or  $\omega_\pi$  are/is. Ideally, we would like to stay as close as possible to a  $0^\circ$  phase shift over the whole range of frequencies we are interested in controlling. This is a hard task though.

The issue of the stability of feedback systems is absolutely crucial and is a main topic of control theory. Knowing quantitatively whether and how much a system is stable requires a deeper analysis than will be given here. We simply wish here to give a feeling of the relevant ideas. The reader is invited to look up Ref.[37] for a thorough analysis.

Not taking into account the phase lag induced by the rest of the loop, we see that P, I or D controllers alone are stable because the phase lags associated with them are  $\pm 90^\circ$  and  $0^\circ$ . However, since I and D controllers do contribute to the phase gain and add up with other delays in the loop, they can contribute to the instability. A double integrator which is represented by the transfer function  $|F_{II}(\omega)| = \frac{-1}{\omega^2 \tau_I^2}$  has an amplitude gain that constantly decreases with a slope of  $-40\text{dB}$  per decade and a constant phase gain of  $-180^\circ$  (or  $+180^\circ$ ) and is therefore unstable at unity gain. As any system reaches unity gain at some point because the electronics is not able to respond equally at any frequency, using a double integrator can be bad for the stability of the system.

# Appendix F

## Looking at the setup in more detail

### F.1 The whole loop step by step

The whole loop is shown in Fig. F.1.

The output of the MINI-CIRCUITS VCO is amplified up to about 1.5W and this RF signal at  $f_{AOM}$  is fed into the AOM. Two AOM frequencies have been used: 80MHz and 200MHz, in order to be able to reach a difference of about 130MHz by operating each AOM slightly detuned from the center frequencies. The light sent into the AOM has a wavelength of  $\lambda_L = \frac{c}{\nu_L} \approx 769$  nm. At that point in the PLL, the signal is carried by a light wave with a frequency  $f_{shift} = \nu_L + f_{AOM}$ . This signal is the phase of the wave.

The shifted light is coupled into a 5meter long monomode optical fiber, which adds phase noise on the phase signal. This phase noise  $\delta\phi$  is equivalent to a frequency noise  $\frac{1}{2\pi} \frac{d}{dt}(\delta\phi(t))$ , which we would like to suppress. On the incoupling side, the fiber core is angle-cut: a small part of the light reflected off the air-core interface is directed out of the main beam path. On the outcoupling side, however, the fiber core is cut straight and the wavevector of the wave-guided light is retroreflected on the core-air interface: a few percent of the light is reflected backwards and goes through the fiber again, picking up once again the phase noise  $\delta\phi$ . Following the same path, that light propagates again through the AOM; its frequency is shifted again to

$$f_{shift^2,back} = f_{shift} + f_{AOM} + 2 \frac{1}{2\pi} \frac{d}{dt}(\delta\phi(t)) = \nu_L + 2 \times \left( f_{AOM} + \frac{1}{2\pi} \frac{d}{dt}(\delta\phi(t)) \right).$$

On the beam path, a few percent of that light backpropagating with frequency  $f_{shift^2,back}$  is picked off and shone onto a photodiode; light forward-propagating is also picked off on the same glass plate before it goes through the AOM and goes to the same photodiode where it interferes with the backpropagating light. Since the propagation inside the fiber is that of a plane wave, the reflection off the fiber-air interface with normal incidence results in a backpropagating beam with the same size and orientation at a given position as the beam propagating forward. Only the wavevector is opposite. The backpropagating beam and the beam that propagates forwards are said to be *mode-matched* and interfere efficiently.

On the photodiode, the two beams interfering and beating against each other, are:

- one weak, backreflected beam carrying the phase noise of the fiber, described by the electric field  $E_{BR}(t) = E_{BR}^{(0)} \cdot \cos([\omega_L + 2\omega_{AOM}]t + 2\delta\phi(t))$
- one much stronger main beam (or carrier), described by the electric field  $E_M(t) = E_M^{(0)} \cdot \cos(\omega_L t)$

For a beam of about 100mW input in the AOM, the main beam is in the 1-10mW range and the back-propagating beam is in the 10-100 $\mu$ W range. The fast photodiode detects the intensity  $I_{BN}$  of the interference given by the square of the electric field:  $I_{BN} \propto [E_{BR}(t) + E_M(t)]^2$ . All terms oscillating at  $2\omega_L$  are too fast for the photodiode and average out to 0. After expanding and turning the product of cosines into a sum, we have  $I_{BN} \propto E_{BR}^{(0)} \cdot E_M^{(0)} \cdot \cos(2\omega_{AOM}t + 2\delta\phi(t))$ , and we see that the photodiode outputs the *beat note* of  $E_{BR}$  against  $E_M$ .

After one stage of low noise amplification and another stage of “normal” amplification, about 10% of the beat note is picked off from the main line by a directional coupler and measured with a spectrum analyzer and the rest is input into the phase detector.

The phase detector is a simple *balanced mixer*. Mixers use the non-linearity of diodes to output the product of two input signals (named port L and R on most mixers). Sending in  $V_{ref,0}\cos(2(\omega_{AOM} + \zeta)t)$  and  $V_{s,0}\cos(2\omega_{AOM}t + 2\delta\phi(t))$  where  $\zeta$  is the frequency mismatch between the 2 inputs and assuming  $|\zeta| \ll \omega_{AOM}$ , the ouput port (named port I on most mixers) gives us something proportional to

$$V_{s,0}V_{ref,0}\cos(2(\omega_{AOM} + \zeta)t)\cos(2\omega_{AOM}t + 2\delta\phi(t)) = \frac{V_{s,0}V_{ref,0}}{2} \cdot [\cos(4\omega_{AOM}t + 2\zeta t + 2\delta\phi(t)) + \cos(2\zeta t - 2\delta\phi(t))]. \quad (\text{F.1})$$

If  $\delta\phi$  is a noise term with low frequency components compared to  $4\omega_{AOM}$  it is then easy to get rid of the latter by low-passing the output of the mixer.  $4\omega_{AOM}$  in our case is  $2\pi \times 800\text{MHz}$  or  $2\pi \times 320\text{MHz}$ . As we were interested in reaching a lock-box bandwidth of a few hundred kHz using operational amplifiers in the 1 to 10Mhz gain-bandwidth product range, we just assumed that the lock-box is not responding to this very fast signal because it is averaged out. In this case, the active components of the lock-box automatically form a low-pass filter by themselves, and we do not need to build in an actual one. That signal at  $4\omega_{AOM}$  has the same amplitude as  $\cos(2\delta\phi(t))$  and can become a problem when faster op amps are used. Taking these considerations into account, we can assume that the mixer outputs  $\cos(2\zeta t - 2\delta\phi(t))$ . The error signal is a sinusoid with phase noise when  $\zeta \neq 0$ ; otherwise it is proportional to  $\cos(2\delta\phi(t))$ . In this case, the error signal around 0 is just proportional to  $\delta\phi(t)$  in the limit of small  $\delta\phi$  (because  $\sin(x) \sim x$  when  $x \rightarrow 0$ ).

Our loop filter is a controller that can be switched between P gain and PI gain. It is part of a lock-box containing an instrumentation amplifier AD8421 which can apply a primary overall gain. The loop filter is followed by an offset stage. The sum of the offset and the error signal processed by the loop filter goes to the MINI-CIRCUITS VCO which is mounted on the lock-box board and so the loop is closed.

## F.2 Schematic of the whole loop

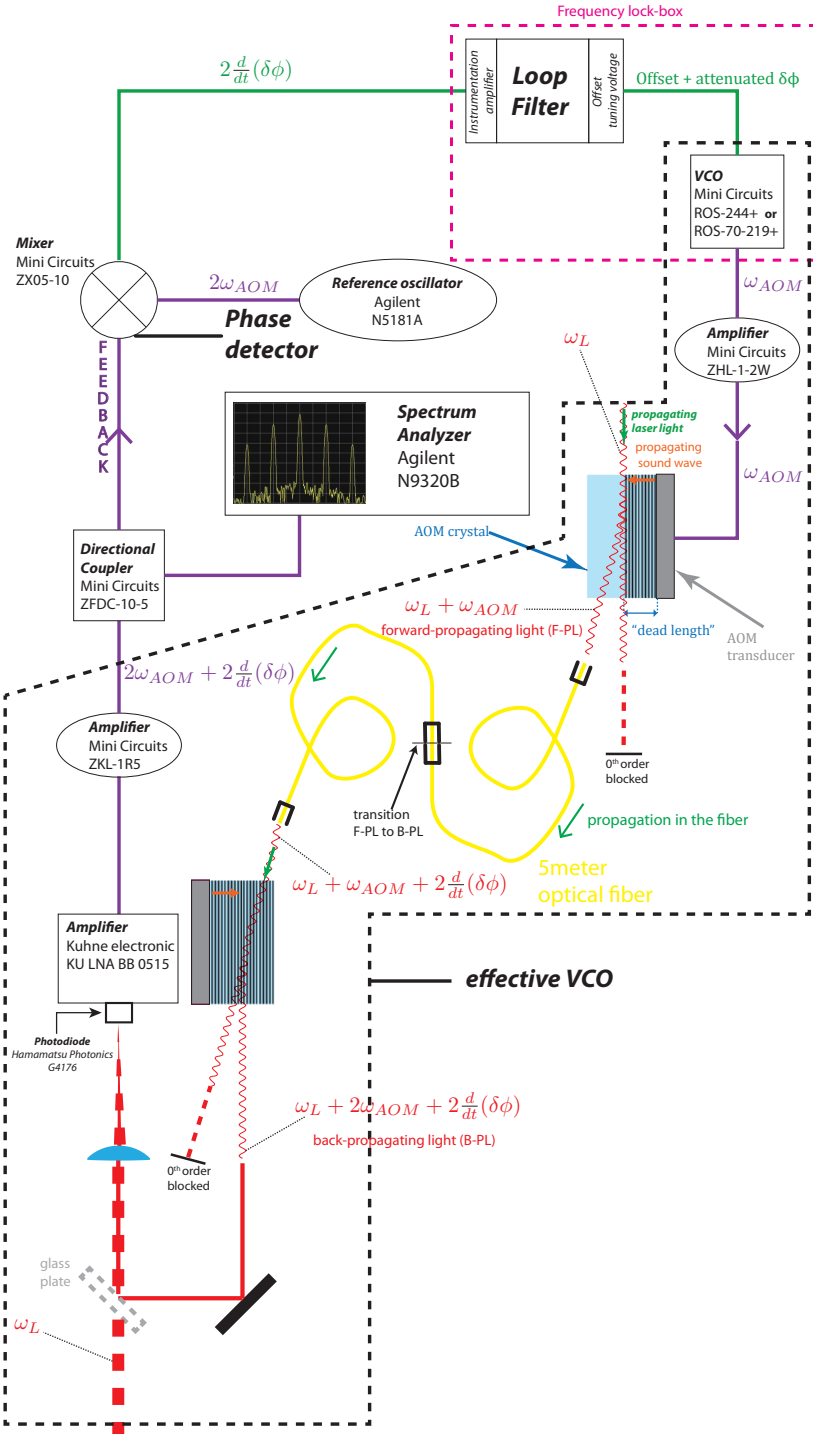


Figure F.1: This picture shows every components of the loop. The path contains twice the same fiber because the beam is reflected off one tip of the fiber and backpropagating through it again.

# Bibliography

- [1] Richard Feynman. Simulating quantum mechanics with computers. *Int. J. Theor. Phys.*, **21**:467, 1982.
- [2] I. Bloch, J. Dalibard, and S. Nascimbène. Quantum simulations with ultracold quantum gases. *Nature Physics*, **8**:267, 2012.
- [3] Rainer Blatt and Roos Christian. Quantum simulations with trapped ions. *Nature Physics*, **8**:277, 2012.
- [4] Alán Aspuru-Guzik and Philip Walther. Photonic quantum simulator. *Nature Physics*, **8**:285, 2012.
- [5] Neil Ashcroft and David Mermin. *Solid State Physics*. Harcourt, Orlando (FL, USA), 1976.
- [6] M. A. Paalanen, D. C. Tsui, and A. C. Gossard. Quantum hall effect at low temperatures. *Phys. Rev. B*, **25**:5566, 1982.
- [7] D. R. Yennie. Integral quantum hall effect for nonspecialists. *Rev- Mod. Phys.*, **59**:781, 1987.
- [8] K. W. Madison, F. Chevy, W. Wohlleben, and J. Dalibard. Vortex formation in a stirred bose-einstein condensate. *Phys. Rev. Lett.*, **84**:806, 2000.
- [9] J. R. Abo-Schaeer, C. Raman, J.M. Vogels, and W. Ketterle. Observation of vortex lattices in bose-einstein condensates. *Science*, **292**:476, 2001.
- [10] A.E. Leanhardt, A. Görlitz, A. P. Chikkatur, D. Kielpinski, Y. Shin, D. E. Pritchard, and W. Ketterle. Imprinting vortices in a bose-einstein condensate using topological phase. *Phys. Rev. Lett.*, **89**:190403, 2002.
- [11] Y.-J. Lin, R. L. Compton, K. Jiménez-García, J. V. Porto, and I. B. Spielman. Synthetic magnetic fields for ultracold neutral atoms. *Nature*, **462**:628, 2009.
- [12] M. Aidelsburger, M. Atala, S. Nascimbène, Chen Y.-A. Trotzky, and I. Bloch. Experimental realization of strong effective magnetic fields in an optical lattice. *Phys. Rev. Lett.*, **107**:255301, 2011.

- [13] Yakir Aharonov and David Bohm. Significance of electromagnetic potentials in quantum theory. *Phys. Rev.*, **115**:485, 1959.
- [14] John D. Jackson. *Classical Electrodynamics (third edition)*. John Wiley & Sons, Hoboken (NJ, USA), 1999.
- [15] Michael V. Berry. Quantal phase factors accompanying adiabatic changes. *Proc. R. London*, **A392**:45, 1984.
- [16] Nigel Cooper. Optical flux lattices for ultracold atomic gases. *Phys. Rev. Lett.*, **106**:175301, 2011.
- [17] Nigel Cooper and Jean Dalibard. Optical flux lattices for two-photon dressed states. *EPL.*, **95**:66004, 2011.
- [18] M. Greiner, O. Mandel, T. Esslinger, T. W. Hänsch, and I. Bloch. Quantum phase transitions from a superfluid to a mott insulator in a gas of ultracold atoms. *Nature*, **415**:39, 2002.
- [19] C. Becker, P. Soltan-Panahi1, J. Kronjäger, S. , Drscher, K. Bongs, and K. Sengstock. Ultracold quantum gases in triangular optical lattices. *New Journal of Physics*, **12**:065025, 2010.
- [20] A. M. Dudarev, R. B. Diener, I. Carusotto, and Q. Niu. Spin-orbit coupling and berry phase with ultracold atom in 2d optical lattices. *Phys. Rev. Lett.*, **92**:153005, 2004.
- [21] Nigel Cooper. Rapidly rotating atomic gases. *Adv. Phys.*, **57**:539, 2008.
- [22] J. Dalibard, F. Gerbier, G. Juzeliūnas, and P. Öhberg. Artificial gauge potentials for neutral atoms. *Rev. Mod. Phys.*, **83**:1523, 2011.
- [23] Joseph E. Avron, Daniel Osadchy, and Ruedi Seiler. A topological look at the quantum hall effect. *Physics Today*, **56**:38, 2003.
- [24] D. K. Nandy, Y. Singh, B.P. Shah, and B. K. Sahoo. Transition properties of a potassium atom. *Phys. Rev A*, **86**:052517, 2012.
- [25] Martin Reitter. Ultracold fermions in a novel 2d setup. Master Thesis, LMU University of Munich, 2012.
- [26] Bahaa E. A. Saleh and Malvin C. Teich. *Fundamentals of Photonics (second edition)*. John Wiley & Sons, Hoboken (NJ, USA), 2007.
- [27] Tobias Tiecke. Properties of potassium. available at <http://staff.science.uva.nl/~tgtiecke/PotassiumProperties.pdf>, 2010.
- [28] Harold J. Metcalf and Peter van der Straten. *Laser Cooling and Trapping*. Springer-Verlag, New York (NY, USA), 1999.

- [29] John Evans. Šolc birefringent filters. *J. Opt. Soc. Am.*, **48**:142, 1958.
- [30] John Evans. The birefringent filter. *J. Opt. Soc. Am.*, **39**:229, 1949.
- [31] Christoph Becker. Multicomponent bose-einstein condensates. PhD Thesis, University of Hamburg, 2008.
- [32] Martin W. Zwierlein and Wolfgang Ketterle. Making, probing, and understanding ultracold fermi gases. In *Ultracold Fermi Gases*, volume **164** of *Proceedings of the international school of physics "Enrico Fermi"*, page 95, 2007.
- [33] Ignacio Cirac and Peter Zoller. Goals and opportunities in quantum simulation. *Nature Physics*, **8**:264, 2012.
- [34] S. Das Sarma, M. Freedman, and C. Nayak. Topological quantum computation. *Physics Today*, **59**:32, 2006.
- [35] Christopher C. Davis. *Lasers & Electro-Optics: Fundamentals & Engineering*. Cambridge University Press, Cambridge (England), 1996.
- [36] Roland E. Best. *Phase-Locked Loops: Design, Simulation & Application (sixth edition)*. McGraw-Hill, New York (NY, USA), 2007.
- [37] Norman S. Nise. *Control Systems Engineering (sixth edition)*. John Wiley & Sons, Hoboken (NJ, USA), 2011.